SCALABLE DESIGNS AND METHODS FOR HETEROGENEOUS ELECTRONIC-PHOTONIC INTEGRATED CIRCUITRY

BY

JOHN A. CARLSON

THESIS

Submitted in partial fulfillment of the requirements
for the degree of Master of Science in Electrical and Computer Engineering
in the Graduate College of the
University of Illinois at Urbana-Champaign, 2017

Urbana, Illinois

Adviser:

Associate Professor John M. Dallesasse

ABSTRACT

A set of semiconductor designs shown to be capable of facilitating scalable and reconfigurable layouts for electronic-photonic integrated circuitry is presented. Three emphases are established to outline and discuss the methods and advantages of merging stand-alone optical components into integrated heterogeneous systems, specifically for implementing optical sensing, efficient laser wavelength tuning, and III-V-on-Si semiconductor fabrication techniques together on a single platform. Considerations regarding the optical geometries and power efficiency of each design are reiterated to assure that each design is compatible with the goals of system-level integration in either biochemical point-of-use or telecommunications applications.

These three approaches to scalable photonic designs are then investigated in their ability to offer dynamic controls of optical signals and their novel usage of heterogeneous material patterning. The optical sensing platform directly integrates multiple linear variable filters (LVFs) atop a CMOS image sensor for electronic controls of detecting a biochemical fluorescent or absorptive optical signal signature, enabling good wavelength resolution ($3.77 - 6.08$ nm) over a wide-band detection spectrum. Detection limits of 0.28 nM for Quantum Dot emitters and 32 ng/mL for near-infrared fluorescent dyes are found in this integrated design, providing comparable results in the compact optical platform to conventional laboratory spectrometers. The instrument is then extended in its usage by testing on point-of-use detection tests via discerning the concentration of free-chlorine in water colorimetrically. The tunable laser cavity design integrates together a GaN waveguide into a standard InGaAsP telecom (1550 nm) edge-emitting laser atop silicon, allowing for wide-band tuning via the strong anisotropic effects solved for in wurtzite GaN. A tuning parameter based off a refractive index variation, Δn, is found to be at $|1.75 \cdot 10^{-4}|$, based off the electro-optic effects in conjunction with an etched grating geometry designed directly into the coupled GaN waveguide, with the structure further extended into a Y-branch laser cavity to enable the Vernier effect for wideband tuning via mode-hopping. A separate GaN-based design, consisting of an RF signal modulator that launches a surface acoustic wave (SAW) into a cavity to produce a highly controllable refractive index variation, Δn, via the photo-elastic and photo-elastic effects, is found to produce a large tuning parameter of $|1.84 \cdot 10^{-3}|$. These effects are then described in their application to dynamically controllable effects for dense wavelength division multiplexing (DWDM) and how the underlying electronic platform enables this, providing advantages over larger footprint or less efficient designs. The fabrication techniques designed provide a method to enable bonding of III-V epitaxial wafers onto a silicon carrier wafer for large-scale processing before final bonding onto CMOS. A processing recipe takes bulk GaAs epitaxial structures and constructs a method for reversibly bonding and processing them on a silicon carrier wafer as III-V islands, ready for final large scale flip-chip bonding onto aligning CMOS features. Additional findings discuss the merits of various etch processes and techniques such that they are compatible to the heterogeneous III-V-on-Si patterning as laid out. The methods optimized allow for simultaneous, heterogeneous development of system-level device integration such that further processing can place various III-V devices side-by-side and process geometries in unison. Processing steps and their results are presented. The extension of this method to different III-V alloys beyond GaAs entirely is therefore considered for even larger-scale system design across photonic elements.

Each set of findings presents both the relevant photonic device characteristics and also a method on how to intersect these devices with a paired CMOS electronic system on silicon, so that a single unified electronic-photonic schematic can be made. Accompanying these conclusions is a range of experimental work ranging from simulation studies, to full-scale integrable sensing designs and their testing, to detailed cleanroom-based fabrication processes for designing the system of III-V-on-Si patterns. A final set of conclusions relates the three tracks of research as being part of a common path forward in scalable photonics designs. Forecasts are then made on how the field of electronic-photonic integration and its applications utilized herein may yet evolve and potentially encompass findings or methodologies from this work.

To the greater minds who have come before me and left work unfinished.

ACKNOWLEDGMENTS

I would first like to acknowledge all of my friends and family who helped me through this long journey toward a master's degree in electrical engineering and this accompanying thesis. Without their emotional and academic support, many of the stresses of graduate school would have slowed me down considerably in realizing a body of work that I can now be proud of. The fact that they were there by phone, email, or text to proofread my drafts, listen to my frustrations, and propose brilliant outsider-perspectives speaks volumes to me. In particular, I would like to thank my parents John Sr. and Mary Beth; my three sisters Teri, Kelly, and Abby; and my close friends Cliff Fosmore and Rianna Weisse for each giving me support and feedback.

This work and in particular this thesis stemmed from numerous brainstorming sessions and active discussions with close coworkers, and so I would also like to acknowledge all of the people who have helped me in understanding and appreciating the background work of semiconductor lasers to which I hope to add. In particular, I would like to thank Professor Yuhang Wan who, as a postdoctoral student, guided me through my first project as a graduate student and taught me how to achieve good results and manage my daily expectations; and to Tommy O'Brien who, as my groupmate and desk-mate, taught me a great deal about cleanroom processing.

Finally, I would like to thank my advisor Professor John Dallesasse. None of this work would have been possible without his consistent feedback and insight, from the theoretical to the experimental, and I feel a great deal of gratitude for his understanding and encouragement throughout this work. He has taught me to appreciate the link between professor and student as an active open discussion. I look forward to continuing my PhD under his guidance.

TABLE OF CONTENTS

CHAPTER 1: INTRODUCTION

"The invention of the integrated circuit was the most important moment since man emerged as a life form."
- Isaac Asimov, 1983

1.1 MOTIVATION

It all began from a modest frustration with the vacuum tube. Two scientists, one spark, and the lessons from all who came before them. What resulted transformed forever what it meant to control the flow of electricity [1]. From this transfer-resistor, or transistor, a series of advances built off early solid-state research showed how the ability to control the flow of electrical carriers could also enable their excitation and optical recombination, resulting in the semiconductor laser [2,3]. Crucial to this insight was the revelation in how materials could be heterogeneously alloyed to produce a continuum of optical wavelength output possibilities, thereby forever expanding what it meant to emit energy photonically [4]. These events marked the dawn of an era of networking devices that could harness the photonic or electronic energy domains.

The inventions and innovations from semiconductor research have caused nothing short of a technological revolution that still yields unparalleled benefits to this day [5,6,7], expanding the ability to control the forces of nature and opening up vast industries in computation and telecommunications. The fields of electronic and photonic devices—controlling the propagation of electricity and light, respectively—owe their livelihoods to the unique properties of the semiconductor. These have enabled the formation of highly controllable and reconfigurable devices that produce stark new phenomena. From this, a scalable process has been born. A single laser diode can now do the heavy lifting of spools of copper wire and transmit along an optical fiber the data-stream from an electronic processing network as fast as 40 Gb/sec [8]. The methods derived through this research have enabled a widespread understanding of photonic devices and electronic devices separately, each with their own advantages for their respective tasks, yet great potential remains in the ability to bridge the two into one common integrated network. To reach this apex, a deep understanding as to what has come before it is crucial.

The ability to employ semiconductors in various geometries and conductivities has enabled highly compact, scalable integrated circuitry designs in the field of electronics. Repeatable techniques and considerations regarding the routing and distribution of signals enabled the first silicon-based electronic integrated circuitry [9], and later work perfected various fabrication strategies to push forward large-scale agile electronic networks [10]. Buoyed by the earlier theoretical work on semiconductor crystals [11,12], rapid advances in understanding the effects caused by doping [13], carrier mobility [14], and native oxide growth/patterning [15, 16] culminated in the complementary metal-oxide-semiconductor field-effect transistor (CMOS), now regarded as the ideal low static power switchable gate for electronic logic and processing [17]. From here, considerable work has continued in establishing methods for electronic integrated circuitry that center on standardized homogeneous silicon growths capable of dense interconnects and increasingly rapid effects [18]. This common platform centered on the CMOS gate and its suite of fabrication techniques that enabled and continues to enable a reproducible and reliable process for electronic integrated circuitry.

Going from the realm of laboratory work to highly regimented device architectures required the seamless interaction of a fundamental set of devices that can be made dynamic and easily controllable.

It is now the intent of the field of photonics to do the same. Large gains in processing speed and energy savings in transmission (Joules/bit) can be made possible by hosting numerous operations between routed optical signals that currently are being transduced into electronic signals [19]. Various other capabilities could also be possible with integrated photonic systems, ranging from the ability to interrogate chemical and biological systems [20], to excite and respond to external environmental stimuli [21], to link devices into gated photonic logic processors [22], and to further intertwine classical and quantum optics [23, 24]. But as straightforward as this desire is, the process that follows is anywhere but certain, given complexities inherent in semiconductor laser designs. Following the first semiconductor laser designs, various research pursuits have made inroads into resolving those complexities with optimal laser device designs that point us forward. These included fabricating double heterostructures [25,26], quantum well carrier-confined lasers [27], thin-film growths using metal-organic chemical vapor deposition (MOCVD) [28,29], native oxidation processes [30], oxide-confined vertical cavity designs [31], distributed feedback structures [32], and three-terminal devices [33]. Along with these, advances in semiconductor crystal theory and growth have enabled photonic materials capable of emitting or detecting photon energy spanning from UV (<400 nm) to mid-infrared (>3 μm) [34,35,36,37]. In each of these breakthroughs, a compound made from compatible cathodic and anodic semiconductors served as the photonic material, with particular success using group III-V elements. These III-V photonic devices thus represent a departure from the self-contained growth methods in silicon CMOS fabrication, given the very intent in allowing for a range of III-V alloys for different photonic operations [38]. Compatibility and scalability is where integration hinges. As such, accommodating various photonic capabilities within a common platform reveals surmountable difficulties. The ability to seamlessly connect and distribute photonic devices for the propagation of optical signals remains the goal inherent in photonic integration.

1.2 METHODS

Together then, the goals of integrating photonics and the established methods for electronic integration point to a path forward. The current optoelectronic infrastructure has been designed with a diverse set of parameters—ranging from choice in gain material, cavity design, and modulation technique—each tailored to a single device, yet a full-scale integrated platform is considered key for denser signal propagation [39]. To do this, a simple framework and set of principles is key. The continual expansion of telecommunication systems prompts this desire for more photonic-based processes, where a system of electrically modulated laser structures can reliably route and interpret signals in-plane on chip [40].

Current state-of-the-art plans in integrated photonics look to monolithic designs for scalable processes. Typically, InP-based systems have been produced for long-haul telecommunication networks [41] whereas in other work Si-based layouts seeks to enable inexpensive rack-to-rack systems [42]. Yet with both of these, the constraints of monolithic designs both add design complexity and hamper the full realization of reconfigurable photonic systems. Given the main advantage in integrated photonics is its versatility in signal manipulation over electronics, monolithic

networks introduce steep tradeoffs and losses as each photonic component must be recast and reoriented into the single material die, inherently limiting the benefits of scale and dynamic controls [43]. The answer to this is therefore to look at heterogeneous integration, establishing methods for a common platform across III-V's that is capable of handling photonics and serving the full range of system-level needs.

Yet in serving those needs, the essential carrier conditions required for gain and stimulated emission serve as a rigid set of constraints for photonic signal generation. To drive a photonic system, an electronic system must be paired that can provide the necessary current, voltage, or high-speed modulating signal input [44]. This is especially true for large-scale photonic systems. As such, it is not enough to look at integrated photonics isolated from its sister domain of electronics. To do so would be to assume coupling of external generated light into a passive integrated photonic structure, a feat since accomplished and left wanting, given its losses and limits in scalability [45, 46]. Instead, it is the motivation and the goal of this thesis to design and plan specific methods for a fully-contained network: heterogeneous electronic-photonic integrated circuitry. This network would have the advantage of coordinated control in both electronic and photonic domains, able to route signals in either and to leverage both capabilities. The work described herein establishes designs and processes for integrated photonic devices such that they can be interconnected with CMOS electronics for an overall scalable, reconfigurable system. A methodology of research has been constructed that marks individual steps toward the desired platform of fundamental photonic devices.

1.3 THESIS ORGANIZATION

This thesis delves into the above discussion and proposes a set of methods and designs to create III-V photonic device designs compatible with mature CMOS fabrication. The nature of photonics requires that a range of parameters be considered in designing any system, so as such the work presented here will focus on testing the hypothesis that a single heterogeneously integrated system for photonic devices is scalable. Three important aspects in integrated photonic devices will be investigated and results for each discussed, covering integrated optical sensing, integrated laser cavity tuning, and scalable III-V-on-Si fabrication methods. Given the multidisciplinary nature of photonics, the scope of this work will be presented in both its theoretical and experimental forms.

Beginning in Chapter 2, a thorough background on the physics and material science necessary for this work is discussed, concluding with how this theory is implemented. Emphasis will be placed on implications from both classical and quantum mechanical effects that together overlap to make laser physics. Following this, the design and testing of an integrated spectrometer capable of small-signal sensing is detailed in Chapter 3. Experimental results are shown for how the process of converting this benchtop optical design into an integrated CMOS-compatible system is accomplished, showing direct applications in wide-band biological and chemical sensing. Chapter 4 then presents the progress in designing integrated laser structures capable of cavity tuning designs. By studying the anisotropies present in the semiconductor gallium nitride (GaN) and its alloys, a set of laser structures is proposed in which small refractive index changes induced by an applied bias can enable dense wavelength division multiplexing (DWDM) in a single low-power device. Discussed in Chapter 5, methods and processes are optimized for large-scale fabrication of

heterogeneously integrated photonic devices. In here, a step-by-step fabrication plan for integrating III-V-on-Si is explored that prepares active and passive photonic devices for interconnection atop silicon. This process is explained for means of enabling scalability and coordination between various electronic and photonic devices on a single chip. Finally, the scope of these findings is then considered in Chapter 6, where an active discussion is given that forecasts how these initial steps toward heterogeneous electronic-photonic integrated circuits pave the way toward rapidly expanding system capabilities. A series of next steps is proposed for realizing the full potential of integrated electronic-photonic systems in light of the results found in sensing, cavity tuning, and integrable fabrication.

The goal of this thesis is to establish the merits in finding a common platform for heterogeneous electronic-photonic integration and then present a cohesive methodology to achieve this, with individual findings and relevant analyses.

CHAPTER 2: BACKGROUND

"I am here to support the assertion that light of every kind is itself an electrical phenomenon – the light of the sun, the light of a candle, the light of a glow-worm."
- Heinrich Hertz, 1889

2.1 PERSPECTIVE

The understanding of light and its interaction with matter remains one of the most fundamental and cherished breakthroughs in physics. It is at the core of how we approach all photonic devices. A set of explanations for optical phenomena have emerged that project the same observations onto different rulesets tailored to a particular scale and scope. This has been the root of optical science since the quarrels of Newton and Hooke, and modern semiconductor laser physics is no exception. As such, a full understanding of the physics behind the laser and its application to integrated photonics must be able to connect these rulesets.

The following presents the necessary physical background for what goes into the light-matter interaction in optoelectronics by splitting up the relevant theory into parts. An overview of classical electromagnetics is first presented that hones in on the conditions to produce wave propagation and modal guidance inside laser structures. Added to this is then a quantum mechanical picture of photon generation and the ruleset for stimulated emission. Then an overview of the material science behind III-V semiconductor material parameters is presented. Finally, a full understanding of laser physics is constructed out of these varied constraints and guidelines for integrating electronics with these photonic devices are laid out.

2.2 CLASSICAL ELECTROMAGNETICS

2.2.1 Wave Dynamics

The central tenet of electromagnetics is that propagating light must emerge from any geometric form upon the temporal and spatial variation of electric (E) and magnetic (H) fields inside of it. It is known that this can be expressed as the general free-space integral form of Maxwell's equations:

$$\oint_C E(r,t) \cdot dl = -\mu_0 \frac{d}{dt} \iint_S H(r,t) \cdot dS \tag{2.1}$$

$$\oint_C H(r,t) \cdot dl = \varepsilon_0 \frac{d}{dt} \iint_S E(r,t) \cdot dS + \iint_S J(r,t) \cdot dS \tag{2.2}$$

where ε_0 and μ_0 stand for the electric permittivity and magnetic permeability of free-space, respectively, and $J(r,t)$ is the applied electric source term as a carrier current density [47]. If one then assumes a generalized homogeneous medium for propagation of light, this postulate can be simplified down to its differential, frequency-domain form:

$$\nabla \times E = -j\omega\mu H \tag{2.3}$$

$$\nabla \times H = j\omega\varepsilon E + J \tag{2.4}$$

Here, $\varepsilon = \varepsilon_0\varepsilon_r$, where ε_r is the relative permittivity for a material, and similarly $\mu = \mu_0\mu_r$ with μ_r as the relative permeability. Combining these two together, assuming no current sources in propagation, and by employing the Coulomb gauge condition such that $\nabla \cdot E = 0$ [47], the general Helmholtz wave equation is produced:

$$\nabla^2 E + \omega^2\mu\varepsilon E = 0 \tag{2.5}$$

By this, the first essential tool for photonic design is made apparent. Noting that this differential equation produces spatial-sinusoidal terms for positive values of $\omega^2\mu\varepsilon$ while negative values produce spatial-exponential decay terms, this effect is encapsulated in one term known as the complex *refractive index*, $\tilde{n}$:

$$\tilde{n} = \sqrt{\mu_r\varepsilon_r} = n + i\kappa \tag{2.6}$$

For the purposes of propagation and later laser cavity design, the real part of the refractive index, n, acts as the figure of merit [48]. It is noted that the refractive index is initially assumed to be isotropic, or degenerate in all axial directions, yet conditions of anisotropic media are later explored for their nonlinear effects. This shows that an oscillating electric field induces an oscillating magnetic field, and vice versa; together, this observation becomes *wave propagation*, where the translation of energy between electric and magnetic terms propels the overall optical power along a Poynting vector, $\vec{S}$, as the curl of the two terms:

$$\vec{S} = E \times H \tag{2.7}$$

This wave equation and the derivation of real refractive index is familiar and thus bedrock to all who study photonics, but in it already is a key factor: that a time-harmonic field can produce a propagating electromagnetic wave whose behavior is closely related to its effective material refractive index. This becomes crucial in later findings on laser design.

As an electromagnetic wave continues through a material sinusoidally, it maintains a spatial phase relationship that is dependent on its refractive index and propagation constant, k, such that

$$k^2 = \omega^2\mu\varepsilon = \frac{\omega^2}{c^2}n^2 \tag{2.8}$$

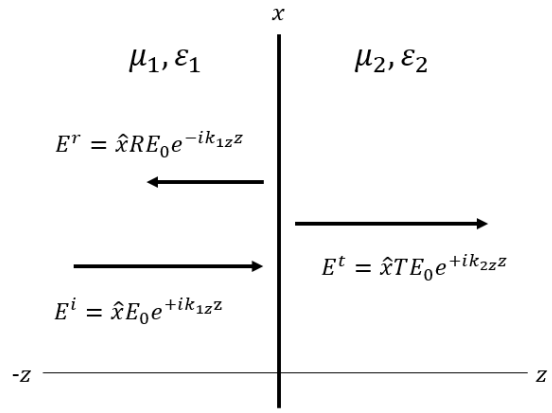

Figure 2.1 Effect of reflection and transmission for incident plane waves

where $c = 1/\sqrt{\mu_0\varepsilon_0}$. This propagation constant, or phase constant, is in effect the descriptor for how a constant phase-front evolves as it traverses a medium, where a larger refractive index implies an optically denser material, meaning a phase velocity delays as goes $1/n$ [48]. Utilizing the Helmholtz wave equation, this allows us to assume an ansatz of an incident electric field emanating from a source as a plane wave:

$$E^i = \nabla \times \hat{r}E_0e^{ik_r \cdot r} \tag{2.9}$$

In this, a time harmonic is assumed in the wave, meaning a frequency-domain propagation wave evolves both spatially and temporally in phase and carries its power along the Poynting vector, $\hat{r}$. The electric field—and by extension the magnetic field too—propagates unabated for the duration that the material index seen is constant [47,48].

2.2.2 Reflection and Transmission

When an electromagnetic field then does happen upon a material change, the refractive index changes and a shift in wave dynamics is observed. By this, the second major constraint of laser physics and thus integrated photonics is observed: *reflection* and *transmission* occurs at index interfaces. At each index interface, a fraction R of the incident field is reflected, while a complementary fraction T is transmitted, as shown in Figure 2.1. Here, k_{1z} and k_{2z} denote the propagation constants for each material, where a refractive index change from n_1 to n_2 occurs and thus components of the field must match at the interface for propagation to exist. Given the constraint of electromagnetics that all tangential components of an electrical field must be continuous at interfaces [47], it then follows that:

$$\hat{z} \times \vec{E}(z = 0^-) = \hat{z} \times \vec{E}(z = 0^+) \tag{2.10}$$

$$1 + R = T \tag{2.11}$$

It is further important to add that the magnetic field components exhibit similar continuity conditions at all index interfaces, so given the orthogonality of the magnetic field, it is also true that:

$$\hat{z} \times \vec{H}(z = 0^-) = \hat{z} \times \vec{H}(z = 0^+) \tag{2.12}$$

$$\frac{1}{\eta_1} \cdot (1 - R) = \frac{1}{\eta_2} \cdot T \tag{2.13}$$

where the wave impedance $\eta_i = \sqrt{\mu_i/\varepsilon_i}$ comes from solving through with the differential form of Maxwell's equations. Combining terms, a general definition for the reflection coefficient of any index-step interface at normal incidence is found as:

$$R = \frac{\eta_2 - \eta_1}{\eta_2 + \eta_1} \tag{2.14}$$

Thus, a reflection of a propagation wave can be induced by the intentional introduction of an index contrast. This principle enables the use of selectively reflective facets in various optoelectronic designs [48,49], such that the dynamics of a wave packet can be made spectrally-sensitive.

To then extend this principle to cases beyond normal incidence, a propagating field obliquely incident can also be divided into its parts. Depending on the angle of incidence, θ_i, a corresponding reflection and transmission result. A refractive bend in the transmitted wave occurs, due to the propagation constant transition and its dependence on the index contrast [47]. Shown in Figure 2.2a and 2.2b, this phenomenon is shown for the two cases of oblique incidence, dependent on whether the electric field component points parallel to the index interface ($z = 0$) or is in-plane perpendicular to the interface. For the first case, the electric field is entirely out-of-plane but its phase propagation is trigonometrically in-plane, as:

$$E^i = \hat{y} E_0 e^{+ik_1(x \sin\theta_i + z \cos\theta_i)} \tag{2.15.1}$$

$$E^r = \hat{y} R_{TE} E_0 e^{+ik_1(x \sin\theta_r - z \cos\theta_r)} \tag{2.15.2}$$

$$E^t = \hat{y} T_{TE} E_0 e^{+ik_2(x \sin\theta_t + z \cos\theta_t)} \tag{2.15.3}$$

A corresponding set of magnetic field terms can then be found, utilizing (2.3), including wave impedance, and noting the required orthogonality of field terms [47]:

$$H^i = (-\hat{x} \cos\theta_i + \hat{z} \sin\theta_i) \frac{1}{\eta_1} E_0 e^{+ik_1(x \sin\theta_i + z \cos\theta_i)} \tag{2.16.1}$$

$$H^r = (\hat{x} \cos\theta_r + \hat{z} \sin\theta_r) \frac{1}{\eta_1} R_{TE} E_0 e^{+ik_1(x \sin\theta_r - z \cos\theta_r)} \tag{2.16.2}$$

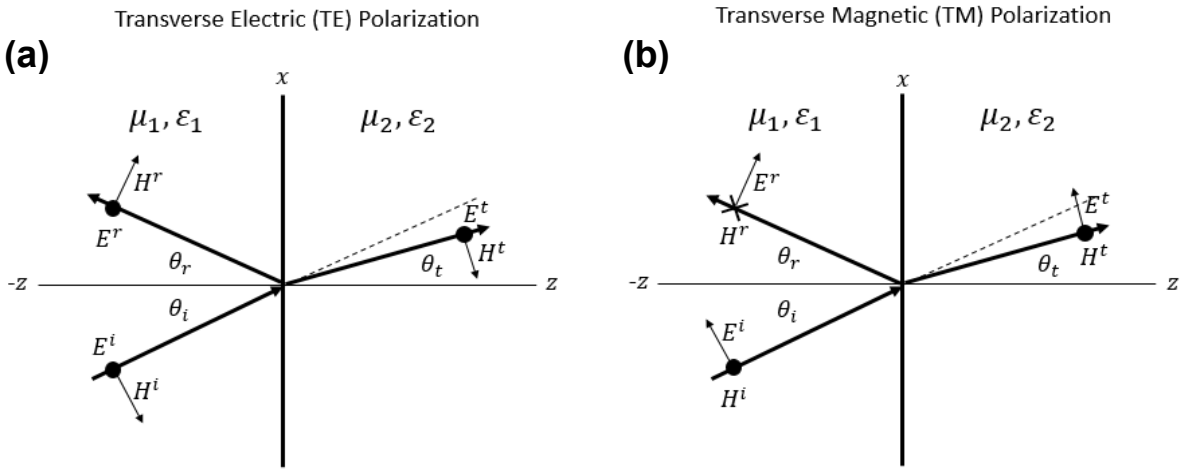

Figure 2.2 Effect of oblique incidence for (a) transverse electric (parallel) polarization and (b) transverse magnetic (perpendicular) polarization

$$H^t = (-\hat{x}\cos\theta_t + \hat{z}\sin\theta_t)\frac{1}{\eta_2}T_{TE}E_0 e^{+ik_2(x\sin\theta_t + z\cos\theta_t)} \tag{2.16.3}$$

Thus, a first set of terms for full wave dynamics at the index interface is found. If looking down along the x-axis as shown, only the electric field components look cross-sectionally transverse and is so termed parallel polarization, but for purposes later detailed this is more aptly seen as a *transverse electric (TE) polarized* field [48]. In the second case, the phase propagation remains consistent due to the unchanging Poynting vector, but the electric field terms spread across the direction perpendicular to the former:

$$E^i = (\hat{x}\cos\theta_i - \hat{z}\sin\theta_i)E_0 e^{+ik_1(x\sin\theta_i + z\cos\theta_i)} \tag{2.17.1}$$

$$E^r = (\hat{x}\cos\theta_r + \hat{z}\sin\theta_r)R_{TM}E_0 e^{+ik_1(x\sin\theta_r - z\cos\theta_r)} \tag{2.17.2}$$

$$E^t = (\hat{x}\cos\theta_t - \hat{z}\sin\theta_t)T_{TM}E_0 e^{+ik_2(x\sin\theta_t + z\cos\theta_t)} \tag{2.17.3}$$

Again the magnetic field terms can be derived by a curl operation on the electric terms:

$$H^i = \hat{y}\frac{1}{\eta_1}E_0 e^{+ik_1(x\sin\theta_i + z\cos\theta_i)} \tag{2.18.1}$$

$$H^r = -\hat{y}\frac{1}{\eta_1}R_{TM}E_0 e^{+ik_1(x\sin\theta_r - z\cos\theta_r)} \tag{2.18.2}$$

$$H^t = \hat{y}\frac{1}{\eta_2}T_{TM}E_0 e^{+ik_2(x\sin\theta_t + z\cos\theta_t)} \tag{2.18.3}$$

For this case, instead, when looking down the x-axis it is seen that solely the magnetic field terms are fully cross-sectionally transverse, whereas the electric field contains components in x and z. This case is therefore termed perpendicular polarization when in free-space propagation, but it is beneficial to see this as a *transverse magnetic (TM) polarized* field. These depictions of polarization represent further crucial understandings in constructing a full picture of photonic devices, with reflection and transmission coefficients dependent on their polarization [48].

2.2.3 Optical Confinement

To utilize this in finding a correlation between incident angle and propagation, the fundamental notion of *phase-matching* is then used in rectifying the transition in *k.* Since a single eigensolution for wave propagation across all space must be solvable, phase-matching allows the waveform consistency at index interfaces, so at the boundary $z = 0$ a constraint emerges on the propagation constant such that:

$$k_1 \sin\theta_i = k_1 \sin\theta_r = k_2 \sin\theta_t \tag{2.19}$$

The new transmission angle is bound by the set propagation constant. This is the basis for the ray optics approach known as Snell's laws, where from the above it is clear that:

$$\theta_i = \theta_r \tag{2.20}$$

$$\frac{\sin\theta_t}{\sin\theta_i} = \frac{k_1}{k_2} = \frac{n_1}{n_2} \tag{2.21}$$

The incident and reflecting angle of a propagating electromagnetic wave must be the same, while the condition of transmitting into a new material alters the propagation angle dependent on the refractive index ratio [47,48]. Looking at (2.21) further, a condition emerges where total reflection and no transmission occurs. This critical angle condition for the incident angle becomes:

$$\theta_c = \sin^{-1}\sqrt{\frac{n_2}{n_1}} \tag{2.22}$$

It is seen that the argument requires $n_1 > n_2$ for a total reflection condition to exist. Index contrasts can then be designed for total or selective reflection to control the flow of waves, a condition of ray optics that is later manifest throughout all of photonic devices and laser design as *optical confinement*.

When two index interfaces then come together, a step-like index function is made such that optical confinement and thus reflection occur at both interfaces. As shown in Figure 2.3a, this structure contains a central region denoted the core, with index n_{core}, and a set of outer regions that act as the optical barrier called the cladding

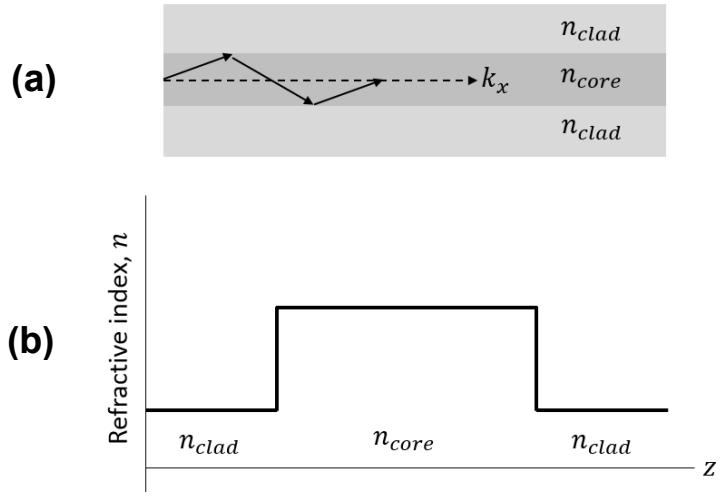

Figure 2.3 Schematic in (a) showing waveguide (or fiber) propagation under total internal reflection. Plot of refractive index profile in (b) for optical confinement in waveguide (fiber) structure

with index n_{clad}. Combined, this produces a guidance path for any electromagnetic wave to follow as shown in Figure 2.3b, thus called a *waveguide*. The electromagnetic wave reflects off each index interface and overall the Poynting vector carries the signal power down the waveguide, as k_x. Various constraints on waveguide dimensions and asymmetries in cladding adjust propagation and attenuation as described later, and for each a critical angle can be found by following (2.22).

With this, the essential guidance properties for wave dynamics are derived and outlined.

2.2.4 Ray Optics Behavior

An important feature of any integrated photonic system is that it must consider and adhere to optical effects over a range of scale. This work represents findings across this range, so for completeness a brief explanation of ray optics phenomena is given.

Building off the findings of effects incurred at index interfaces, an optical layout can be constructed out of optical elements that distributes light accordingly. This is readily used in most experiments and simulation, given the macroscopic intuition seen in its findings. In this, electromagnetic waves can be simplified to a picture of traveling rays that are guided and routed to a desired location by means of lensing and mirroring [50]. This perspective is consistent with all other views of wave dynamics, and is merely varied in scope and scale. Three main effects are observed and thus employed in this perspective: *collimation, divergence*, and *convergence*. Given that the optical output of any semiconductor laser experiences some degree of divergence [49,50], where light spreads outwardly by some angle θ_D, it becomes necessary to employ means for routing light.

Noting this, two main lensing arrangements are emphasized here to construct designs for integrated photonic devices. Shown in Figure 2.4a, a plano-convex lens works to take in light from a diverging source (left side) placed at the focal length, f, of the lens and then refracts it inside the lens until it collimates the source. In Figure 2.4b, a bi-convex arrangement experiences a varied effect where again a diverging source into a lens (left side) is placed and by appropriate spacing the light is refracted through the lens until it arrives focused at the focal length, f, as an object

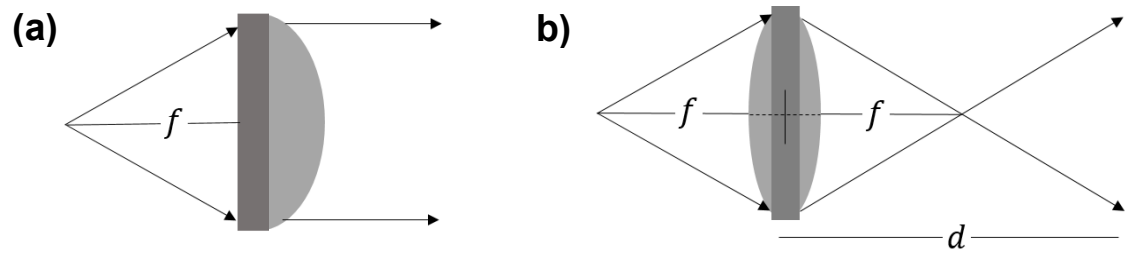

Figure 2.4 Ray optics layout for (a) plano-convex mirror showing collimation of light from the focal point and for (b) biconvex mirror showing a range of focusing light from the focal point.

"image". The bi-convex lens can be thought of as the joining of two plano-convex lens together, and as such a wide range of inward focusing is possible with the bi-convex design.

To construct an optical arrangement for ray optics level work, the concept of *ABCD matrices* is utilized [50]. Noting a focal length , f, the approach to solving out how rays utilizes a matrix approach that considers an emitting source's aperture radius, r_{in}, and its diverging slope, r'_{in}, to find a formalized net result as:

$$\begin{bmatrix} r_{out} \\ r'_{out} \end{bmatrix} = \begin{bmatrix} 1 & 0 \\ -\frac{1}{f} & 1 \end{bmatrix} \begin{bmatrix} r_{in} \\ r'_{in} \end{bmatrix} \tag{2.23}$$

This is in effect the familiar "lens maker's equation" for relating the foci of a source and its "image" output [50]. Similarly, the traversing of waves in the picture of ray optics can be shown to accrue a spatial translation over length d as:

$$\begin{bmatrix} r_{out} \\ r'_{out} \end{bmatrix} = \begin{bmatrix} 1 & d \\ 0 & 1 \end{bmatrix} \begin{bmatrix} r_{in} \\ r'_{in} \end{bmatrix} \tag{2.24}$$

Finally, a matrix formulation of Snell's law as it pertains to refraction in a new material can be shown to bend light as:

$$\begin{bmatrix} r_{out} \\ r'_{out} \end{bmatrix} = \begin{bmatrix} 1 & 0 \\ 0 & \frac{n_1}{n_2} \end{bmatrix} \begin{bmatrix} r_{in} \\ r'_{in} \end{bmatrix} \tag{2.25}$$

In this, the previous index interface phenomena are consolidated into a single linear algebra operator. It is now seen easily that for given index contrasts, a varied degree of refraction is expected.

Together, this effect manifests as a serial set of alterations to the ray path of the propagating waveform, each caused by a deliberate index change or geometric interface. The goals of focusing or collimating a beam path can be designed on a component basis for effective control of signal light, as discussed further in Chapter 3. This allows for the joining of multiple optical components via the matrix method, with the output of one becoming the input of the next. The reverse-order product of these matrices becomes the net result, allowing for designs such as optically

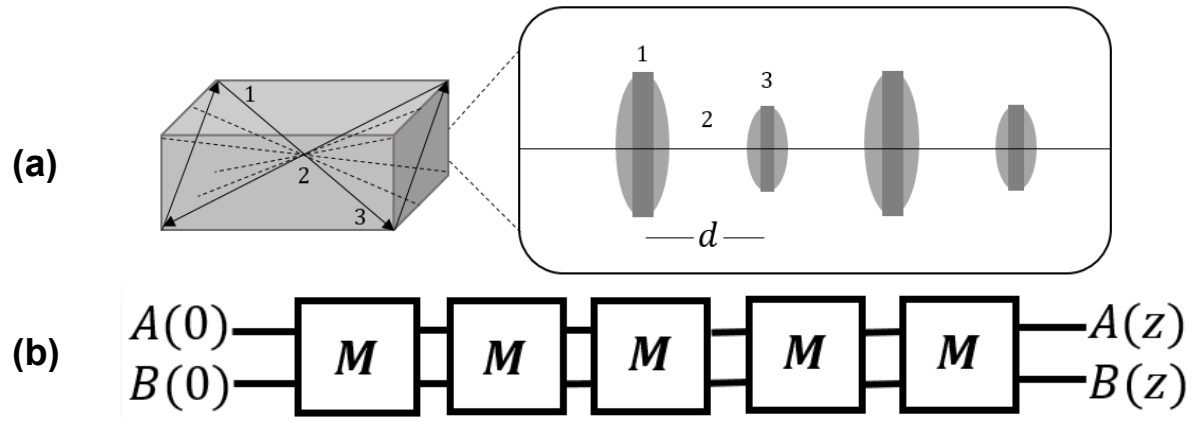

Figure 2.5 Diagram of ABCD method in (a) for a cavity. Each element is defined by its geometries and index. Schematic of a general forward matrix method in (b) for different photonic elements. Each index interface is defined as a transition block for the optical mode or rays, similar to the ray optics ABCD approach.

confining cavities, collimating structures, and perturbative feedback arrays that can be constructed in an "add/drop" manner of individual interfaces. Figure 2.5a details this, where the surfaces of a laser cavity can be reconstructed as a set of repeating lenses, each which contributes to the product of matrix terms. In Figure 2.5b, this same effect lays the foundation to the *forward transfer matrix method* as discussed in Chapter 4, where again an optical input is unitarily evolved by a set of independent, linear transformations M over a total distance, z [48]. The ABCD matrix effect is powerful in that the same ray optics approach can be applied equally across all integrated photonic designs.

2.2.5 Modal Behavior

The next scale of importance in formulating integrated photonic structures is that of investigating modal confinement and distribution. The nature of optical confinement by index interfaces of high-to-low steps can be extended to a more formal definition whereby a material contrast mediates modes of electromagnetic waves.

To produce modal behavior, one can first consider the symmetric slab waveguide model. Shown in Figure 2.6a, the slab waveguide of thickness d propagates light along z and experiences parallel boundaries along the x-axisk, with a common cladding index on either side. It is first recognized that the propagation constant must now dictate propagation along all three cardinal directions, so:

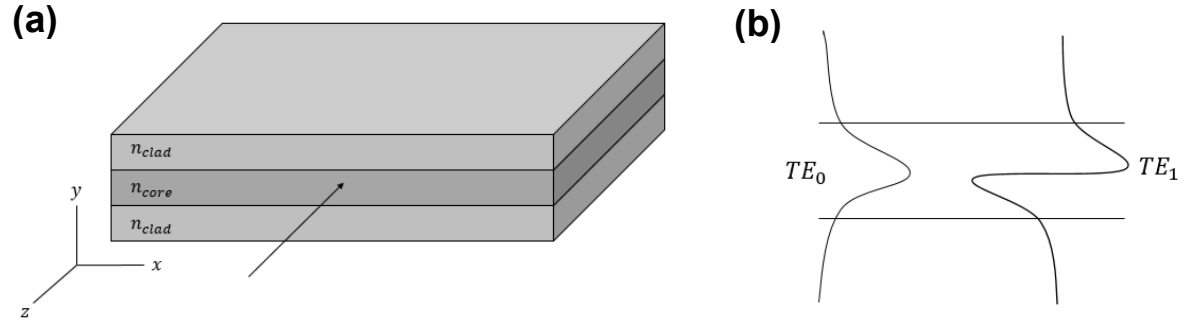

Figure 2.6 Slab waveguide model shown in (a) for photonic signal propagation. It is seen that the core is confined by cladding. Plot of the waveguide distribution shown in (b) for first two modes.

$$k^2 = k_x^2 + k_y^2 + k_z^2 \tag{2.26}$$

Since the propagation constant is intimately related with the refractive index of a material, it then becomes helpful to note an additional constraint on the propagation constant, known as the *dispersion relation* [47, 48]:

$$k_x^2 + k_y^2 + k_z^2 = \omega^2 \mu \varepsilon \tag{2.27}$$

The dispersion relation simply relates the summation of propagation constants back to the Helmholtz equation by matching it to material and frequency parameters. Looking at the figure, it is clear that material variation occurs over y, propagation occurs in z and no propagation or confinement is seen in x. As such, a coupled set of equations is found:

$$k_{y,core}^2 + k_z^2 = \omega^2 \mu_{core} \varepsilon_{core} \tag{2.28.1}$$

$$-\alpha_{y,clad}^2 + k_z^2 = \omega^2 \mu_{clad} \varepsilon_{clad} \tag{2.28.2}$$

where $-\alpha$ is chosen to designate the propagation constant inside the non-confining cladding, for $y \geq d/2$. Matching terms at each boundary, an electric field ansatz is therefore found to produce a standing wave solution inside the wave-guiding structure and a decay function outside of it:

$$E_x = \begin{Bmatrix} Ae^{-\alpha_{y,clad}\left(|y|-\frac{d}{2}\right)} \\ B\cos(k_{y,core} y) \end{Bmatrix} e^{ik_z z}, \qquad \begin{matrix} y \geq d/2 \\ y \leq d/2 \end{matrix} \tag{2.29}$$

This is represented in Figure 2.6b for the first two harmonics of the standing wave. Since the electric field is now completely transverse to the direction of propagation pointing in x, as before this is denoted a TE_m mode, where m is for a harmonic term in the standing wave. A similar derivation produces TM_m modes.

Applying boundary conditions at the index interfaces, a set of guidance conditions emerges that dictates how each mode propagates in the index core. The relation for the cladding propagation constant, $\alpha_{y,clad}$, finds:

$$\alpha_{y,clad} = \begin{Bmatrix} \frac{\mu_{clad}}{\mu_{core}} k_{y,core} \tan(k_{y,core} y) \\ -\frac{\mu_{clad}}{\mu_{core}} k_{y,core} \cot(k_{y,core} y) \end{Bmatrix} \tag{2.30}$$

In this, both even and odd solutions are found. Intersecting this is the relation establishing the contrast between the core and cladding refractive indices, found by taking the difference between the dispersion relations in (2.28):

$$R = \frac{d}{2}\omega\sqrt{\mu_{core}\varepsilon_{core} - \mu_{clad}\varepsilon_{clad}} = \frac{d}{2}k_0\sqrt{n_{core} - n_{clad}} \tag{2.31}$$

The intersection between the two finds the relation for which modes are sustained and propagated in a particular index contrast of core and cladding [47]. The confinement factor, Γ, for each maintained mode thus describes how much is contained within the cladding [48], or:

$$\Gamma = \frac{\int_{inside} \mathrm{Re}\{E \times H\} \cdot \hat{z}\ dy}{\int_{total} \mathrm{Re}\{E \times H\} \cdot \hat{z}\ dy} \tag{2.32}$$

A larger contrast or a thicker waveguide (d) imply more modes may propagate with better confinement in the same structure. For each sustainable mode, a corresponding $k_{y,mode}$ is found, and with this it is seen that the propagation constant in z can be found by the dispersion relation as:

$$k_z = \sqrt{\omega^2\mu_{core}\varepsilon_{core} - k_{y,mode}^2} = k_0 n_{eff} \tag{2.33}$$

where n_{eff} is the *effective refractive index* for a given sustaining mode [48]. The effective refractive index describes a particular mode, TE_m or TM_m, and how its equi-phase front evolves, constrained by the fact that:

$$n_{core} \geq n_{eff} \geq n_{clad} \tag{2.34}$$

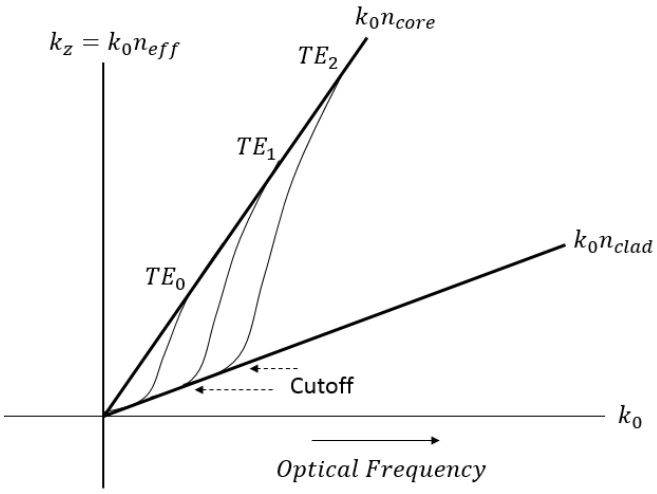

Figure 2.7 Dispersion plot of each slab mode's effective index versus the optical frequency. It is seen that as optical frequency rises each mode will become more confined and have its effective index approach the core.

This presents the next crucial insight in integrated photonic design: all effective indices are then upper-bound by the core, with the fundamental mode having the highest index and each subsequent higher-order mode decreasing in effective index [48]. The effective index of a particular mode increases as the optical frequency increases, steadily approaching the core index (Figure 2.7). A mode containing an effective index smaller than the cladding is thus all imaginary in index, highly dissipative, and will not propagate [48]. This idea enables waveguide designs to be tailored for single mode designs, whereby a cutoff condition exists for every mode when $k_z \to 0$, so $k_y \to \alpha$ as it becomes evanescent into the cladding, causing the dispersion relation for any particular mode m to be bounded by

$$m\frac{\pi}{2} < k_0 d\sqrt{n_{core}^2 - n_{clad}^2} < (m+1)\frac{\pi}{2} \tag{2.35}$$

Taking this principle to other geometries, the slab waveguide model of modal confinement can be extended for rectangular waveguides. This formalism is more useful since a rectangular waveguide allows for finite dimensions in both x and y for the same propagation in z. In such a case, optical confinement exists for both cross-sectional transverse directions, so modes are now identified by two modal numbers, p and q. Further, given that the boundary conditions along each index interface do not cause the electric field to vanish, phase matching requires that neither electric nor magnetic field components reside entirely transversely. As such, what presides are hybrid modes, denoted HE_{pq} and EH_{pq}, where both electric and magnetic fields maintain a component along z and the modal characteristics depend on whether the electric or magnetic terms are dominant [48].

2.2.6 Effective Index Method

To approach this solution, the *effective index method* can be used. In this method, a cross-sectional form of a rectangular waveguide is divided into nine index-interfaced segments, each of which partially contributes to optical confinement. Shown in Figure 2.8a, a typical rectangular waveguide arrangement consists of free-space confinement along the sides and a cladding substrate underneath the core. Considering just the HE_{pq} ($E^x{}_{(p+1)(q+1)}$ dominant) modes first, a set of three vertical slab waveguide approximations are solved separately as shown in Figure 2.8b. In this, the outer segments produce slab waveguides of solely free-space while the central slab waveguide is asymmetric of thickness d confined by free-space (n_0) and the cladding substrate ($n_{substrate}$). By a coupled set of boundary conditions, the resulting equation finds a transcendental equation in terms of $k_y d$ that can solve for the effective index of each vertical slice [48]:

$$k_{y,center}d = \tan^{-1}\left(\frac{\mu_{center}\cdot\alpha_{y,upper}}{\mu_{upper}\cdot k_{y,center}}\right) + \tan^{-1}\left(\frac{\mu_{center}\cdot\alpha_{y,lower}}{\mu_{lower}\cdot k_{y,center}}\right) + p\pi \tag{2.36}$$

Since k_z is common between all dispersion relations, the propagation constants in y can be found as:

$$\alpha_{y,upper} = k_0\sqrt{n_{eff}^2 - n_{upper}^2} \tag{2.37.1}$$

$$\alpha_{y,lower} = k_0\sqrt{n_{eff}^2 - n_{lower}^2} \tag{2.37.2}$$

$$k_{y,center} = k_0\sqrt{n_{center}^2 - n_{eff}^2} \tag{2.37.3}$$

This process is iterated for all three vertical slices into "effective" slab waveguides. A dispersion plot can then be produced from this, much like for a slab waveguide, where the figure of merit is the overall effective index, n_{eff}, within each vertical waveguide for each allowable mode. Then, using this effective index for each vertical waveguide as an input, a single horizontal slab waveguide is constructed, as shown in Figure 2.8c. In this form, any variations

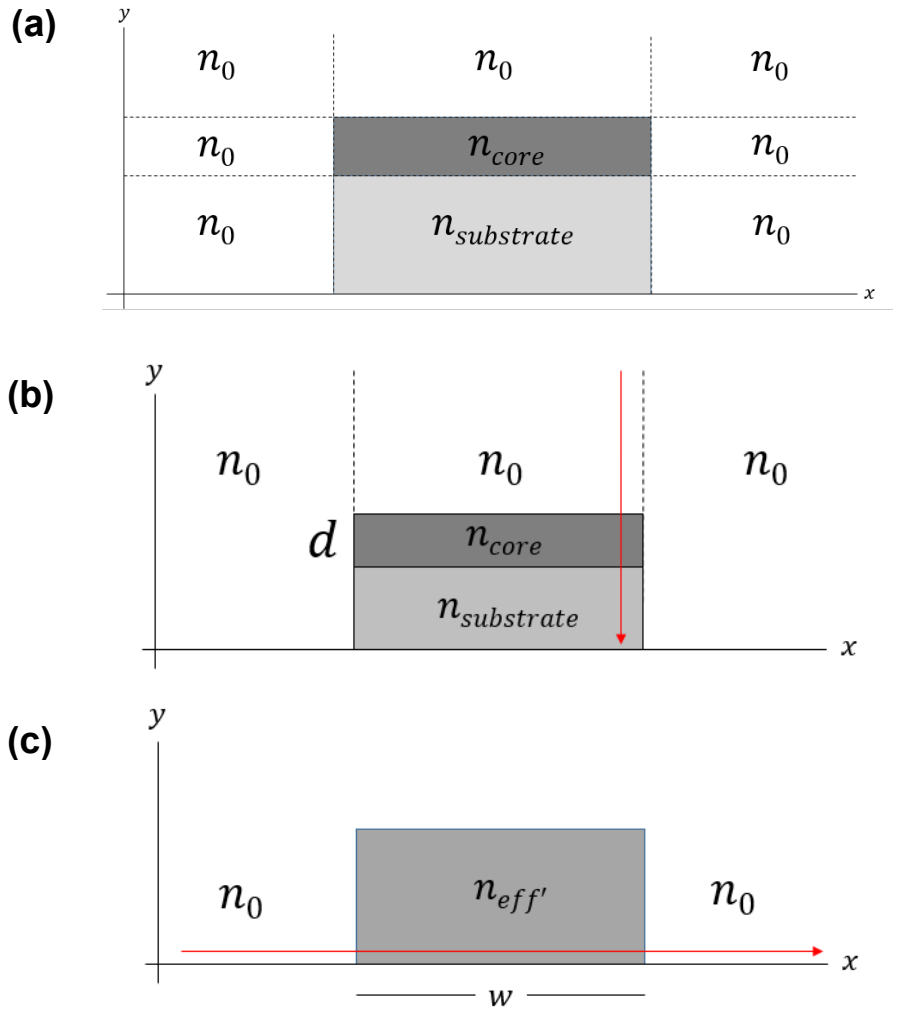

Figure 2.8 General setup in (a) for a rectangular waveguide using the nine-section effective index method. The first step of the method is shown in (b) where each vertical index stack is solved as one slab waveguide, while the final step is shown in (c) where each effective horizontal piece is solved together as one slab waveguide.

captured vertically are now reflected in a set of three effective indices utilized horizontally [48]. This form is then solved over the waveguide width w for $k_x w$, as:

$$k_{x,center} w = \tan^{-1}\left(\frac{\varepsilon_{eff,center} \cdot \alpha_{x,right}}{\varepsilon_{eff,right} \cdot k_{x,center}}\right) + \tan^{-1}\left(\frac{\varepsilon_{eff,center} \cdot \alpha_{x,left}}{\varepsilon_{eff,left} \cdot k_{x,center}}\right) + q\pi \tag{2.38}$$

Again given the common dispersion relations to the one k_z associated with power flow, additional constraints can be utilized:

$$\frac{\varepsilon_{eff,center}}{\varepsilon_{eff,right}} = \frac{n_{eff,center}}{n_0} \tag{2.39.1}$$

$$\frac{\varepsilon_{eff,center}}{\varepsilon_{eff,left}} = \frac{n_{eff,center}}{n_0} \tag{2.39.2}$$

$$\alpha_{x,right} = k_0 \sqrt{n_{eff,total}^2 - n_{eff,right}^2} \tag{2.40.1}$$

$$\alpha_{x,left} = k_0 \sqrt{n_{eff,total}^2 - n_{eff,left}^2} \tag{2.40.2}$$

$$k_{y,center} = k_0 \sqrt{n_{eff,center}^2 - n_{eff,total}^2} \tag{2.40.3}$$

The final dispersion plots can be made by solving (2.38) for $n_{eff,total}$, which is the overall effective modal index within the given rectangular structure, across an optical frequency sweep. A most effective way of formatting this relation is by expressing the net result in normalized coordinates of $\beta \; vs. V$, where:

$$\beta = \frac{n_{eff,total}^2 - n_0^2}{n_{core}^2 - n_0^2} \tag{2.41}$$

$$V = k_0 d \sqrt{n_{core}^2 - n_0^2} \tag{2.42}$$

By this, the asymmetric cladding contrast is utilized as a normalization parameter in both the frequency sweep's dependence on waveguide parameters (V, or the V-number) and the normalized effective index contrast, β.

Given this process, it is clear that the ability to solve for which modes confine and propagate in a structure is a crucial hallmark in designing integrated photonic devices. This enables a clear understanding as to the frequency-dependence of modes.

2.2.7 Finite Element Solvers

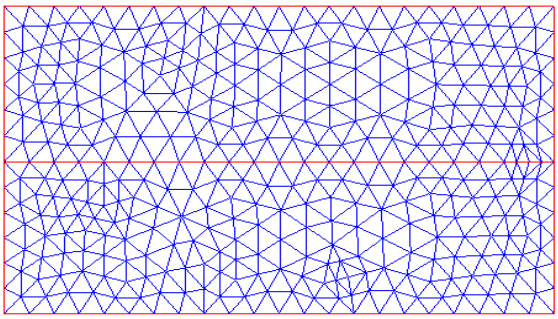

Figure 2.9 Distribution of elements across waveguide to produce computational mesh for FEM solvers.

While the effective index method unveils dispersion trends for each optical mode, the geometric patterns and relative intensity of each mode are still inexact. To this, the use of the *finite element method* (FEM) enables a clear understanding of modal density within any material geometry. FEM uses familiar boundary condition relations of electromagnetics in a sparse-matrix solver that can describe the entirety of an electromagnetic wave's spatial and temporal variation [51]. This method serves as an extraordinarily convenient tool for exacting the necessary beam properties of a propagating or oscillating mode, relevant for integrated photonic designs.

The setup for an FEM solver is straightforward and involves the discretization of a medium into an elemental *mesh.* As represented in Figure 2.9, a waveguide-like geometry can be filled with a solvable mesh of dense, triangular, gridded areas; the resolution of the FEM solver depends on the density of the elements in the mesh, where each element contributes an eigensolution.

The system is then solved as a unified system, where the interaction of all elements in the mesh are simultaneously analyzed and distributed. To do this, the overall geometry can be thought of as a set of functional forms describing the electric and magnetic field distribution, each matched to one mesh element, and thus the intent is to find this consistent set of parameters that describe the modal eigenvalue and match at each boundary accordingly [47]. By this, a set of differential operators can be related to this set of unknown functions that define the eigenvalues of the mode, as:

$$L\varphi = f \tag{2.43}$$

where L encompasses all possible differential operations available in all mesh elements, f is the initial applied source on any given mesh element, and φ is the set of unknown functions that outline the mesh element solutions. Finding φ is the intent of the FEM solver. These unknown functions are thus simplified and related to an established set of basis functions as [51]:

$$\varphi = \sum_{j=1}^{N} c_j v_j \tag{2.44}$$

where c_j are a set of coefficients that constrain, confine, and correlate the functional form of each basis function, v_j. With this general form, a piece-wise approach to finding the total eigenvalue distribution is performed by integrating these unknown functions over any elemental area Ω with respective weighting functions, w_i, as:

$$\int_{\Omega} w_i \, L \sum_{j=1}^{N} c_j v_j \;\; d\Omega = \int_{\Omega} w_i \, f \;\; d\Omega \tag{2.45}$$

By invoking Galerkin's method [51], this says that w_i can be made equal in functional form to v_j, or $w_i = v_j$, meaning that the Hilbert space associated with the weighting functions is equivalent to the basis function space. In total, this allows a grouping of the basis function interpolations multiplied by the desired expansion coefficients to equal the source terms.

To perform this, the Helmholtz equation of (2.5) is set up into a basis function form, where all source terms are eliminated and instead the field along the propagation direction, E_z, is used:

$$\nabla_t \cdot \left(\frac{1}{\mu_r} \nabla_t E_z\right) + \; k_0^2 \epsilon_r E_z = 0 \tag{2.46}$$

This then produces a set of linear basis functions that can be found by integrating them together to stand as the full differentiation over the overlap area of any given element, edge, or node as

$$\int \int_{\Omega} w_i \left(\nabla_t \cdot \left(\frac{1}{\mu_r} \nabla_t E_{z,j}\right) + \; k_0^2 \epsilon_r E_{z,j}\right) d\Omega = \; 0 \tag{2.47}$$

Finally, the outer boundary conditions in the mesh that border or cross any index-interface are additionally constrained by continuity and differential continuity conditions, so the final weak-form representation of the FEM computational solver determines the overlap between mesh terms for a given set of scalar boundary conditions as [51]:

$$\int \int_{\Omega} \left(\frac{1}{\mu_r} \nabla_t E_{z,j} \cdot \nabla_t w_i - \; k_0^2 \epsilon_r w_i E_{z,j}\right) d\Omega = \oint_{\Gamma_D} \hat{n} \cdot \left(w_i \frac{1}{\mu_r} \nabla_t E_{z,j}\right) d\Gamma + \oint_{\Gamma_N} \kappa_N w_i \, d\Gamma \tag{2.48}$$

where Γ_D and Γ_N cover all continuity and differential continuity boundary conditions, respectively, along the desired domain surface. Further explanation in how to then assemble basis functions is explored in [47].

Figure 2.10 explains how the FEM process works in fact. In this, each global element (Figure 2.10a,b), each global edge (Figure 2.10c,d), and each global node (Figure 2.10e,f) of a particular dense mesh are used to interpolate

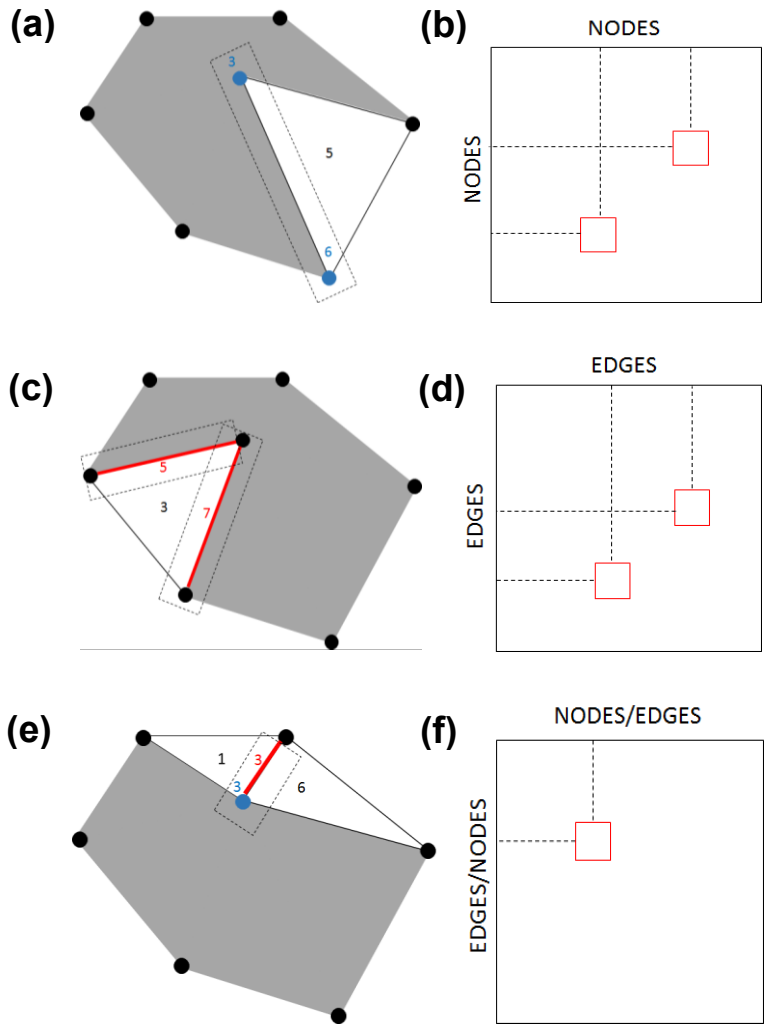

Figure 2.10 Node-node overlap depiction (a) and matrix (b), edge-edge overlap depiction (c) and matrix (d), and edge-node overlap depiction (e) and matrix (f)

the unknown functions that overlaps a set index interface or geometry, constrained only by Maxwell's equations and phase-matching boundary conditions. This means that each element, edge, and node is made to relate to each neighboring element, edge, and node, creating a matrix of interaction terms. A sparse matrix necessarily results given the relatively few neighbors per interface, a main advantage in the FEM computational solver's speed. Each element is then interpolated by a set of overlapping linear basis functions, $N_i^{(e)}$, each centered and maximized on one node, i, while overlapping a maximum of six neighboring elements that are locally solved, as shown in Figure 2.11.

The final result of the FEM computational solver run produces a consistent set of eigensolutions and matching eigenvalues. These eigenvalues match to the modes present in a given waveguide structure, dependent on its index interfaces and its geometry [51]. It is then up to the user to sift through all possible eigenvalues found and determine which ones correspond with a real effective refractive index, as any imaginary effective indices will expectedly dissipate and can be discarded. An example solution is shown in Figure 2.12, where a partially filled waveguide containing an upper half of free-space and a lower half of silicon dioxide (SiO_2, $n=1.5$) is confined inside a metallic

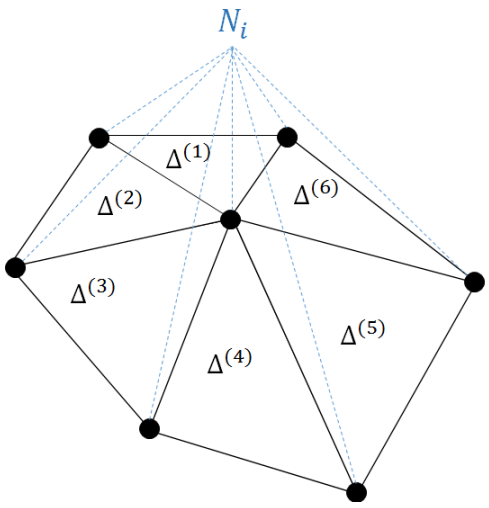

Figure 2.11 Basis function, N_i, construction across overlapping mesh elements of area Δ in solver.

cavity; given the higher index of the SiO_2, this higher order EH_{11} mode shows that the propagating light optically confines to the lower half of the waveguide with only minimal spread into the free-space.

Together, this then shows the most relevant electromagnetic theory and various solving methods for solving complex structures relevant for integrated photonic designs.

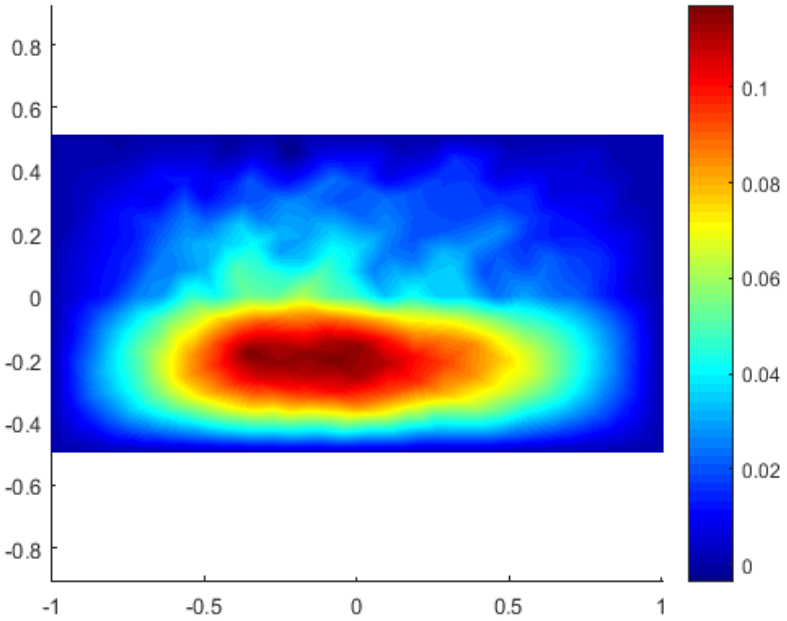

Figure 2.12 Solution showing the eigenmodes of a half-filled dielectric rectangular waveguide. Each eigenmode produces a spatial electric field distribution and an effective optical frequency of propagation. The effective index can be solved by back-solving from a particular mode frequency, useful for cutoff conditions.

2.3 QUANTUM MECHANICS

2.3.1 Particle Dynamics

It is now pertinent to discuss the next set of phenomena available with the behavior of light. While now understood to be a propagating wave in a classical electromagnetics picture, a breakthrough occurred in physical understanding whereby it was found that light must also exist in particle-form, in radical departure from prior convention. And so the photon was born, the fundamental particle of light [52]. To arrive at the significance of photon generation in designing and integrating semiconductor lasers as described in this work, the wave-particle duality of an electron—that which begets the photon—is first required and thus emphasized. It is known that any electron contains both potential and kinetic energy, denoted in a single *time-independent Hamiltonian operator* as [53]:

$$\hat{H} = K + U = \frac{-\hbar^2}{2m}\nabla^2 + V(\vec{r}) \tag{2.49}$$

where ħ is Planck's fundamental constant of quantization, m is the mass of the charge carrier, and $V(\vec{r})$ is the Coulombic potential felt by an electron. The motion of the electron is such that a wave function, Ψ, exists for all possible forms of its travel where a complete summation of these functional eigenstates describes probabilistically where and how an electron's wave propagates, as:

$$\Psi = \sum_n a_n \psi_n \tag{2.50}$$

where a_n represent the coefficients for each orthonormal eigenstate, ψ_n, such that $\sum_n |a_n|^2 = 1$ over a single Hilbert space of possible states [53]. These eigenstates exist delimited by n, the principal quantum number, and correspond to a *discrete eigenenergy level* for the electron. By this, it is further postulated in quantum mechanics that the application of the Hamiltonian operator upon any of these basis function eigenstates extracts the very same Hermitian energy value, known as the time-independent Schrodinger equation [52, 53], or:

$$\hat{H}\psi_n = E_n\psi_n \tag{2.51}$$

where E_n represents the energy eigenvalue for a given electron eigenstate. To then simplify mathematics, a more familiar form known as Dirac notation that takes advantage of eigenstate orthogonality can be employed [53]:

$$\psi_n = |\psi_n\rangle \tag{2.52.1}$$

$$\psi_n{}^* = \langle\psi_n| \tag{2.52.2}$$

$$\langle \psi_m | \psi_n \rangle = \delta_{mn} \tag{2.52.3}$$

where the complex conjugate of a state is marked by the asterisk. This postulate of eigenstates corresponding to eigenenergies thus produces the famous Bohr frequency condition, where the separation between any two eigenstates is a discrete energy difference, or:

$$\Delta E = E_m - E_n = \hbar \omega_{mn} \tag{2.53}$$

where ω_{mn} is the angular frequency, $2\pi\nu_{mn}$, of an emitted photon. As such, the transition in energy between any two electronic eigenstates is facilitated by *photon absorption or emission* [48]. It is here where the profundity of quantum mechanics lends itself directly to integrated photonics, as an elegant mechanism emerges for the deliberate generation of light by transitioning of energy between electronic states. In this, an opportune revelation is seen. The interactions necessary between electronic and photonic semiconductor devices for a scalable system strongly resemble the interactions possible between electrons and photons on a quantum scale.

2.3.2 Quantum Confinement

To design structures capable of efficient production of photons, the same classical methods of phase matching at boundaries can be used on an atomic level. Beginning with an ansatz electronic wave function that looks like a plane wave (2.9), an idealized potential energy boundary can be formed along x as:

$$V(x) = \begin{Bmatrix} 0 \\ \infty \end{Bmatrix}, \begin{matrix} x \leq L/2 \\ x \geq L/2 \end{matrix} \tag{2.54}$$

This is known as the *infinite quantum well* [48]. Inserting this into the Schrodinger equation, a second-order differential equation results that produces a set of fundamental eigenstates of the form:

$$\psi_n(x) = \begin{Bmatrix} \sqrt{\frac{2}{L}} \cos\left(\sqrt{\frac{2mE_n}{\hbar^2}} x \right) \\ 0 \end{Bmatrix}, \begin{matrix} x \leq L/2 \\ x \geq L/2 \end{matrix} \tag{2.55}$$

Here is where the principle of *quantum-confinement* emerges. When an electron's motion is bounded by a potential barrier of energy, a series of confining effects take place where a standing wave emerges for the electron's probabilistic movement [53]. The presence of an electron is therefore constrained to only inside this barrier, measurably only in the regions where its wave function eigenstate may exist and later collapse [52]. As such, a relation between energy

interfaces and index interfaces is apparent; similar to optical confinement, quantum confinement involves the intentional introduction of a separate potential energy barrier.

Given the nature of this analytical solution, the momentum argument inside the sinusoid, where $p = \hbar k$, can further be constrained to the fact that distinct solutions only exist as:

$$k = \sqrt{\frac{2mE_n}{\hbar^2}} = \frac{n\pi}{L} \tag{2.56}$$

where again n is the principle quantum number. At last, the nature of the Bohr frequency relation in (2.53) manifests as a measurable energy for this quantum well as:

$$E_n = \frac{\hbar^2 n^2 \pi^2}{2mL^2} \tag{2.57}$$

where it is now clear that the separation grows between quantized electronic energy eigenstates grows as n^2 and, as such, the exact energy of a corresponding photon can be intimately related to a quantum-confined geometry, as shown in Figure 2.13a. It is also immediately clear that any two *isolated* eigenstates produce zero energy overlap, as its measurable *expected value* average is:

$$\langle \psi_2 | \hat{H} | \psi_1 \rangle = \int_{-\frac{L}{2}}^{\frac{L}{2}} \psi_2{}^*(x) \left(\frac{-\hbar^2}{2m} \nabla^2 \right) \psi_1(x)\, dx = A \int_{-\frac{L}{2}}^{\frac{L}{2}} \cos\left(\frac{2\pi}{L}x\right) \cos\left(\frac{\pi}{L}x\right)\, dx = E_1 \delta_{21} = 0 \tag{2.58}$$

Extending the principle of infinite barriers then, the method remains the same for approaching *finite potential barriers* in a quantum well. It is these that give the most realistic insight for integrated photonic structures. Much like in classic electromagnetics with waveguide barriers, a continuous solution is found that requires both bound terms and decay terms as shown in Figure 2.13b, where for an eigenstate confined by a potential of:

$$V(x) = \begin{Bmatrix} 0 \\ V_0 \end{Bmatrix}, \begin{matrix} x \le L/2 \\ x \ge L/2 \end{matrix} \tag{2.59}$$

the wave functions become:

$$\psi_n = \begin{Bmatrix} Ae^{-\alpha_{x,barrier}\left(|x|-\frac{L}{2}\right)} \\ \mathrm{B}\cos(k_{x,well}y) \end{Bmatrix}, \quad \begin{matrix} x \ge L/2 \\ x \le L/2 \end{matrix} \tag{2.60}$$

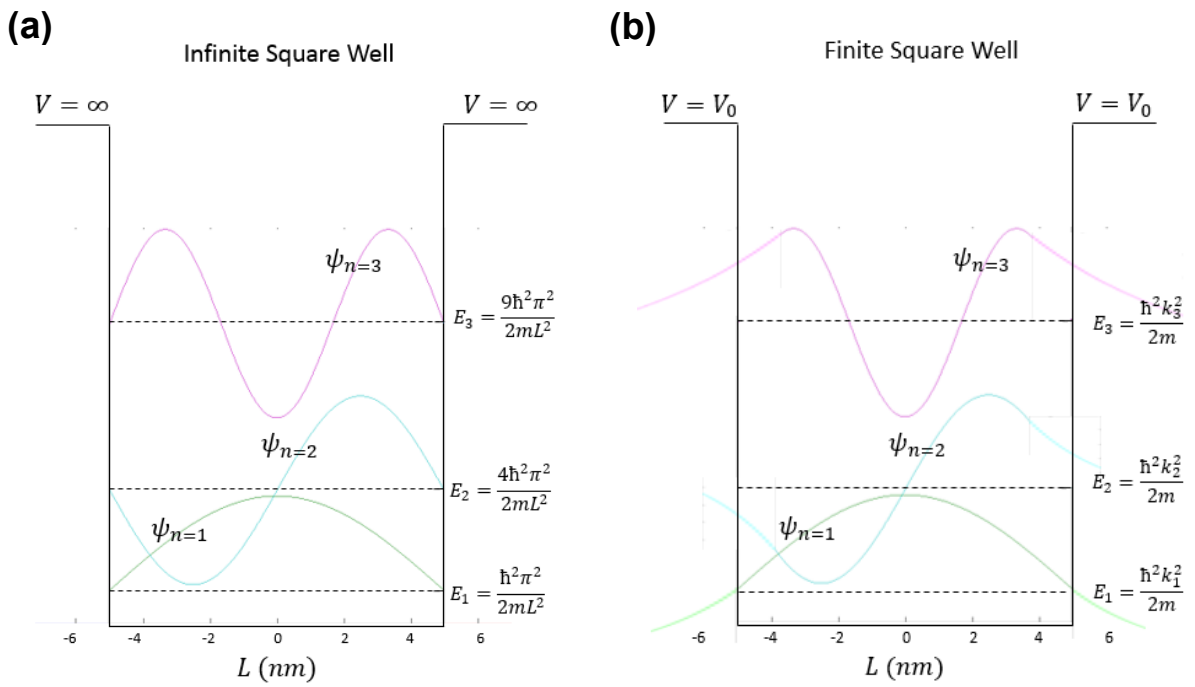

Figure 2.13 Plot of discrete energy eigenvalues and sinusoidal eigenstates for an infinite quantum well in (a), and the discrete energy eigenvalues and piece-wise eigenstates for a finite quantum well in (b).

Again matching phase at boundary conditions as before, the set of solutions is found by a transcendental equation solver that constrains all terms based on continuity and differential continuity boundary conditions [48,53], producing:

$$\alpha_{x,barrier} = \left\{ \begin{matrix} \frac{m_{barrier}}{m_{well}} k_{x,well} \tan(k_{x,well} x) \\ -\frac{m_{barrier}}{m_{well}} k_{x,well} \cot(k_{x,well} x) \end{matrix} \right\} \tag{2.61}$$

where $m_{barrier}$ and m_{well} are the *effective mass* of an electron (or charged particle) in a material [48]. Expounded upon in [53], this effective mass relation becomes crucial in tailoring structures for various photon generating structures. The momentum related to each confined energy level is then solved for by intersecting these even and odd trigonometric equations with a single centric term determined by the potential barrier, V_0, as:

$$R = \frac{L}{2} \sqrt{\frac{2 m_{well}\, V_0}{\hbar^2}} \tag{2.62}$$

By solving for the set of intersecting $k_{x,well} x$ values, the quantized energy levels can be back-solved, noting the relation between E and k in (2.56). The adjusted terms still scale as per their n^2 relation, but the energy level is shifted

slightly down due to the reduced confinement. This allows for integrated photonic designs to create quantum-confined finite square wells and approximate their energy levels as though they were infinite [48].

The idea of quantum-confinement structures enables electronic eigenstates to be knowingly set. The postulates of quantum mechanics set guidelines for how to use small "quantized" dimensions and deliberate material choices, a crucial method for designing efficient semiconductor lasers at particular energy levels as discussed later. With this, the process of extracting transition energy as photons becomes analytically precise.

2.3.3 Perturbation Theory

Taken as fact that eigenstates do not generally interact, a set of principles are found to force temporal interaction between these two atomic levels for coherent generation of photons. A form of Schrodinger's equation is therefore used that uses *time-dependent perturbation* [53], where the overall wave function made is:

$$\hat{H}|\Psi_n(t)\rangle = i\hbar\frac{\partial|\Psi_n(t)\rangle}{\partial t} \tag{2.63}$$

where now a time-dependent change in the total wave function is related to the total energy of the electron. A crucial insertion is made, where a small time-dependent sinusoidal perturbation is added to the static Hamiltonian as [48]:

$$\hat{H} = \hat{H}_0 + \hat{H}' \tag{2.64}$$

$$\hat{H}' = \hat{H}'e^{+i\omega t} + \hat{H}'^{+}e^{-i\omega t} \tag{2.65}$$

The full setup of this Hamiltonian then incorporates the full summation of possible unperturbed eigenstates as (2.50) into the time-dependent operator, but by applying the chain rule of the differential operator, a great deal of simplification occurs and this becomes:

$$\sum_n \frac{\partial a_n}{\partial t}|\psi_n(t)\rangle e^{iE_nt/\hbar} = -\frac{i}{\hbar}\sum_n \hat{H}'(t)a_n(t)|\psi_n(t)\rangle e^{iE_nt/\hbar} \tag{2.66}$$

To constrain this, the overlap of any particular eigenstate ψ_n with a separate state ψ_m (i.e. Fourier's trick) is found by the insertion of $\langle\psi_m(t)|$, so:

$$\langle\psi_m(t)|\psi_n(t)\rangle\sum_n \frac{\partial a_n}{\partial t}e^{\frac{-iE_nt}{\hbar}} = -\frac{i}{\hbar}\sum_n \langle\psi_m(t)|\hat{H}'(t)|\psi_n(t)\rangle a_n(t)\, e^{\frac{-iE_nt}{\hbar}} \tag{2.67}$$

and noting the orthogonality of separate eigenstates, this enforces $n = m$, so:

$$\frac{\partial a_m}{\partial t} = -\frac{i}{\hbar}\sum_n \langle \psi_m(t)|\hat{H}'(t)|\psi_n(t)\rangle a_n(t)\, e^{\frac{i(E_m-E_n)t}{\hbar}} \tag{2.68}$$

where it is now clear that the separation in the two energy levels, $E_m - E_n$, pulls out an atomically resonant angular frequency, ω_{mn}, and that the change in probability amplitude to the upper state, a_m, depends on the lower state, a_n. The field frequency of the perturbing Hamiltonian, ω, is then related to each state, noting a ground state $a_n^{(0)}(t=0) = 1$ and a first excited state $a_m^{(0)}(t=0) = 0$, thus establishing [48]:

$$\frac{\partial a_m^{(1)}}{\partial t} = -\frac{i}{\hbar}\left(\langle H'\rangle e^{i(\omega_{mn}-\omega)t} + \langle H'^{+}\rangle e^{i(\omega_{mn}+\omega)t}\right) \tag{2.69}$$

Integrating through for the probability of any final state as $|a_m|^2$, a final transition rate of any electron between a ground state and an excited state is found as:

$$W = \frac{\partial}{\partial t}|a_m|^2 = \frac{2\pi}{\hbar}|\langle H'\rangle|^2 \delta(E_m - E_n \pm \hbar\omega) \tag{2.70}$$

This is *Fermi's golden rule* for state transition, perhaps the most insightful point yet for the goal of designing photonic devices. It is seen that a reciprocal relationship exists between the ability to electromagnetically perturb an electronic state upward or downward, via the incidence or emission of photons at $\hbar\omega$ that resonate with the electronic transition, $E_m - E_n$ [48]. Given this, the interweaving of electronics and photonics is at its most apparent.

2.3.4 Photon Generation

This relationship enables the core processes central to the design of integrated photonics. Figure 2.14 displays these two processes; their elegance reflects their simplicity. First, the excitation of an electron from a ground state to an excited state due to an incoming photon is *absorption*, leaving behind an absence of negative charge—or *hole*—in the ground state [54]. The *recombination* of the same electron and hole in their respective states is then *stimulated emission*, where a photon that matches coherently in phase, polarization, and photon energy to the perturbing absorbed photon is emitted. A third process of *spontaneous emission* that recombines carriers and emits photons incoherently serves as a crucial precursor to stimulated emission in laser physics. Thus, stimulated emission arises from spontaneous emission and occurs only under the conditions where a *population inversion* of excess electrons into the excited state $|m\rangle$ is reached [50]. Since the field frequency, ω, must resonate with the atomic transition energy frequency, ω_{mn}, photons that are off-resonant will either propagate through if smaller than the atomic transition or will experience heavy phonon dissipation if larger [54].

Detailed derivations exist for the relevant rates of stimulated emission and absorption processes, yet the main takeaway is that the net rate per unit volume of semiconductor goes as [48]:

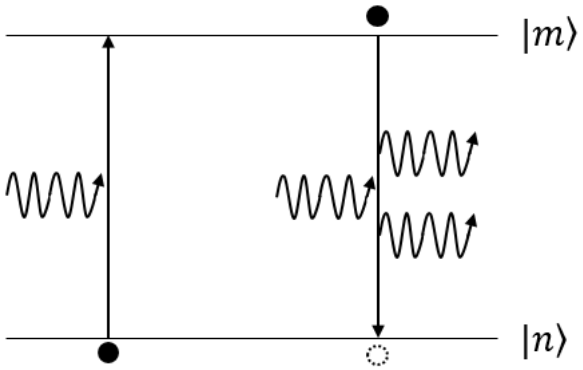

Figure 2.14 Schematic of the quantum mechanical processes of absorption and stimulated emission. On the left, a photon excites a ground state electron (filled-in dot) causing absorption, leaving behind a hole (dotted line dot). On the right, an additional photon hits the excited state electron, causing recombination of the electron-hole pair and causing a second photon to be produced coherently as stimulated emission.

$$\begin{matrix} R_{absorption} \\ R_{stim.emission} \end{matrix} = \frac{2}{Vol.}\frac{2\pi}{\hbar}\sum_{k_n,k_m}|\langle H'\rangle|^2\begin{Bmatrix}\delta(E_m - E_n - \hbar\omega)\cdot f_n(1-f_m) \\ \delta(E_m - E_n + \hbar\omega)\cdot f_m(1-f_n)\end{Bmatrix} \tag{2.71}$$

where the summation is over the density of states while f_m and f_n are the Fermi-Dirac statistics of each energy eigenstate, excited or ground state [54]. Thus, absorption requires occupation in the ground state and vacancy in the excited state, while stimulated emission predictably requires the opposite.

This then outlines the background for how the postulates of quantum mechanics predict the behavior of electron energy levels in quantum-confined structures and how time-dependent perturbation theory allows for the interaction of these levels via absorption, spontaneous emission, and stimulated emission; together, these present the second set of insights necessary for patterning photonic structures in all integrated designs as investigated in this work.

2.4 SEMICONDUCTOR THEORY

2.4.1 III-V Crystals

The final set of background constraints relates to why III-V compound semiconductors pose the best advantages for integrated photonic devices and how the CMOS framework on silicon can be made compatible with this. It has been found through various theoretical studies and x-ray diffraction experiments that semiconductors form into defined crystals [54]. The takeaway from these crystalline forms is that the ordering of atoms in the crystal greatly affects its properties and optoelectronic effects. To then design integrated forms for electronic or photonic functionality, the crystal structure matters.

The first crystal structure of importance is *zinc-blende.* Defined as the interweaving of two face-centered cubic (FCC) structures of either group III or group V elements, the lattice vector separation between these atoms establishes an overlap form with a common lattice constant, a, as shown in Figure 2.15a. The symmetric spacing of all the III-V elements in zinc-blende means that all Coulombic interactions between neighboring atoms and their valence electrons

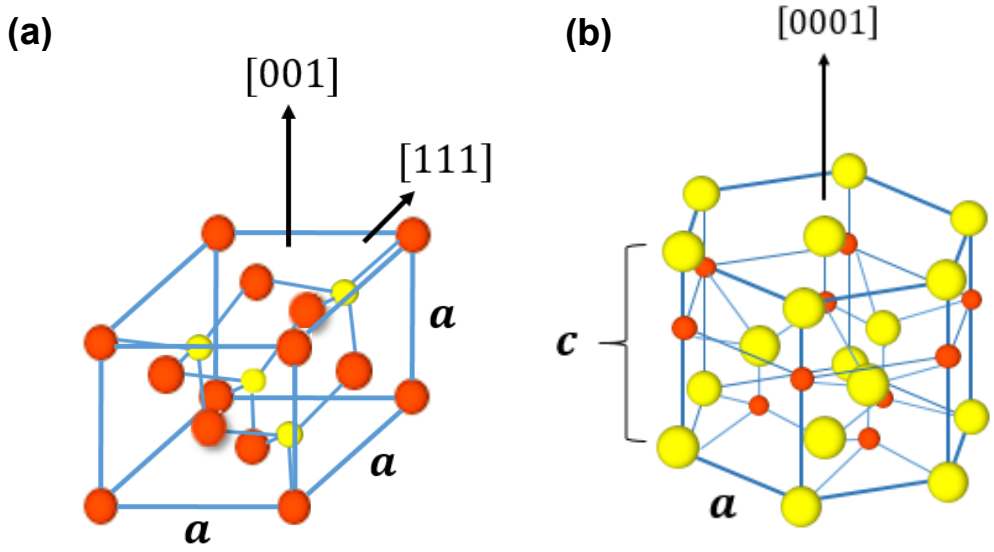

Figure 2.15 Structure of the zinc-blende crystal in (a), where common growth planes are shown, and structure of the wurtzite crysta in (b), where the common growth plane is shown.

is *centrosymmetric*, meaning any lattice effects are spatially redundant and thus spatially cancelling [55]. Thus, the crystal orientation in any device growth is defined by three isotropic axes, where (001) and (111) orientations are most common for varied bonding and emitting characteristics [56]. Many III-V compound semiconductors solidify as zinc-blende, including GaAs, InP, InAs, and their various alloys.

The second crystal structure emphasized for III-V compound semiconductors is *wurtzite*. The wurtzite differs largely from zinc-blende in that the wurtzite is the interweaving of two hexagonal lattices each of a group III or a group V element, as shown in Figure 2.15b. Two lattice constants come about from this, with an in-plane a and vertical c, noting $c = 2\sqrt{2/3}a$. Thus, the lattice is not evenly spaced between all elements, owing to the increased ionicity in the wurtzite group V sites, so Coulombic repulsion does not exactly cancel and thus retain a force, implying that the wurtzite structure is *noncentrosymmetric* [55]. This noncentrosymmetry becomes crucial in later discussions on various anisotropies and higher-order nonlinear effects present in particular III-V material and their application to integrated devices. The wurtzite orientation is therefore defined by four axes, three of which define isotropic 120º rotations in the hexagonal plane while the fourth defines the anistropic c-axis; thus, the most common growth axis is for the anisotropic axis to be normal to the wafer as (0001).

2.4.2 Lattice Energy Bands

The formation of these lattices then produces a reliable understanding of its band properties. While a single electron moving between single atom eigenstates is previously described, the behavior of entire lattices of these same atoms forms *bands* of values. Through detailed derivations explained in other texts [48,57], a periodic wave function inside the lattice—the Bloch wave function—experiences Coulombic potentials at the edge of its every lattice vector. The wave function spatial variation and overlap between any two atoms, taken into the momentum domain of k, produces a set of energy bands where electrons can and cannot reside [57]. From this, the fundamental benefit of the

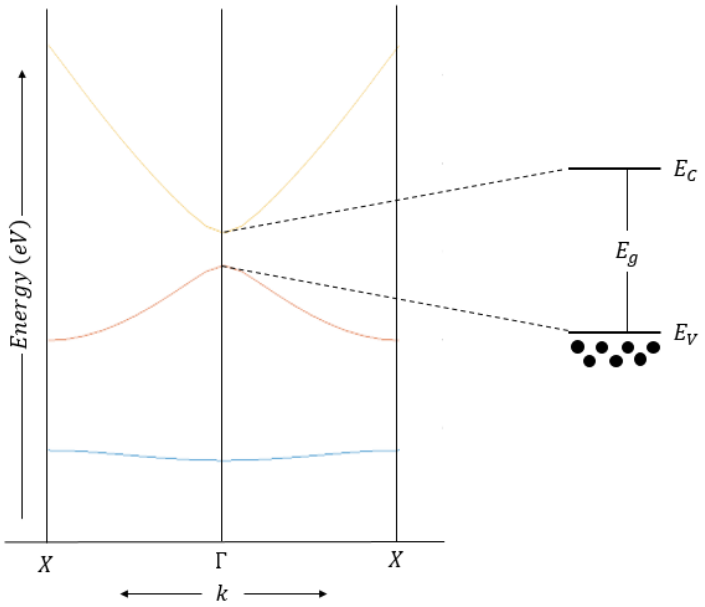

Figure 2.16 Plot of Energy versus momentum (E-k) producing the lattice bands for the first Brillouin zone. The inset shows the direct bandgap that emerges between the uppermost valence and first conduction band.

semiconductor for both electronics and photonics emerges: the *energy bandgap* separates a *valence band,* E_V, for unexcited electrons and a *conduction band,* E_C, for excited-state electrons. The accumulation of electrons in the valence band is the available population for absorption by means of the Fermi-Dirac statistics. Doping of n- or p- type atoms into a semiconductor produces a Fermi level, E_F, that sits within the bandgap and sets the offset between any two materials and their conduction/valence bands [48,54].

In Figure 2.16, an E-k diagram showing the energy and momentum relationship for the different bands is found. Electrons will accumulate in the lowest part of the conduction band once excited, and so in III-V semiconductors the lowest point is at zero electron momentum $k = 0$, or the Γ-point; as such, zinc-blende and wurtzite structures for semiconductors are *direct-bandgap materials* which recombine carriers most efficiently for photon generation [57]. Given the understanding from (2.70) that recombination across eigenstates produces a defined photon energy, it becomes apparent that different wave function overlaps produce different bandgaps, and as such materials can be used to emit specific photon energies [48]. The idea of III-V alloying, where ternary and quaternary alloys of group III or group V elements are interspersed, allows for bandgap engineering for the emission of a particular wavelengths across a wide spectrum [4]. Typical values for specific materials are shown in Table 2.1.

Table 2.1 Values for typical semiconductor bandgaps. The bandgaps are given in terms of eV for energy and μm for the corresponding wavelength.

	Si	GaAs	GaN	AlN	InP	GaP
E_g	1.124	1.424	3.44	6.2	1.344	2.272
λ	1.103	0.871	0.36	0.2	0.923	0.546

2.4.3 Silicon Compatibility

A final consideration is how silicon forms. The structure of silicon solidifies into a modified form of a zinc-blende lattice, known as the *diamond* structure. The two intersecting FCC lattices are both made of silicon, which means the same symmetries and isotropies apply. However, due to the formation of diamond structures and their conversion into the momentum domain, the conduction band is lowest at a non-zero momentum $k \neq 0$, implying electrons will accumulate away from the Γ-point when excited [54]. As such, silicon is defined as an *indirect-bandgap material*, denoting that it is inefficient for recombination and photon generation [57]. By this, it becomes apparent why the combination of III-V materials for photonics and silicon for CMOS electronics is necessary. Photon generation must come from direct-bandgap materials, while silicon has been nearly perfected for the use in memory structures and electronic controls via CMOS. Among III-V materials, further effects can be considered depending on the centrosymmetry of the crystal. Together, this outlines the reasoning for why all electronic-photonic integration benefits from designing with heterogeneous methods in mind.

2.5 LASER PHYSICS

2.5.1 Cavity Conditions

At last, the parameters outlining electromagnetics, quantum mechanics, and semiconductor theory are understood. When these individual wave, particle, and lattice considerations are then overlapped and optimized, a powerful metric emerges that serves as the basis for integrating photonic devices in a single III-V on Si system. To affect one is to affect them all. As such, this culminates in the field of semiconductor laser physics, where the intersection of these principles produces a reliable means of stimulated emission at a given wavelength and into a given modal distribution.

The means of extracting a beam of coherent photons as *lasing* lies in three characteristics: a carrier *pump*, a *cavity*, and a *gain medium*. This corresponds to a means of electrically driving a time-dependent excited state for both holes and electrons, an optically confined *Fabry-Perot cavity* structure, and a QW capable of population inversion above a specified bandgap energy (in eV) [48,50]. A Fabry-Perot cavity, as shown in Figure 2.17, consists of a three-dimensionally confined space that is confined on either end by reflecting mirrors [50]. This produces phase-matching boundary conditions, as described before in (b), where an accumulated phase φ over a particular cavity length L will experience *resonance* and constructively interfere for a particular set of periodic electromagnetic waves to build up a standing wave over multiple reflections. This means a gain in field over one cavity roundtrip in z will occur but will remain bounded by losses and by the phase condition of the cavity [48], as:

$$1 = |r_1||r_2|e^{(\Gamma g_{th} - \alpha_i)L + i(2k_z L + \varphi_1 + \varphi_2)} \tag{2.72}$$

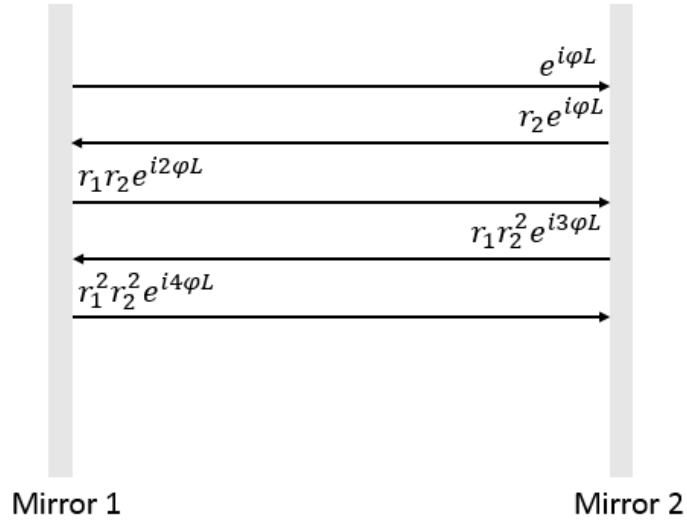

Figure 2.17 Depiction of Fabry-Perot cavity, where a resonance condition emerges for a given set of frequencies as continuous reflections off each mirror produce constructive inference in the phase.

where $|r_1|$ and $|r_2|$ denote the overall reflection coefficient for each end facet of a semiconductor laser, and the accumulated net gain minus losses goes as $(\Gamma g_{th} - \alpha_i)\, L$. This first produces from the propagating terms that:

$$2k_z L + \varphi_1 + \varphi_2 = 2\pi \cdot m \tag{2.73}$$

where only resonant propagation constants will remain. From this it can be solved that the separation between any two resonant propagation constants longitudinally along the cavity length abides by:

$$2\left(\frac{2\pi\Delta\nu}{c}\right) n_{eff} L = 2\pi m \quad \longrightarrow \quad \Delta\nu = \frac{c}{2n_{eff}L} \tag{2.74}$$

The longitudinal mode spacing creates a *free spectral range (FSR)* of possible longitudinal frequencies that resonate with the cavity. A longer cavity produces a denser packing of these possible cavity frequencies, constrained only by length and total effective refractive index, implying that a change in the effective refractive index along the cavity can move between longitudinal modes.

2.5.2 Gain Spectra

Constraining this further, though, are the exponential growth and decay terms that find:

$$\Gamma g_{th} = \alpha_i + \frac{1}{2L}\ln\left(\frac{1}{R_1 R_2}\right) = \alpha_i + \alpha_m \tag{2.75}$$

which defines the critical parameter of *gain threshold,* Γg_{th}. This says that for the system to lase, an optically confined gain threshold must be reached such that it overcomes losses per length related to its intrinsic material, α_i, and related to its individual mirror losses per length, α_m [48]. As such, increasing cavity length reduces mirror losses per length

but increases intrinsic losses per length, while the reflection of each facet directly changes the quality of the cavity's *photon density*. To this point, the gain threshold defines the maximum for electrically pumped stimulated emission, such that the QW experiences population inversion, gain clamps at threshold, and lasing occurs. This threshold emerges from (2.70) as a relation for the gain spectrum, g, as:

$$g = \frac{q^2}{2\nu n_{eff} c\varepsilon_0 m_0^2} \cdot \frac{2}{Vol.} \cdot \frac{m_r^*}{\pi\hbar^2 L} \cdot |\langle H' \rangle|^2 \cdot \delta(E_m - E_n - \hbar\omega) \cdot (f_C - f_V) \cdot H(\hbar\omega - E_{hn}^{em}) \qquad (2.76)$$

where the initial factors come from relating the stimulated emission rate per output power per photon energy ($R_{stim}/(P_{output}/\hbar\omega)$), and the density of states for QWs produces a Heaviside step-function $H(\hbar\omega - E_{hn}^{em})$, that grows as integer multiples of $m_r^*/\pi\hbar^2 L$. It is seen that the conditions necessary in a cavity for lasing depends not only on its effective length and effective index, but also on the particular material chosen to define the energy eigenstate separation for a photon energy value and thus the gain spectrum possible with that design. Any integrated photonic design must match the cavity to what the material energy separation will allow.

2.5.3 Electrical Conditions

The transition in energy that defines the photon is now instead from QW electron eigenstate, em, to QW hole eigenstate, hn, as E_{hn}^{em}, a value necessarily greater than the bandgap. To produce this, electrical pumping must be sufficient to separate out electron and hole carriers into their quantized conduction and valence *bands*, respectively [48]. Thus, an electrical potential is applied across the gain region such that the Fermi level that defines midpoint carrier occupation statistics of each material is split, pinning *quasi-Fermi levels* to a separation of $F_C - F_V$. This produces the guideline for population inversion as:

$$F_C - F_V > E_{hn}^{em} \left(= \hbar\omega_{output}\right) \qquad (2.77)$$

where the energy separation in quasi-Fermi levels that occur with electrically-driven minority carrier injection (i.e. an applied junction bias) must be greater than the separation in the QW energy eigenstates that produce stimulated emission photons. As such, a quasi-Fermi level separation in semiconductor lasers requires a separation in carrier occupation and thus consideration for p-i-n doping [48]. Figure 2.18 shows this sufficiently, for a p-i-n structure under bias. This means that across the QWs, a double heterostructure material layering must be formed, where typically a p-i-n diode of a p-type hole injector, an intrinsic region for the QWs, and an n-type electron injector together form the semiconductor laser electrical pump and gain region. Other recent novel designs employ an n-p-n design for improvements in gain threshold and electrical controllability [33], but for the purposes of this thesis what is important is merely the interface.

This completes the understanding of the background of how semiconductor lasers exist as a matter of intersecting multiple viewpoints of theory and design. A gain region defined by a QW must be chosen to match to a particular output wavelength by bandgap engineering for initial spontaneous emission, while the laser cavity design around this gain must be separately constructed in index and length to produce the desired set of longitudinal modes

that resonate within the gain in order to reach stimulated emission from spontaneous emission. To conclude this background, it helps to look at what this all means for designing photonic devices in the broader scope of electronic-photonic integrated circuitry. The constraints now imposed show why the bonding onto CMOS silicon is important for fabrication and scalability, yet also why methods for enabling material compatibility over a wide range of III-V materials for gain or controls is necessary to densify the use of optical signals. The capabilities therefore available to the engineer in designing integrated electronic-photonic systems rest on the ability to consider the theoretical and empirical needs in heterogeneous material interfacing across sensing, cavity tuning, and fabrication layout topics.

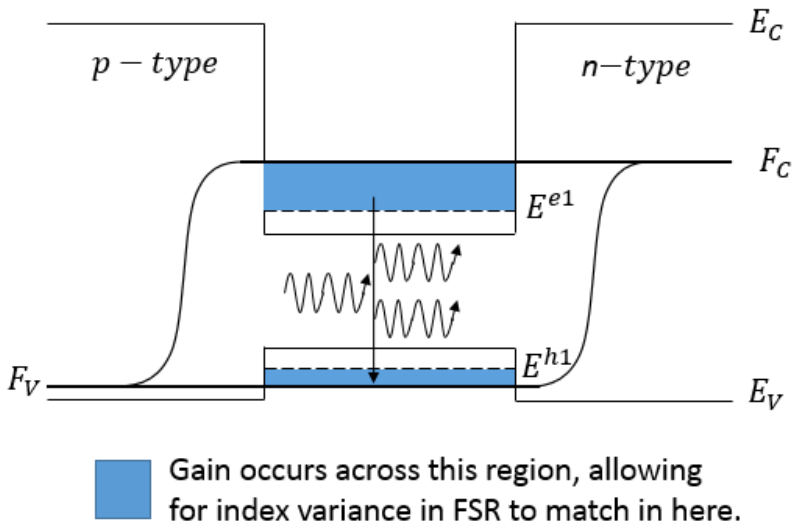

Figure 2.18 PN-diode laser structure where a QW of smaller bandgap is sandwiched in between two barrier layers of larger bandgap. This quantization causes discrete energy eigenvalues to emerge inside the quantum well, pushing upward where electrons can accumulate via their density of states. Electron injection is shown by the use of each barrier being oppositely doped (p or n) and an applied bias causing the quasi-Fermi levels to be pinned apart. The range of photon gain for stimulated emission as defined in (2.77) is shown in blue by being lower-bound by the first energy eigenstate's density of states and by being upper bound by the pn-diode bias condition, $F_C - F_V$. Population inversion results where a single optical frequency with a photon energy lying across the blue regions will experience gain and lase.

CHAPTER 3: SENSING METHODS AND RESULTS

"I think the light of science is so dazzling that it can be evaluated only by studying its reflection from the absorbing mirror of life; and life brings one back to wildness."
-Charles Lindbergh, 1967

3.1 MOTIVATION

The significance of any integrated photonic system rests on its ability to both transmit and receive optical stimuli. To enable optical sensing for real-world applications, this requires that the system be able to resolve a signal's signature and fashion it accordingly. Given the nature of light having a relation between its amplitude and its wavelength, a most pertinent means of sensing is by the use of a spectrometer, where a signal can be spread out into a weighted wavelength spectrum. One of the growing areas for spectral sensing is point-of-use testing, where a specified light source is directly paired with a particular biological or chemical assay and the resulting signal variation after passing through the assay is sensed and collected for immediate results [58]. Point-of-use testing has seen implementation across industries where resolvable signal variations can optically denote the presence or absence of a chemical attribute, useful in the areas of food safety, colorimetric water quality monitoring, and pathogen detection [59,60]. These devices point a direction forward in bioelectronics and biophotonics, structured around the ability to discern the spectral signatures of a particular materials [61]. Yet the key barrier that consistently emerges in these is the lack of a compact integration strategy for these devices; in short, a system optimized in portability, versatility, and ease of use would greatly improve adoption of these devices and their techniques [58]. Such a system is the focus of this work.

The goal then is to determine a method best capable of integrating together the necessary optical emitters, electrical circuitry, and the collecting optics for a miniaturized spectrometer platform. Since versatility is key, a constraint is proposed that the integrated system be made compatible with a CMOS electronic platform. Given the prevalence of CMOS image sensors in available consumer electronics—where a dense pixel array made of silicon photodetectors and a matched lens array can collect photons in a spatial manner for image capture—the design intent of this integrated electronic-photonic system is to make it match to a CMOS image sensor as its platform. Compared to a tabletop spectrometer based upon a diffraction grating, where a long propagation distance is necessary for good spectral resolution, the integrated photonic system can be placed directly on a photodetector array with satisfactory resolution and a greatly reduced device footprint [62]. A point-of-use sensor can then be made rapidly deployable and integrable as part of a handheld smartphone platform for a wide range of assays and their matching photonic emitters.

This work presents the completed findings in designing a CMOS-compatible miniaturized spectrometer system that is capable of signal emission and detection for wide-band sensing. The major findings included detail the layout and design of the components, the initial proof-of-concept testing, the simulation results for the optical arrangement, the fabrication results, and the final testing confirming the vitality of a miniaturized spectrometer as compared to an available spectrometer and optical spectrum analyzer (OSA). A completed sensing platform that

straddles the electronic control and photonic signal domains results [62]. This process and its findings represent the first step in producing methods for heterogeneous electronic-photonic integration.

3.2 LINEAR VARIABLE FILTER

3.2.1 Design

As an integrable approach is desired, one popular method of reducing the footprint of the tabletop-scale diffraction gratings and long monochromator lengths in spectrometers is to employ a compact linear variable filter (LVF). The LVF is a dielectric-based distributed Bragg reflector (DBR) that has contained inside its growth a set of linearly-graded cavities [63]. The DBR denotes a series of high-low refractive index steps between thin-film dielectrics, which causes a series of reflections at each index interface as described in Chapter 2. Ordinarily a DBR stack would therefore produce a uniform reflection and transmission effect across a wavelength spectrum, which would allow a uniform intensity through the structure, but the inclusion of a series of linearly-graded cavities between the DBR stacks made out of the same dielectric steps causes a spatial variation to occur. Instead, the linear grade causes the LVF to resonate at different wavelengths as they each match to the varying filter thickness, causing a particular LVF to match to a particular wavelength range [62]. In this work, a set of two LVFs is used, allowing for a wide-band of detection while still maintaining high spectral resolution as compared to single LVF wide-band designs. For an appropriate range in sensing for this integrated photonic device, the two are chosen and purchased (JDSU) to be specified for single wavelength transmission across the range:

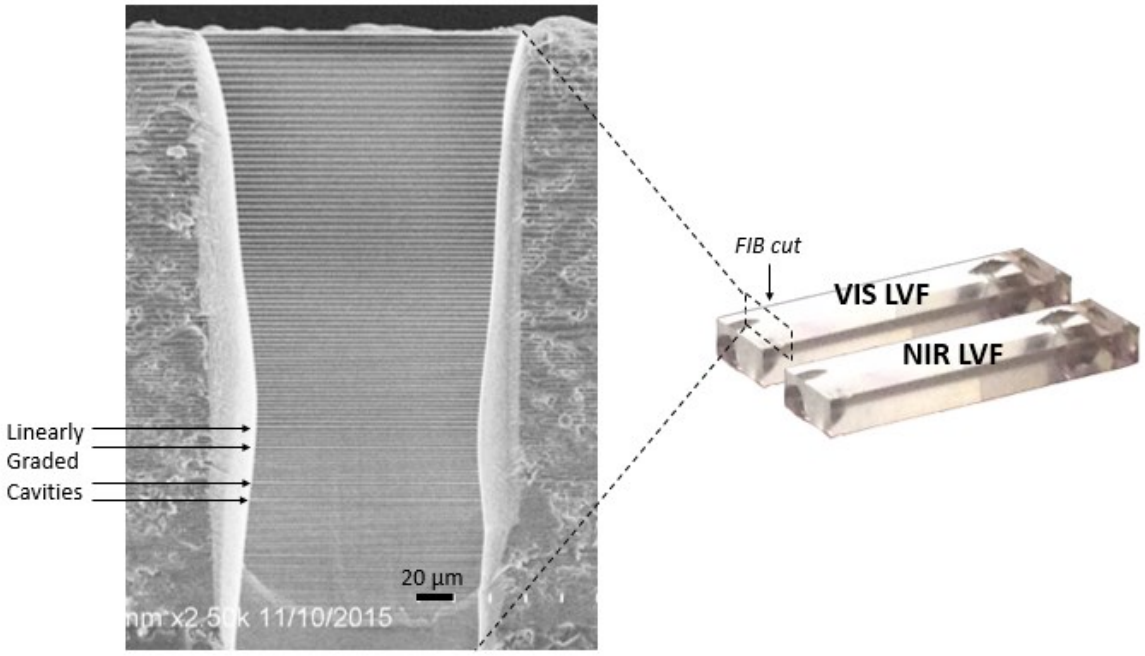

Figure 3.1 SEM cross-section of LVF DBR layer structure. It is clear that a periodic change in the layer material is accompanied by a set of cavities that break that periodicity, here shown as a single cut of the gradient. The relative scale is shown for comparison to the overall LVF size.

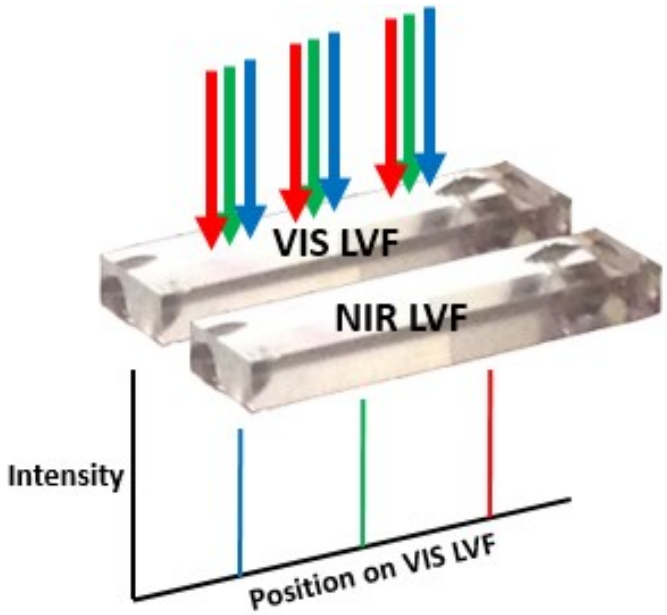

Figure 3.2 Diagram of expected transmission from polychromatic sources onto LVF. Bandpass filtering is seen.

$$\text{Visible (VIS) LVF}: \quad \lambda_{VIS} = 400\,nm - 700\,nm \tag{3.1}$$

$$\text{Infrared (NIR) LVF}: \quad \lambda_{NIR} = 630\,nm - 1080\,nm \tag{3.2}$$

The design of each LVF is shown in Figure 3.1, where a picture of the LVFs along its gradient axis is shown next to a scanning electron microscope (SEM) cross-section of the very same. This SEM was achieved by performing a focused-ion beam (FIB) cut into the top of the LVF at a specified location, as discussed later. The FIB cut was designed to penetrate the top side of the LVF containing the DBR and its etalon cavity coating, whereas the rest of the LVF is transparent silica.

A spatially-dependent optical band-pass filter is therefore produced, whereby a spatially varying Fabry-Perot resonance effect is felt along the length of the LVF, producing transmission peaks such that a specific wavelength passes at a specific location. This is shown in Figure 3.2, where it is expected that monochromatic sources would transmit at one specific spatial location on the LVF while polychromatic sources would spread and produce a series of transmission peaks that vary in amplitude in correlation to that spectral component's relative intensity. Noting the previous discussions denoting the changes in reflection for oblique incidence, it is seen that proper usage of the LVF *requires normal incidence* of all signal light for proper sorting and spatial-spectral conversion. This produces a set of conditions that allow for a spectral separating effect, allowing the LVF to act as a highly condensed spectrometer insofar as it allows for spectral resolution.

3.2.2 Filter Characterization

To consider this spectral resolution and to begin characterizing the LVF as an integrable photonic component, a series of initial tests is performed on the LVFs to better understand their spatial gradient. Each LVF has initial dimensions of 12 mm (length) x 3 mm (width) x 1.5 mm (thickness). Yet it is expected that the desired spectral

detection range (λ_{VIS} or λ_{NIR}) is inclusive in that length, implying that excess dielectric is on either end of the specified range. Noting the behavior of DBR reflectivity spectra, additional lobes of transmissivity are present outside of the specified range due to resonant higher order harmonics [63], so the first step is to trim back the LVF so it does not exceed the detection range in dielectric. This additionally has the benefit of allowing the LVF to better fit, lengthwise, on a CMOS image sensor.

This characterization is performed by employing a tabletop spectrophotometer to produce a set of transmission measurements for each LVF. The spectrophotometer tool works by using a focused reference laser beam and a focused analysis laser beam, such that an initial pair of reference measurements are taken with 1) nothing in either path to denote full transmission, or an upper threshold, and 2) a dark absorbing block in the analysis path to

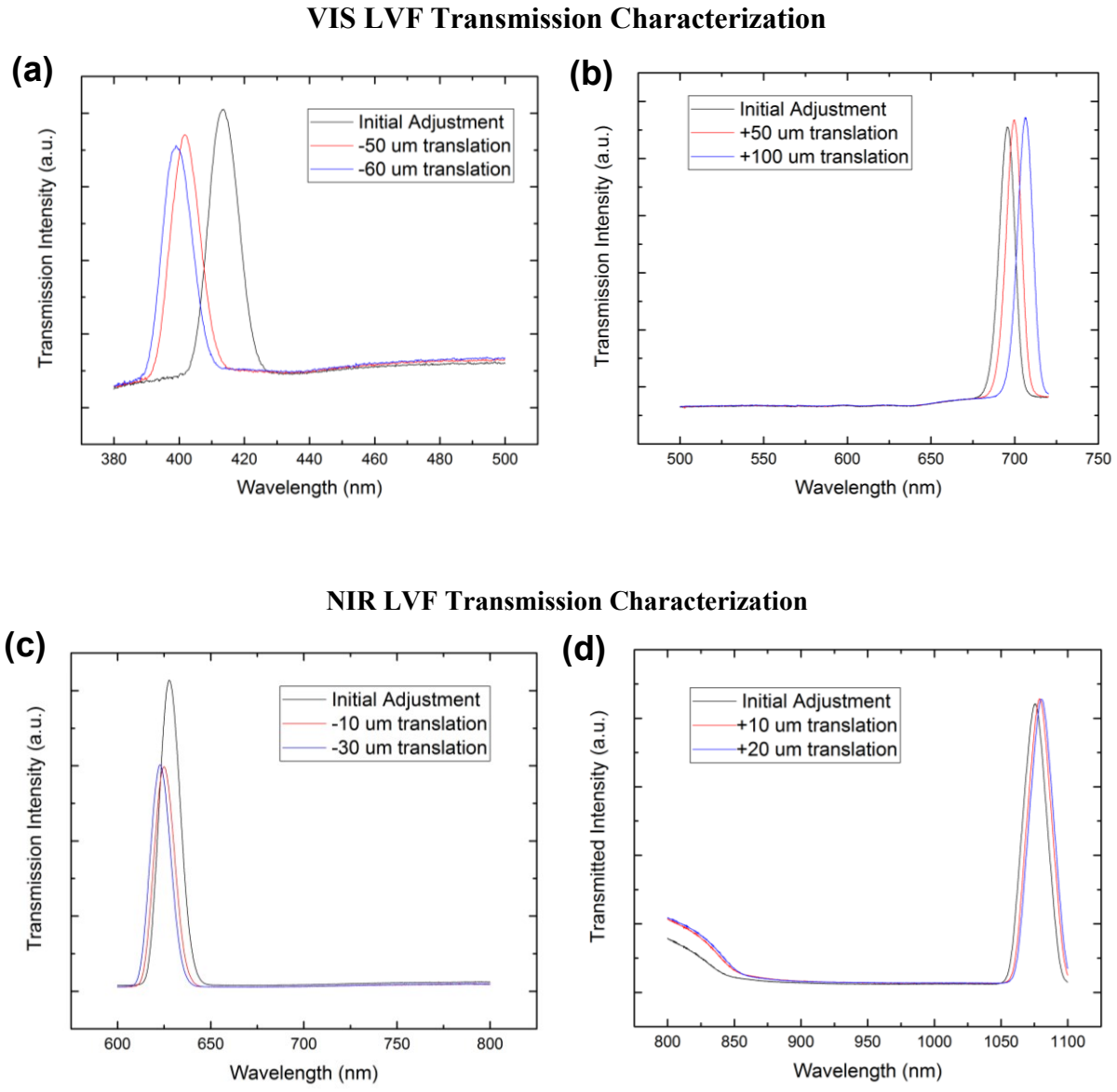

Figure 3.3 Plot of relative transmission (%) of VIS LVF on spectrophotometer at (a) short and (b) long λ. Plot of relative transmission (%) of NIR LVF on spectrophotometer at (c) short and (d) long λ.

denote a zero point, or a lower threshold. Together, this outlines the allowed range of transmission sensitivity for the spectrophotometer's calibration. Following this, the focused analysis beam is set to a particular wavelength range via the internal software and is then aligned so that it is focused with normal incidence right onto the LVF at a particular location along its length axis. The alignment is set up in a way so that the LVF is attached to a translation stage that can be adjusted by a manual knob whose tick marks match to micron resolution. A sweep across the expected range of the LVF, either VIS or NIR, then produces a transmission plot. Shown in Figure 3.3a through Figure 3.3d, the resultant transmission intensity confirms the effect of the LVF: namely, that a highly selective DBR pass-band filter is constructed that allows for significant suppression of transmission everywhere but at a specified wavelength. The intersection of the focused beam with the point on each LVF that corresponds with a desired transmitted wavelength (i.e. for the VIS LVF at 400 nm and 700 nm, for the NIR LVF at 630 nm and 1080 nm) is then marked for later adjustment. It is seen that the FWHM resolution of each LVF, as shown in Table 3.1, is:

Table 3.1 Tabulated results of FWHM found

	Short wavelength FWHM	**Long wavelength FWHM**
VIS LVF	11 nm	11 nm
NIR LVF	14 nm	25 nm

The resolution of the NIR LVF is lower than the VIS LVF, yet still comparable. This information on overall spectral resolution presents useful insight as to whether the LVF or later the CMOS will provide the limiting factor in spectral resolution.

3.3 CMOS IMAGE SENSOR

3.3.1 Characterization

While the LVF performs the task of spreading out different spectral components in a single wave-packet of sensing data, it is the CMOS image sensor that is necessary for full detection. Here the ability to integrate electronics and photonics becomes key. As described before, the nature of the CMOS electronic structure allows for a camera-based photodetector array to be formed, again used because of the advantages and versatility in fabricating silicon CMOS for electronic designs. Once the LVF separates out the transmitted components, a CMOS image sensor (as in Figure 3.4a) is set up to immediately intake the light spatially along its pixel array, thus providing programmable means for reading out the spectral distribution of a light source by simply looking at the CMOS's spatial distribution. So it is critical to devise a method of reliably and scalably attaching the LVFs to the CMOS image sensor for sufficient analysis, shown in Figure 3.4b.

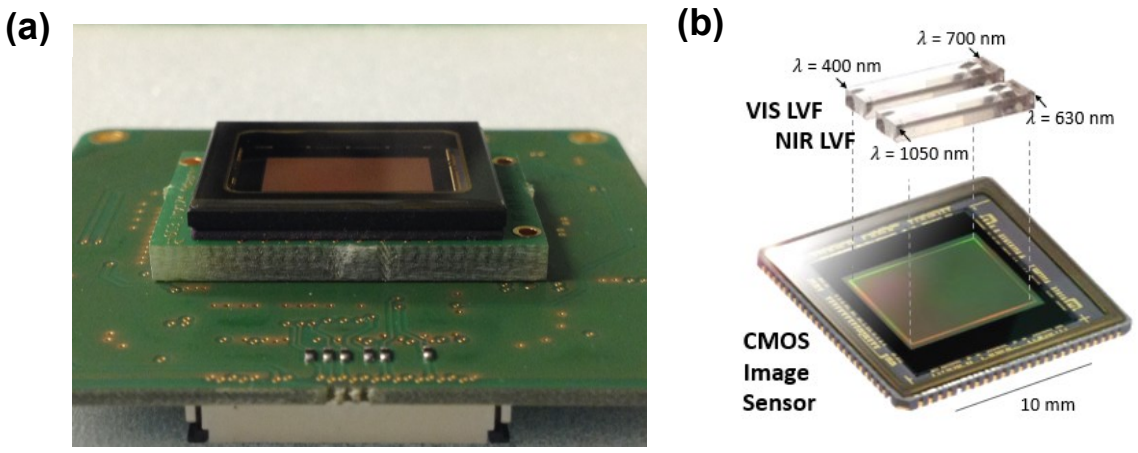

Figure 3.4 Photo of CMOS image sensor utilized for heterogeneous optical design in (a) and schematic of design layout in (b), bonding multiple LVFs to the CMOS for integration.

Two setups are employed for the integrated sensing designs. The first uses a PixelLink CMOS image camera where the two LVFs are attached with simple adhesive atop the camera cover-glass to prepare a system for proof-of-concept testing of the LVF in comparison to other spectrum-analyzing instruments, including an OSA. This initial testing utilizes a benchtop setup with free-space optics as needed to effectively control the incident light onto the LVF and CMOS such that it is normally incident. The second design is the complete integrated design. Built congruently with the first system but on two separate ONSemi IBIS4-6600 CMOS image cameras (2210 x 3002 active pixels), this design directly bonds the LVFs onto the CMOS image sensor pixel array to assure maximal coupling into the pixel array and. Analytical points from the first stage act as a precursor to the second stage.

Utilizing the first CMOS image sensor, a series of initial benchmark calibrations are taken to analyse the LVF spectrometer setup. A set of monochromatic sources are aligned and collimated into the LVFs using a set of free-space optics components. Starting with the VIS LVF, a HeNe laser source with a known optical wavelength is shined onto the sensing device and used for calibration of spatial-spectral conversion. Centered at λ = 632.8 nm, the HeNe laser source is then sent into the tabletop OSA (0.05 nm spectral resolution) and resolved to have a source linewidth of 0.11 nm. The corresponding pixel-equivalent linewidth is found by examining where on the CMOS pixel array the source emerges and then performing a Gaussian fit function on the results to produce a pixel-equivalent resolution of 38 pixels. This produces a spatial-spectral conversion ratio (CR) of:

$$CR_{VIS} = 10.07\ \frac{\text{pixel}}{\text{nm}} \tag{3.3}$$

Shown in Figure 3.5a, an actual snapshot of the CMOS image sensor detection is shown for the HeNe source. Taken with minimal background lighting, the CMOS image sensor successfully places the HeNe wavelength in a predictable position along the LVF and then into the CMOS image sensor for collection. A crop of the image along the gradient axis of the LVF, limiting the region of image processing to just the region desired, allows for the conversion ratio to then be applied to the pixel count for producing a *corresponding wavelength* distribution. This becomes the figure of

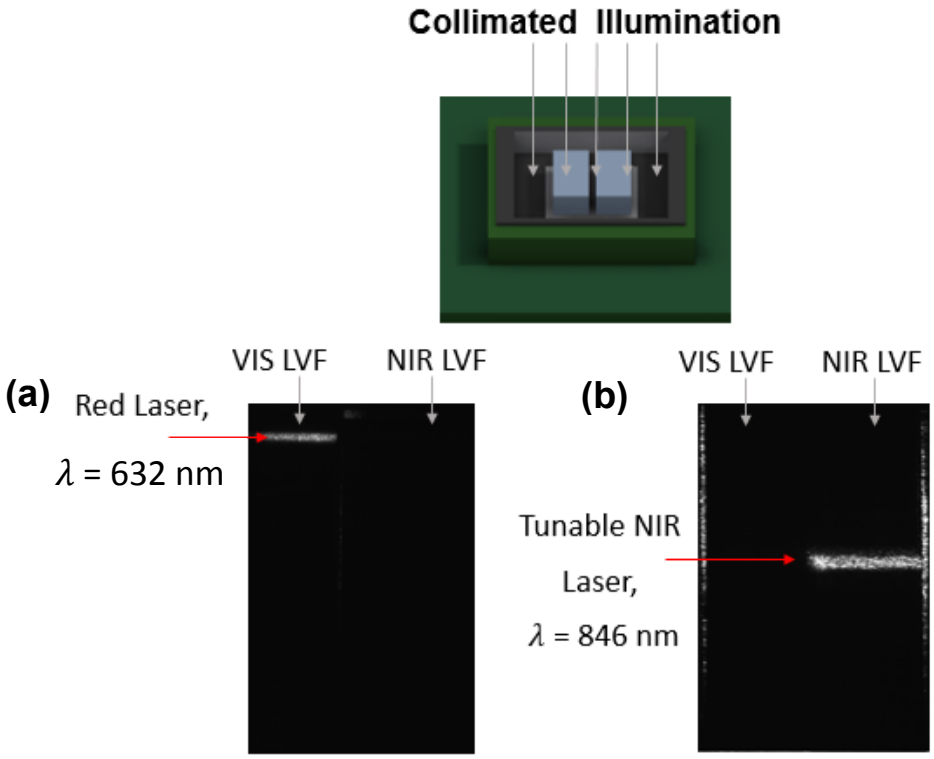

Figure 3.5 Photo from integrated CMOS setup for calibration, showing pixel linewidth of a HeNe laser source through the VIS LVF in (a) and pixel linewidth of IR laser through the NIR LVF in (b).

merit for all LVF-based spectrometer measurements: exacting the wavelength spectrum from the CMOS image sensor intensity counts. Moving to the NIR LVF, a tunable laser source, λ =835 nm – 855 nm, is collimated into the system and again read by the OSA for comparison. From the OSA, the tunable laser has a resolvable linewidth of 0.16 nm, and when collected into the NIR LVF, the pixel-equivalent resolution is seen to be 45 pixels. This again produces a spatial-spectral conversion ratio unique to the near-infrared spectrometer, as:

$$CR_{NIR} = 7.40\ \frac{\text{pixel}}{\text{nm}} \tag{3.4}$$

In Figure 3.5b, this effect is shown. The tunable laser source is seen to produce a single illumination peak along the LVF, which will then be interpreted in post-processing in terms of intensity counts seen by the CMOS (monochrome: 0-255). A similar process is carried out for the second set of LVFs for the second CMOS image sensor, upon their bonding.

3.3.2 Bonding Strategies

The second set of CMOS image sensors is therefore prepared for the integrated design. Noting the previous work on the spectrophotometer in determining the exact point on both ends of both LVFs where the wide-band sensing range ends, a series of measurements are prepared for readying the LVF for dicing. This is then followed by the LVFs

(a) (b)

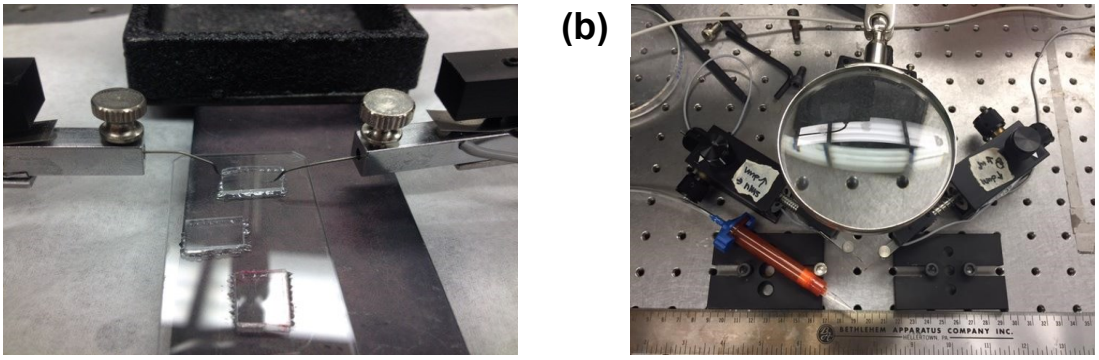

Figure 3.6 Initial experiments for testing epoxy bonding for CMOS image sensor in (a) and final setup for accurate epoxy bonding for integrated optical design in (b).

being bonded to the CMOS image sensor directly in order to determine the viability of the heterogeneous integrated platform.

To prepare the VIS and NIR LVFs for dicing, a series of cleanroom-based techniques is employed for repeatable and suitable procedure. The LVFs are each brought under a microscope so that the initial mark made on each from the spectrophotometer testing may be traced and extended around the full dielectric. This allows for proper alignment of the mark for when the system is diced. The resulting sizes for both LVFs are made to be trimmed to less than 10 mm in length, noting that the OnSEMI CMOS image sensor is 10 mm (length) x 7.5 mm (width) in size. Following this, the LVFs are wax-bounded at $250° C$ to a carrier glass slide with the DBR/cavity side of the LVF face down into the wax. A coating of photoresist (PR) is then spun onto the LVFs to protect the surface, whose excess dielectric side faces up. The positive PR used is S1813, which reliably produces a 1.3 μm coating when spun on at 3000 rpm for 30 seconds. The carrier wafer is then baked at $110° C$ for 1 min, with the final setup brought to the dicing saw for trimming. Using a semiconductor-grade resin bond diamond dicing blade with sufficient exposure and 400 grade mesh, the LVFs are then diced in single pass lines and examined under microscope for any harsh striations. Finally, the PR is washed away with a standard acetone-IPA degrease while the wax is then removed via heat and a degrease.

The LVFs are then readied for bonding by preparing their alignment along the CMOS image sensor. The intent in bonding is to attach each LVF by using minimal adhesive, noting that too much adhesive could potentially cover a wide span of the pixel array, thus distorting its individual cell lensing. A UV-curable bonding epoxy is therefore purchased and paired with an electronic fluidic dispenser (EFD). The EFD is designed to control the flow of the adhesive, and a careful set of test trials are used to test the speed of the dispensing system. Running at 0.2 seconds of disbursement, the LVFs are then dabbed along their sides and each LVF is directly bonded directly onto a separate CMOS image sensor pixel array. This separation is to aid in experimental handling, where the intent is still maximal integration. A UV cure of the epoxy follows, with approximate exposure times being around 2 min. The experimental setup for this preparatory procedure is shown in Figure 3.6a and 3.6b, where the LVF is affixed and held in place by various optical bench tools.

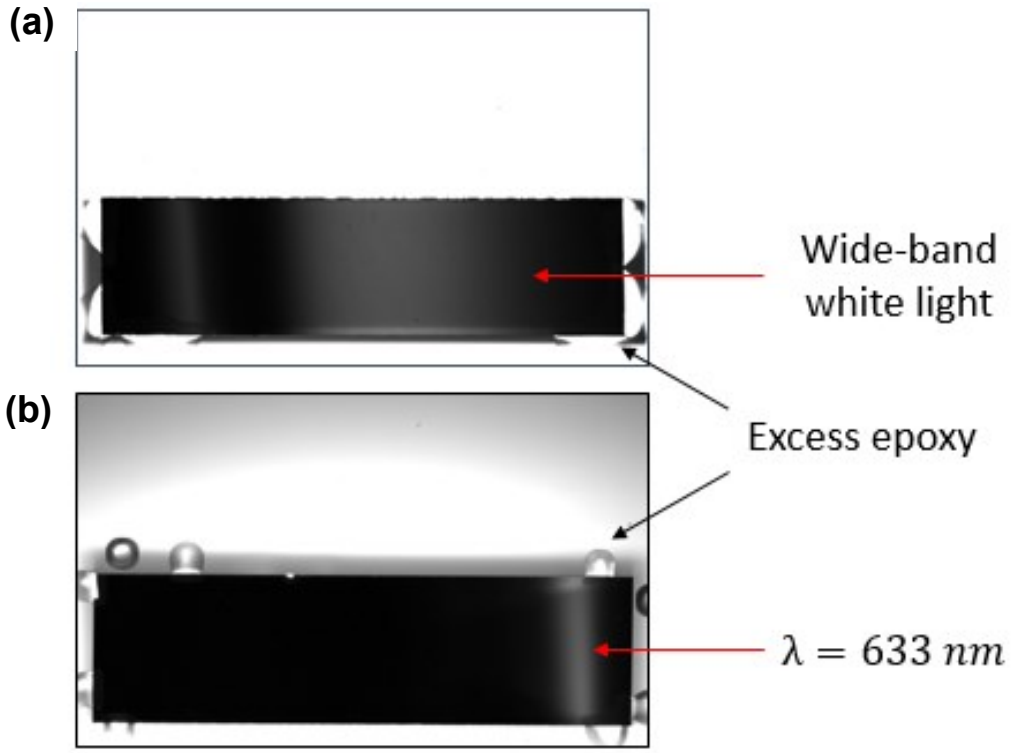

Figure 3.7 Raw image results of bonded VIS LVF in (a), confirming ability to detect wide-band source, and results of bonded NIR LVF in (b), confirming ability to resolve fine linewidth.

3.3.3 CMOS Analysis

The results of the bonding of the LVF onto the CMOS image sensor are shown in Figure 3.7a,b as part of a capture suitable for image processing. It is seen that, while excess epoxy is visible on each CMOS image capture, this is not blocking any of the relevant range of either CMOS image sensor, which is along the length of the LVF gradient. The range of detection post-dicing is simultaneously shown in this result, where it is seen that the NIR LVF still extends to the short red-wavelengths while the VIS LVF still extends across its full visible light spectrum, as desired for later experimentation. In short, the UV curable epoxy is shown to work as an initial method of bonding different materials for integrable fabrication and devices. The CMOS image sensors are now subject to spatial filtering by means of the LVF, enabling a basic setup to establish methods for further integration perspectives.

To analyze these images, a methodology emerges where incident light filtered through the LVF can then be made subject to signal processing as its captured by the CMOS sensor array. The image exposure time can be made adjustable during any measurement, depending on the signal intensity, but while noting that an increase in exposure time also increases the number of photons collected that contribute to noise. Within the full pixel array, a region of interest is selected and trimmed along the gradient axis of one LVF on one CMOS image sensor, and is then averaged in intensity along the transverse direction of the LVF. Using the spatial-spectral conversion ratios as found before, a corresponding wavelength can be extracted from the pixels. Each set of sensing data collected on the CMOS is thus subject to a set of filtering constraints when resolving per pixel, as:

$$I_{t,pixel} = \sum_{\lambda} I_{0,\lambda} \cdot a_{\lambda} \cdot b \cdot c \cdot d \tag{3.5}$$

where $I_{0,\lambda}$ is the initial weighted intensity per wavelength as found by the integrated spectrometer, a_{λ} is the responsivity of silicon across the spectrum, b is the Gaussian fit parameter, c is the LVF-to-CMOS optical coupling, and d is the spatial-spectral conversion ratio for relating intensity overlap in wavelength to pixels. Whereas $b, c,$ and d can be assumed constant across the LVF spectrum for incident light, the responsivity must therefore be encoded into the processing algorithm to account for the silicon photodiodes [64]. The final transmitted intensity is the figure of merit when comparing the integrated LVF spectrometer approach to tabletop methods.

3.4 INITIAL TESTING AND METHODS

The merits of the system are therefore first tested to determine the strength and spectrum of the sensing seen, prior to full integration. This is used to both confirm the concept as well as to produce initial constraints related to the integrated optics and electrical drive circuitry next needed. Utilizing the first CMOS image sensor setup for rapid setup, a methodology is devised for direct comparison of results to a tabletop spectrometer and an OSA. In this, a bench-top design is created. To extract quantitative understanding on the integrated spectrometer's efficacy, a set of optical fluorescence and absorption tests is used.

3.4.1 Fluorescence Setup

The initial sensing setup for the fluorescence test turns on the fact that fluorescence is inherently a quantum mechanical process where an optical setup must be able to detect a *wavelength-shift* that is characteristic of a particular material. As shown in Figure 3.8a, a fluorescence test proceeds by applying an external photon source that is resonant with a particular molecular "line" (i.e. $|1\rangle \rightarrow |3\rangle$) and then allowing scattering mechanisms in the material to *Stokes shift* the energy and instead spontaneously emit a small-signal, *red-shifted* wavelength (i.e. $|2\rangle \rightarrow |1\rangle$) [50]. This material interrogation can thus be read out as a set of fluorescence peaks that are associated to a particular excitation source, so a particular chemical or material must be matched to an emitting source with enough intensity so that the spontaneous emission of the fluorescence is detectable.

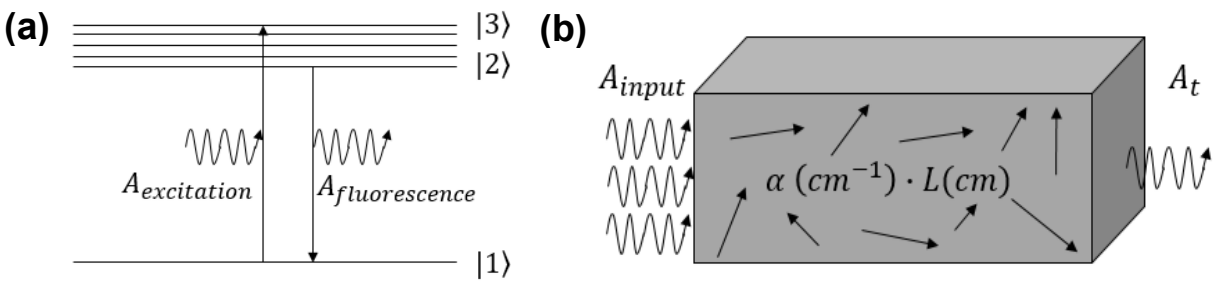

Figure 3.8 Diagram of optical fluorescence process in (a), where each line comes from a molecular transition, and diagram of optical absorption process in (b), where bulk attenuation reduces transmission.

As such, the excitation source for the fluorescence setup is chosen to be from a blue laser ($\lambda = 410$ nm) for the VIS LVF and an infrared laser (λ= 785 nm) for the NIR LVF. The excitation source is set up to be externally focused with a set of focusing optics into a liquid fluorphore test specimen and is then collected, and collimated to cover the full spectral range of the relevant LVF. Off-angle collection of the fluorescence is used as necessary to subdue the strong-field excitation source when it might saturate the LVF and thus hide the weak-field fluorescent signal.

3.4.2 Absorption Setup

The absorption setup is constructed separately to allow for larger interaction lengths. As shown in Figure 3.8b, the absorption process is predominantly classical where a loss term per bulk length affects an incident signal, I_0, and attenuates due to scattering mechanisms inherent to the material over a given length to overall transmit a fraction of the initial term. This produces an alteration in the amplitude of a particular source that is spectrally dependent, so a wide-band source is ideal for measurement of a particular chemical or material's absorptive signature [50]. Thus, a relation between a transmission measurement over a wide-band source and its corresponding absorption properties across the same band can be inferred.

Absorption tests are thus matched to a white light LED source, spanning a broadband spectrum of 400 nm $\leq \lambda \leq$ 800 nm , that is collimated through a bulk liquid material, expanded via free-space optics, and the remaining transmitted light is made incident on the LVF.

3.4.3 Test Layout

A set of two layouts for the two experiments on the first CMOS image sensor is therefore constructed on a tabletop. The schematic for each is shown in Figure 3.9a and Figure 3.9b. In this schematic, the effect of the LVF as part of an integrated spectrometer begins to come to light. The LVF will transmit through the relevant light spectra at only specific points.

The focusing optics for fluorescence contain a set of two biconvex lenses that are first placed apart by a focal length from the diverging source, collimated, and then again spaced by a separate focal length from the center of a fluorophore-containing cuvette. To test the fluorescence, a plano-convex lens again placed a focal length's distance is used to collimate the relevant fluorescent light at a 90° angle from the excitation direction, and this is then sent onto the sensing device. Critical to this verification of the LVF concept is the simultaneous collection in a separate spectrometer for comparison, as shown. A set of QD solutions is used to test the fluorescence, each designed to emit at a wavelength denoted by its name (QD520, QD560, QD610, QD740, QD880); as well, an IR fluorophore dye is prepared to confirm the operating range of the LVF spectrometer across its wavelength range. Synthesis of these QD solutions is either contained to its purchase or is produced in-house by the assistance of those associated with [65,66].

The absorption optics utilize a set of diverging spontaneously emitting white light sources that are collimated and transmitted through the absorptive test material housed inside a cuvette of 1 cm propagation length, followed by passage through a set of expanding optics containing a set of two biconvex lenses, each again placed as before to enable their desired effect on the optical signal. This light is therefore spread in order to cover the full gradient length

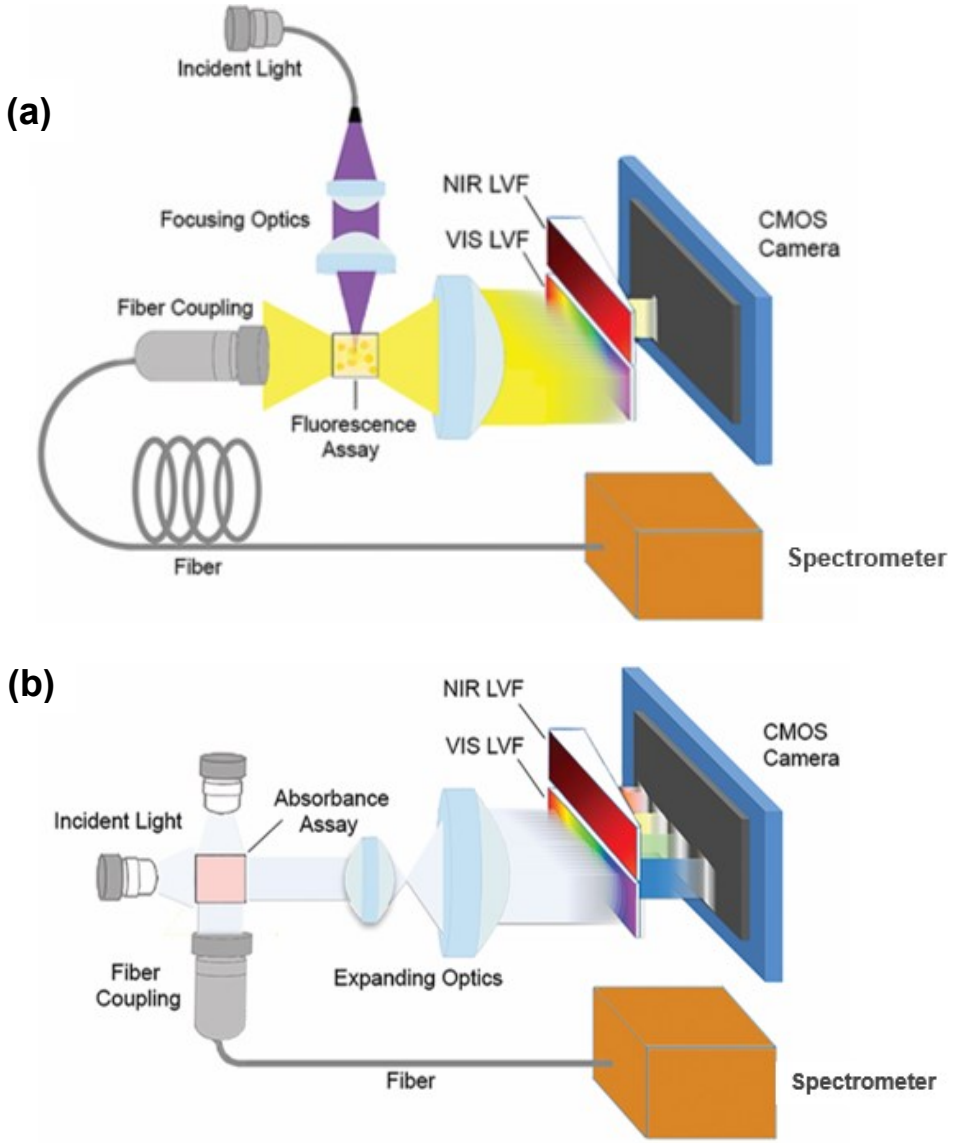

Figure 3.9 Layout diagram of initial fluorescent testing in (a), confirming ray optics design and that a wide range of sensing is possible on the LVF spectrometer. Layout diagram of initial absorption testing in (b), confirming colorimetric capabilities of integrated design.

of the VIS LVF, given its wide-spectrum attributes. The materials chosen for testing this effect are first a set of food coloring dyes to verify the absorptive characteristics of each dye, followed by a dilution sweep of a single green color dye to test the efficacy of the LVF in pulling out resolvable data at lower intensities, and then finally a colorimetric assay kit that detects the presence of free chlorine contaminants in tap water by the onset of a pink color.

The results from each fluorescence test are shown in the next set of figures. Figure 3.10a and 3.10b show the results of each QD solution as collected on the comparing handheld spectrometer and on the LVF spectrometer system in question. It is seen that a comparable set of results can be made with the LVF spectrometer using just the CMOS pixel value results, able to resolve well across the full spectrum in question [62]. And utilizing the conversion ratios

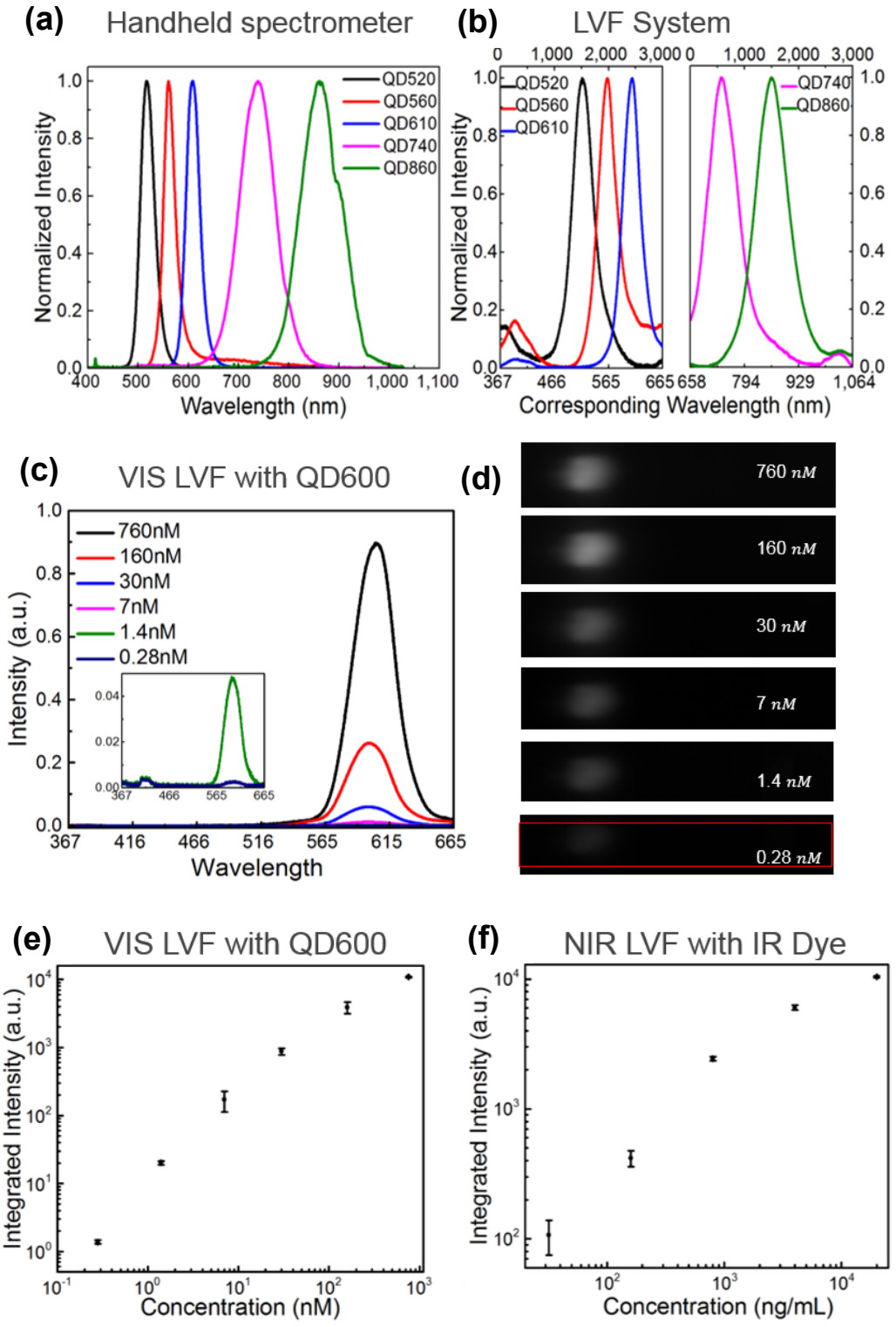

Figure 3.10 Fluorescence emission test for five different QD solutions on portable spectrometer in (a) and on LVF system in (b), confirming its detection range and comparability. Emission spectra on VIS LVF across QD concentrations in (c), with inset showing the lowest two. Cropped images from integrated system showing the same concentration range in (d). Spectral integration for each concentration on VIS LVF in (e) and on NIR LVF in (f), plotted with standard deviation whiskers.

for each LVF as found before in (3.1) and (3.2), a corresponding wavelength can be matched to the pixel count and as expected this matches the wavelengths of the collected fluorescence well to the handheld spectrometer results.

Following this, a set of concentration measurements for a QD600 solution and for the infrared fluorophore are prepared. The QD600 is readied at concentrations ranging from 760 nM to 0.28 nM, while the infrared dye is prepared from 20 µg/mL to 32 ng/mL. Figure 3.10c shows the results as an example from a measurement on the VIS LVF of the QD600 across its range along with the actual CMOS image sensor pictures (Figure 3.10d), where each profile of the dilution is normalized by its corresponding CMOS image sensor exposure time for proper comparison. Figure 3.10e and Figure 3.10f thus finally present the spectrally-integrated intensity of each of the concentration sweeps, confirming that a linear increase in the fluorescent signal sensed is found as well as confirming the efficacy of the LVF sensing at low concentrations. This monotonic increase can thus be extrapolated to predict the expected

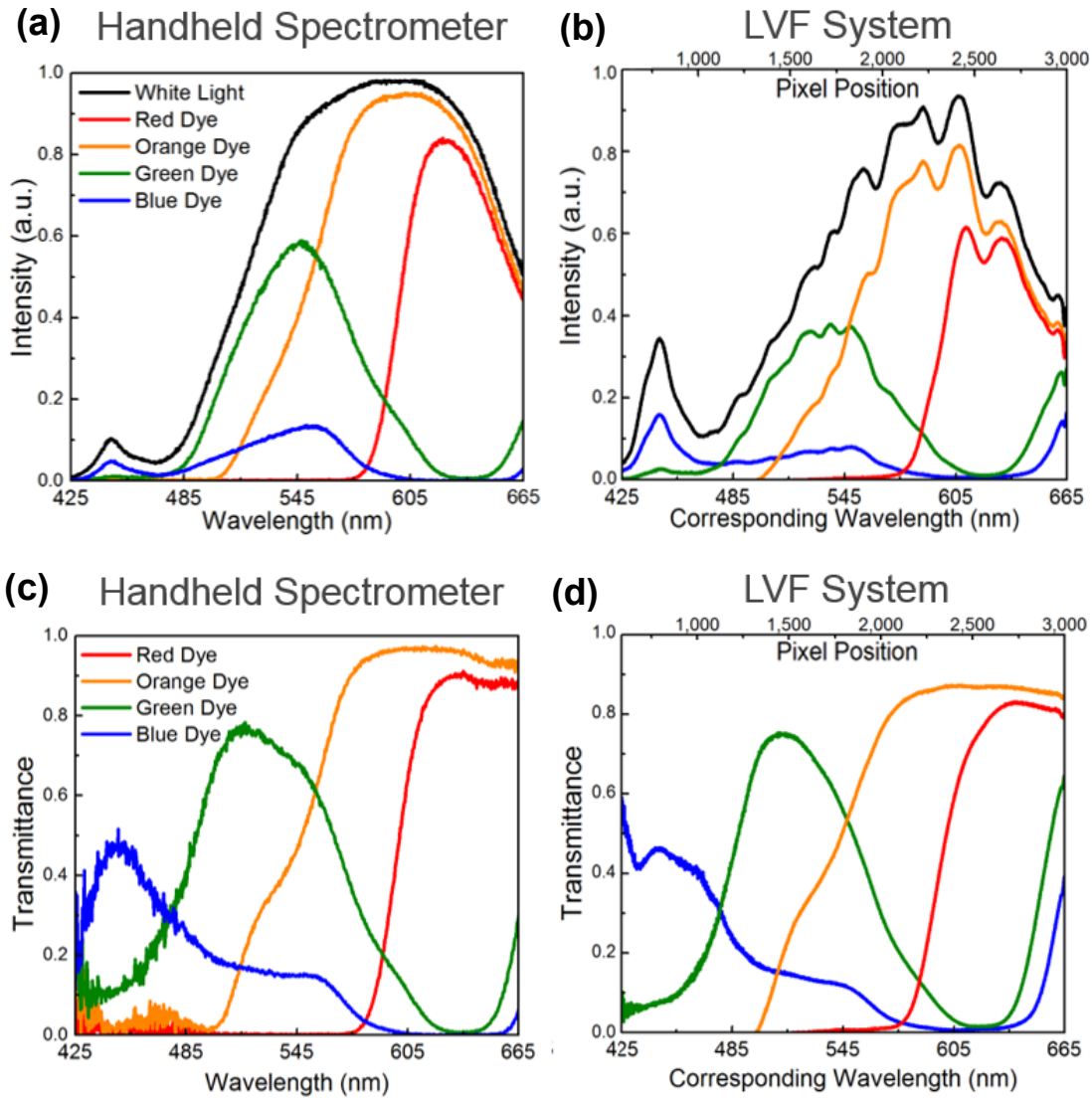

Figure 3.11 Absorption results across food dyes for the comparison handheld spectrometer in (a) and for the LVF system in (b). The reference is in black. Calculated transmittance for the comparison handheld spectrometer in (c) and for the LVF spectrometer system in (d).

intensity at higher concentrations of fluorescing chemical, as well as to predict the limits of detection at gradually lower concentrations. The results from each absorption test are next shown. In Figure 3.11a through Figure 3.11d, the set of results from the initial food coloring transmission tests are displayed, where it is seen that the implied absorptive properties (as interpreted from the transmission) of a particular dye vary across the spectrum. A series of fringe patterns is seen in the LVF spectrometer intensity results in Figure 3.11b, on account of the fact that these initial tests are using the CMOS image sensor with its cover-glass still attached [62]. Because of this, fringe patterns emerge from the incident white light source and any back reflections caused by the index change upon incidence with the silicon pixel lens array. However, this effect is overall not detrimental to the results, since this is common across the entire spectrum given the LVF's spatial-spectral relation, so once the transmission results of output is found (dividing a dye's intensity over the baseline white light intensity), the effect is removed, as shown in Figure 3.11d. Thus looking at the transmission results as derived from the intensity results, it is again found that the LVF system produces satisfactory

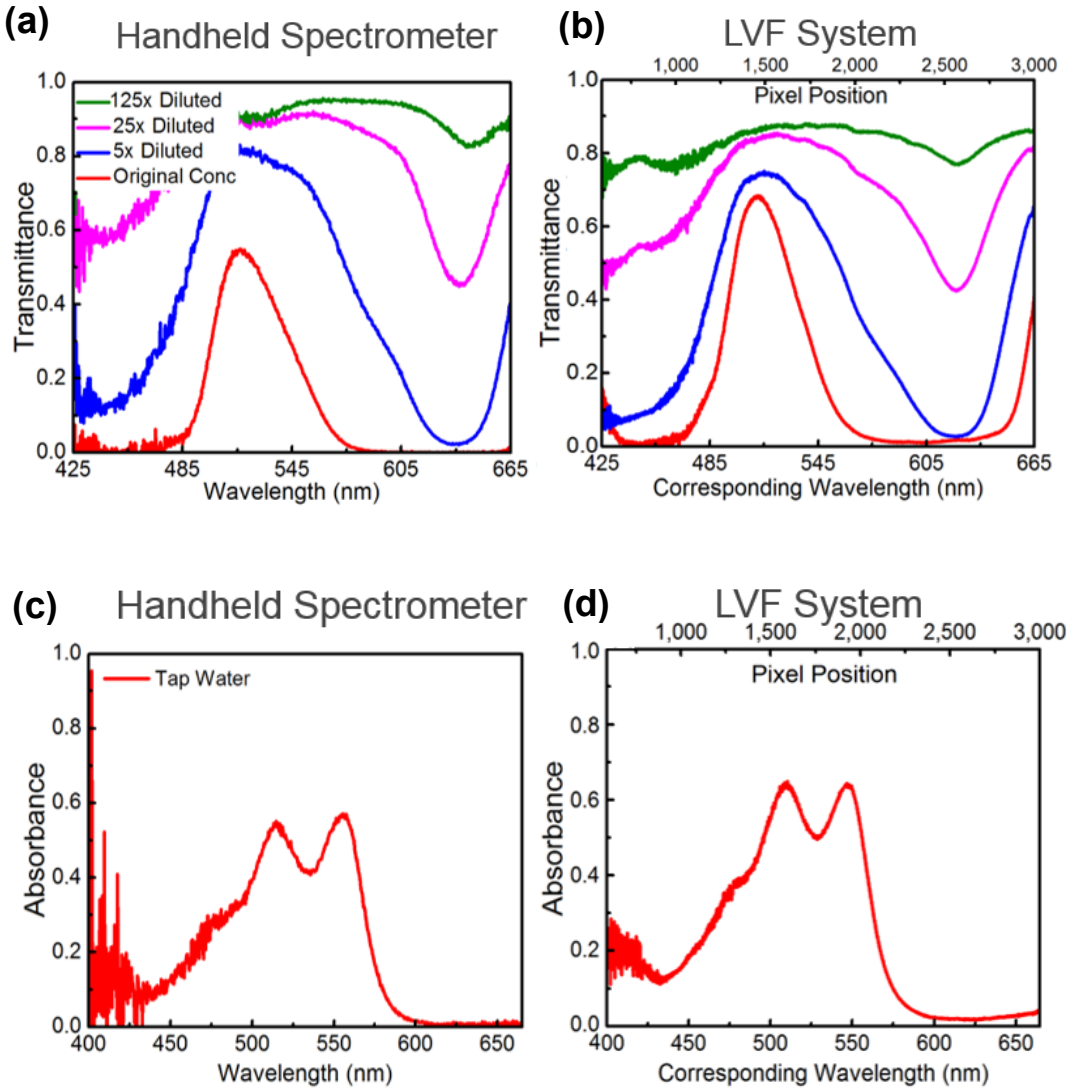

Figure 3.12 Transmittance results for dilution sweep of green dyes on comparison spectrometer in (a), and on LVF spectrometer system in (b). Absorbance of free chlorine in tap water seen on handheld spectrometer in (c) and on LVF spectrometer in (d), showing characteristic saddle.

results as compared to the handheld spectrometer. This is reassuring, as it underscores the fact that using the LVF setup produces an exceedingly compact version of the same spectroscopic effects, pointing the way forward for integration.

The next set of results looks at the concentration sweep and colorimetric effects. Shown in Figure 3.12a and Figure 3.12b, the results across a concentration sweep for green dye again show the same qualitative effects, confirming the LVF system's merits. Figure 3.12c and Figure 3.12d are the results found from the water quality test for detecting free chlorine, utilizing local city water (Urbana, Illinois). Again looking for the onset of a pink color whose intensity is directly proportional to the chlorine concentration, the results show the capability of the system to perform analytical measurements. The resulting absorbance of the free chlorine serves as the figure of merit, as calculated from the transmission results by methods covered in [67], using:

$$A = log_{10} \frac{I_o}{I_t} \tag{3.6}$$

so absorbance produces log results that are displayed on a linear plot. This shows that appreciable free chlorine is detected by the LVF system via the absorptive signature seen in the spectrum, in good agreement with the expected saddle as seen on the comparing instrument. Noting local water quality reports for the city of Urbana [68], the LVF is capable of detecting chlorine concentrations lower than 3.9 mg/L. This then proves the concept and readies it for integration.

3.5 INTEGRATED OPTICAL DESIGN

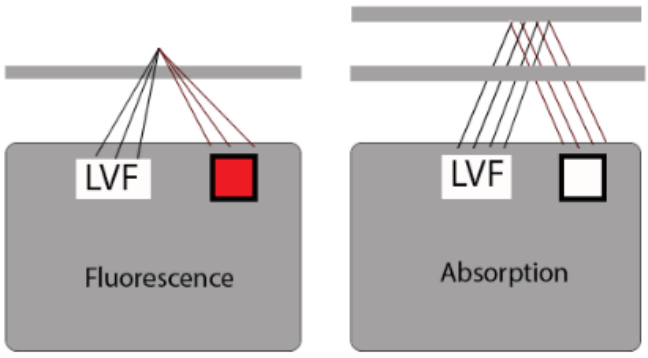

Figure 3.13 System-level diagram showing the intended optical path length for integrated mobile device.

To then begin inward focusing on the goal of heterogeneous electronic-photonic designs, a method for integrating together the LVF spectrometer with its necessary optical elements is created. The intent of the design is to make a photonic sensing device capable of attachment to a mobile smartphone platform while still centered around a CMOS image sensor. This allows for the first clear steps towards seeing an integrated system become scalable, bringing macro-scale elements down to the sub-millimeter level. As such, the overarching goal becomes finding a

way to match the results obtained above with a maximally condensed device footprint. This means that a set of ray optics-based approaches shall be used to prepare an optical schematic that couples light into a set of microfluidic assay containers and then collects the scattering or transmitting result onto the CMOS for spectral analysis. The overall design straddles the electronic and photonic domains by providing the necessary components to integrate electrical drive circuitry, optical components, the specimen under test (SUT), and the LVF-CMOS bonded system. A fluorescence optical design is therefore prepared that focuses light to a point specified at 9 mm above a CMOS image sensor plane (Figure 3.13), while an absorption optical design is prepared that collimates light into a microfluidic again placed 9 mm above a CMOS image sensor plane (Figure 3.13). Each miniaturization design has been completed by first modeling the ray optics routing necessary for a particular spectroscopy method. The software ZEMAX has been used to create each optical layout, while the software AutoDesk Inventor has been used to construct the assembly to maintain these integrated geometries. The ZEMAX software allows for the inclusion of index and geometry information for proper beam forming, while Inventor makes orthographic drawings for fabrication.

3.5.1 Fluorescence Integrated Design

A condensed optical layout is constructed using red light LEDs to operate as the fluorescence light source. These LEDs are chosen from the OSRAM miniTOP LED catalog, each having the dimensions of 1.4 mm (width) x 2.2 mm (length) x 1.3 mm (thickness) with a central wavelength of $\lambda = 630$ nm and a linewidth of $\Delta\lambda = 16$ nm. These dimensions and their corresponding light emission spectra are downloaded as a single packaged file from OSRAM and incorporated into the ZEMAX layout as a solid object denoting one LED.

To produce a steady stream of red light that can be focused into the cuvette, a set of three LEDs are chosen after early tests to produce a single "light bar" that can excite and fluorescence over a wider range in the microfluidic sample. A 3 mm diameter rod lens of length 10 mm and BK7 glass is downloaded and purchased from a standard optical inventory is inserted in the optical pathway of the red LEDs. The rod lens acts as a biconvex lens whose radius

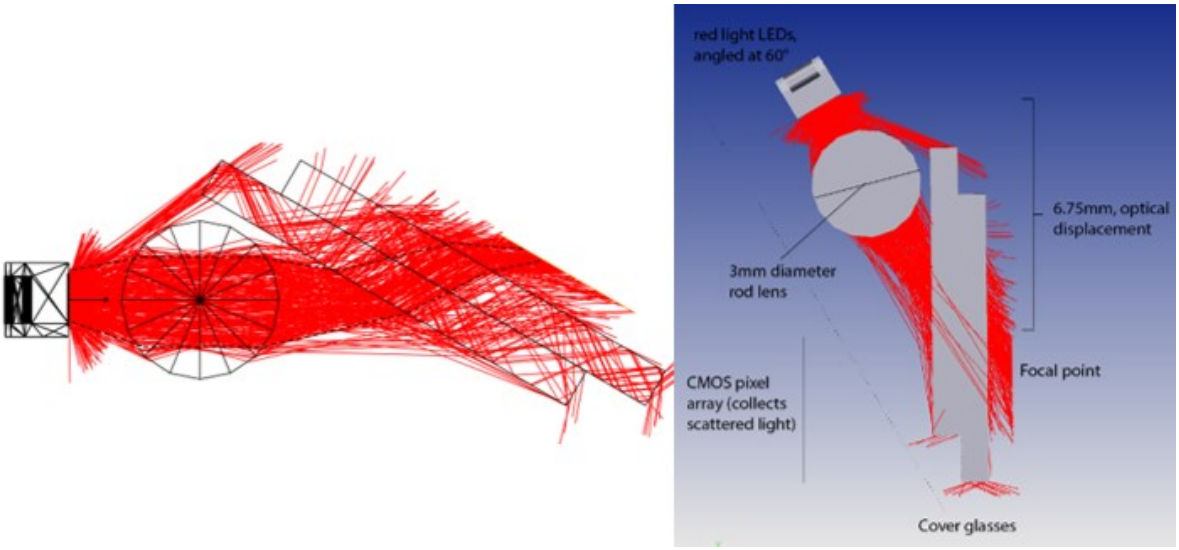

Figure 3.14 ZEMAX results showing the final optimized design of the fluorescence integrated photonic design. The image on the left shows the path caused by the rod lens, producing a focused beam that is designed for maximal intensity inside the cover glasses. The corresponding measurements are shown on the right.

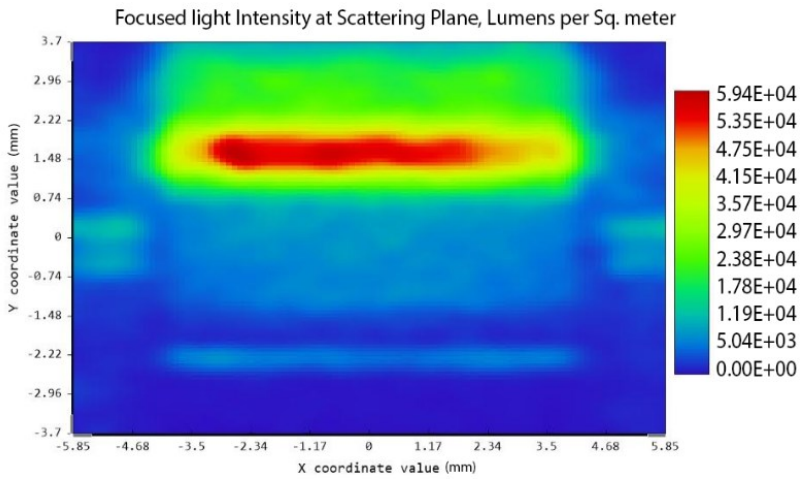

Figure 3.15 Intensity results from ZEMAX simulation, where a focused light "bar" is seen at the fluorophore.

of curvature is that of the radius of a complete circle, allowing for maximally compact focusing lengths. Initial studies in ZEMAX confirm that slight adjustments in the placement of the source relative to the lens greatly distort the ability to focus the light into a single bar, so an optimization process native to ZEMAX is run. In this optimization process, the location of the focused "image" is locked in place and the source-lens separation is varied. Through iterative runs, this finds that by placing the lens 2.5 mm away, the red LEDs are then focused past the rod lens and just into the surface of the sample. As such, the red light LEDs are placed at an optimized incidence angle of 60° normal to the plane of the CMOS image sensor, as this will allow scattering light off the sample solution to fall directly onto the CMOS pixel array while minimizing any source light scattering back. Two sets of cover glasses are placed in front of the optical path after the rod lens to account for the refractive bending of the light through a new material: one piece signifying the cover-glass on the back of a mobile phone, the second signifying the first wall of the microfluidic cuvette holding the fluorophore sample placed 9 mm from a CMOS image sensor plane for consistency. By then re-simulating the optics through the ZEMAX software, the ray path adjusts to each piece of silica glass in the path and the focal point is found just inside the cuvette. This setup therefore finds the point where fluorescence is to be expected, and as such is set to be right about the LVF for proper collimation. The results from this design are shown in Figure 3.14. It can be seen that the ray optics software emits rays from the red light sources and they land as focused at the focal point. The displacement between the source and the focal point is seen, as varied by the index shifts.

To confirm that focusing has been achieved into the cuvette, an intensity analysis just inside the cuvette plane is performed in ZEMAX. This is done by constructing a detection plane past the second cover glass, causing all emission rays to fall onto it, and then the upstream layout is optimized such that maximal focusing is seen in the cross-sectional power intensity. The optimized result that matches to the above setup is shown in Figure 3.15. These results show good beam uniformity and confirm that the three LED sources provides sufficient intensity at the focal point.

A metal framework is designed in Inventor so as to hold these optical components in place. Designed for fabrication in aluminum, an integrated assembly is produced that aligns the optics as according to their ZEMAX layout

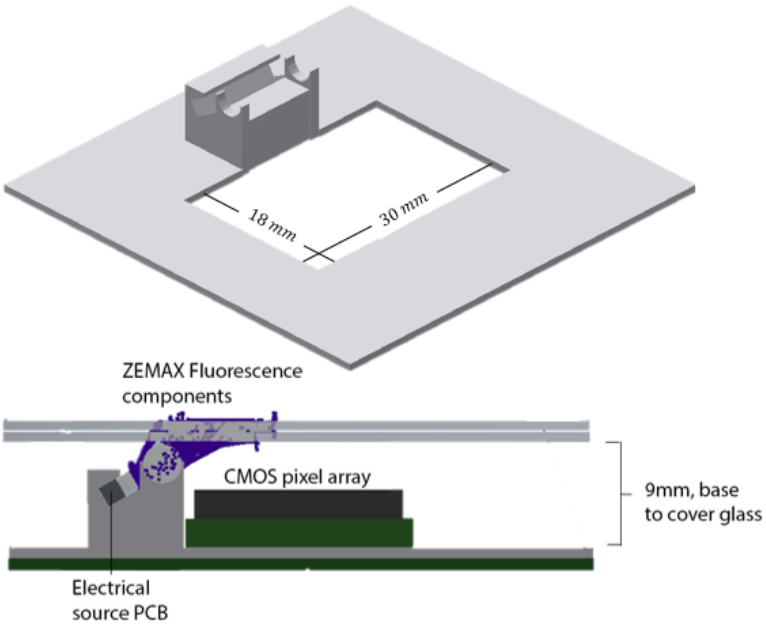

Figure 3.16 Design of integrated assembly piece for proper geometric alignment of fluorescence components.

with their relevant placement so all fluorescent light may traverse through the LVF as normal to the gradient axis. This assembly piece is designed to make room for an electronic PCB connection underneath the set of LEDs and their lenses, allowing for a full electronic-photonic consideration. This design is prepared with regards to its ability to be fabricated, its ability to securely hold together the photonic components, and its ability to be matched to a microfluidic and a CMOS image sensor for full consideration of scalability. This metal framework is shown in its final design as Figure 3.16.

3.5.2 Absorption Integrated Design

A set of white LEDs are implemented as the excitation source for the second optical design. Again using OSRAM brand miniTOP LEDs with the same dimensions as before, the spectra of each have a broadband spectrum of λ = 400 – 750 nm, ideal for use with the visible LVF.

The absorption optical layout is used to collimate white light directly into the cuvette sample, allowing light to travel into and be reflected in collimation back onto the LVF. Because of this optical path doubling, only a smaller microfluidic depth is needed. A 5 mm diameter rod lens with a length of 10 mm is chosen from Edmund Optics to serve as the beam collimating lens for the diverging white light. As before, a ZEMAX optimization simulation is commenced that places the lens 3.46 mm away from the white LED sources, within the focal point, so as to collimate the optical rays. Again, this works by the principles of biconvex lenses discussed in Chapter 2 and its ray matrices. The collimated light is transmitted through the cuvette and reflected off a mirrored surface inside the microfluidic, placed 4.5 mm inward, that then guides the transmitted light to the CMOS array. The cover-glass pieces are again included in the ZEMAX optics simulation for full refractive consideration. Through optimization, an angle of 32° normal to the cover glass plane is found to position the light sources. This reduces horizontal displacement along the optical setup for maximal integration. The results of this optimization process is shown in Figure 3.17.

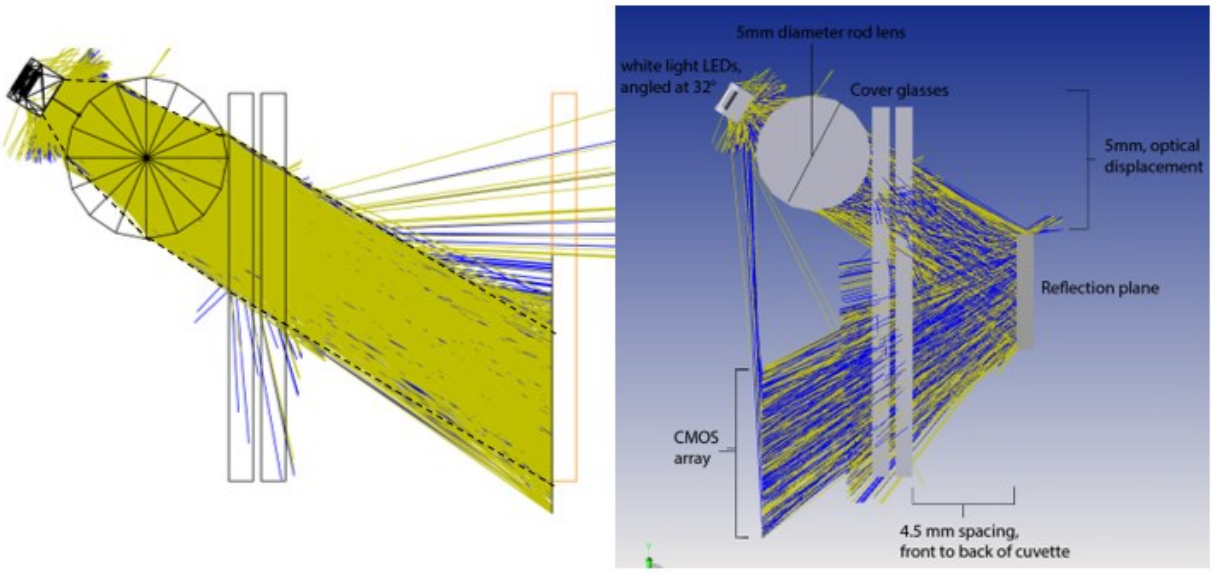

Figure 3.17 ZEMAX results for the absorption setup, where a separate rod lens is optimally placed along the optical axis to produce good confinement. It is seen on the left that the ray trace produces strong collimation beyond the lens. The image on the right shows the same with its reflection, denoting all measurements.

To then confirm that collimation is seen, a secondary optimization in ZEMAX is performed by means of looking at the intensity patterns. Constraining for divergence angles of 0° at the detection plan at the back of the cuvette on the reflection plane, collimation is found within the design. These intensity measurements are shown in Figure 3.18. A consistent intensity is seen across the spread of the lens, both across its diameter and along its length which latches with the length of the LVF. This then confirms that the setup of these optical components readies the full electronic-photonic device for sensing.

A separate aluminum framework is constructed for the absorption setup, as before for the fluorescence setup. This is used to assure that the spacing between the sources and emitters allows for collimation while the spacing between the microfluidic and the LVF allows for maximizing compactness, a requirement for good integration. The

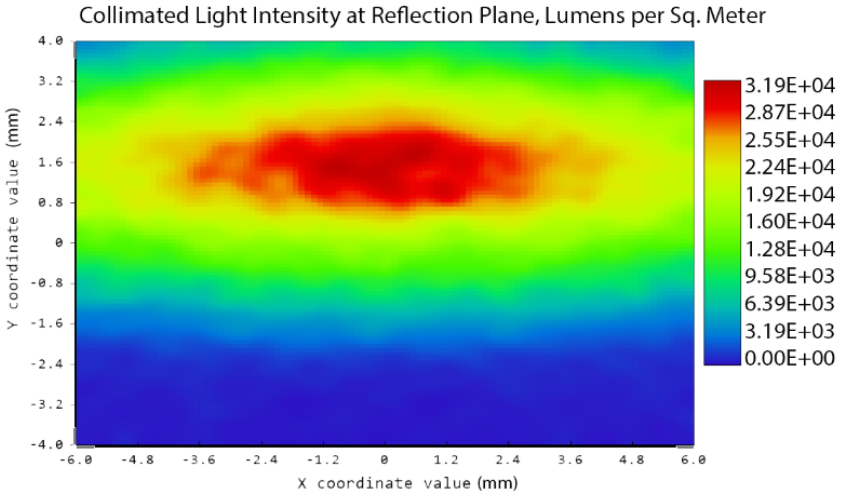

Figure 3.18 Intensity results from ZEMAX simulation, where collimated light is found past the glass plane.

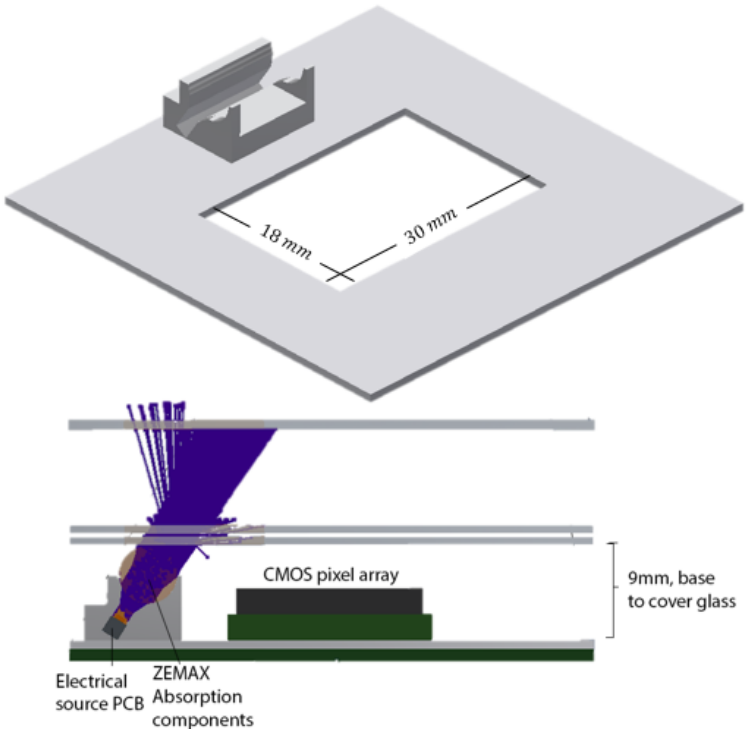

Figure 3.19 Design of integrated assembly piece for proper geometric alignment of absorption components.

same placement of the electronic PCB is employed here. This is shown in Figure 3.19, showing the finalized design as prepared and optimized for fabrication.

3.6 INTEGRATION TESTING

The integration designs are then analyzed, combined, and finally put to testing for confirmation of their ability to act as a scalable and heterogeneous means of distributing electronic-photonic sensing devices. The set of tests again uses both absorption and fluorescence. If proven successful, this can be used as a justification that the goals of electronic-photonic integrated circuitry can begin with establishing methods to place together optical components atop CMOS-based electronics and produce valuable sensing results.

To test this system, a cradle is designed to hold each assembly together for quick access and testing. This platform is designed in Inventor as well. A matching set of microfluidics is designed to fit into this cradle, where the exact placement of each testing assay is based off the original ZEMAX and Inventor integrated designs, given that the optical path length is sensitive to the location of the fluorescent or reflecting surface. A variety of microfluidics are tested and optimized, accounting for the specific assay it is designed for as well as accounting for slight imperfections in the stereolithographic prints of the pieces. The metal framework is fabricated and filed to proper form to account for any variation in the component fit. Each optical component is then fastened into the setup and bonded into place using UV-curable epoxy. An electrical PCB is designed using the software Eagle so that the LEDs are connected in

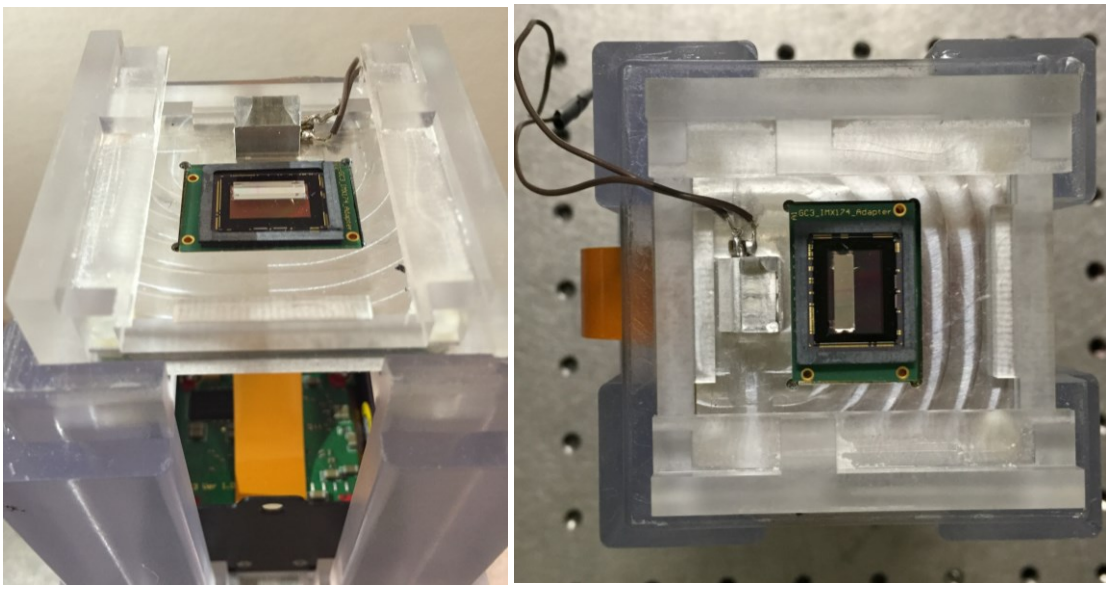

Figure 3.20 Setup of integrated assembly stand for testing. The LVF bonded onto the CMOS image sensor is clearly seen, along with the integrated electronic and photonic elements arranged by it.

parallel so that a current source may be used to drive them with common bias. An imaging software native to the electronic that drives the CMOS image sensor is used for bitmap-based image capture, able to be processed and trimmed after detection of absorption or fluorescence experiments. The final setup, shown for absorption, is presented in Figure 3.20 where the electrical wiring is shown going to the optical sources, the LVF is shown bonded onto the CMOS image sensor, and the optical components are configured as necessary to project light into the sample under test.

The system is first tested for absorption results on the VIS LVF in the integrated design. The results confirm that an integrated electronic-photonic device can be made out of the heterogeneous bonding of optical components onto an electrical framework and an LVF onto a CMOS image sensor. Figure 3.21a through Figure 3.21c show an initial set of tests comparing the resolution of the integrated LVF spectrometer to the same spectrometer as before. Four separate laser sources—at λ = 410, 413, 548, and 669 nm—and a wide-band white light source filtered by either a band-pass or high-pass filter are used for comparison. It is seen in these that the spectra from each peak or band is well-aligned with the comparison tool, confirming an overall efficacy in the integrated system as well as producing a conversion ratio for the VIS LVF of:

$$CR_{VIS} = 5.714\ \frac{\text{pixel}}{\text{nm}} \tag{3.7}$$

Figure 3.21d,e show the absorption results for an ELISA absorption kit used as described in [69], where a fetal fibronectin assay is arranged in different concentrations to determine the minimum resolvable signal for the integrated setup. In this, a broadband light source is used and the spectra is seen to show an increase in absorbance with increased concentration, ranging from $4 - 1000$ ng/mL. This measured absorbance spectra presents the figure of merit for

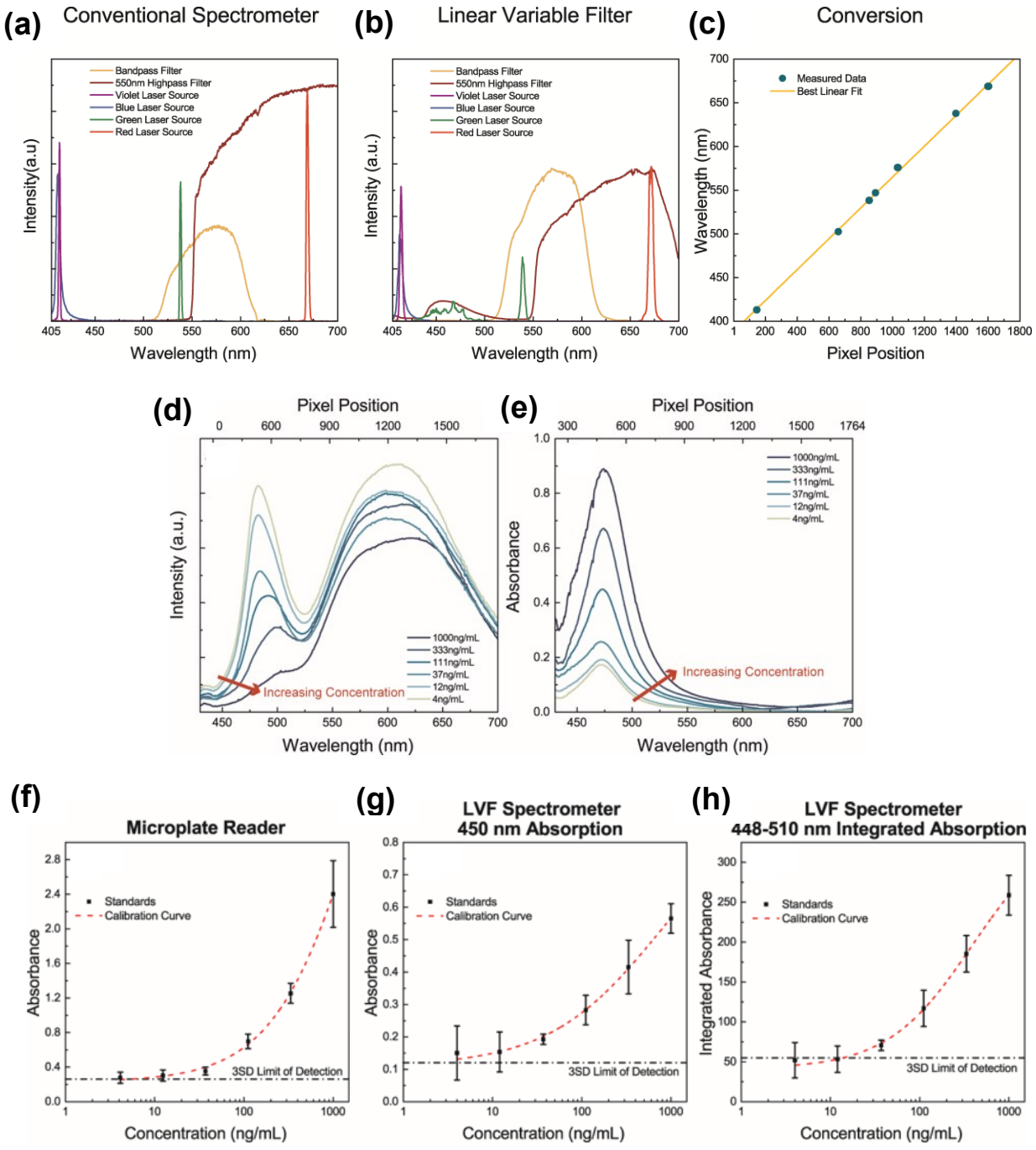

Figure 3.21 Spectra of comparison handheld spectrometer in (a), of integrated VIS LVF spectrometer system in (b), and a plot of the conversion ratio between the spectra in (c), using a linear fit model. Resultant spectra of serially diluted ELISA samples on the VIS LVF spectrometer in (d) and its corresponding absorbance of the same dilution sweep in (e). Dose-response absorbance across concentrations of ELSIA assay using comparison microplate reader in (f) and across the same ELISA assay using LVF spectrometer in (g), measured at absorption wavelength λ=450 nm. Total dose-response absorbance integrated over the λ=448 – 510 nm band shown in (g).

comparing this electronic-photonic device to other systems. To then see this comparison, a dose-response curve is presented for the same results from a microplate reader (Figure 3.21f), the LVF spectrometer at the $450\ nm$ point (Figure 3.21g), and a spectral integration dose-response from $448 - 510\ nm$ on the same (Figure 3.21h). These show good relation across the range of concentrations between the large microplate reader and the integrated sensing device.

Preliminary fluorescent results as measured on the integrated design are then presented in Figure 3.22. For this setup, a set of samples of the ALEXA750 fluorophore designed for emission at λ = 750 nm is prepared across a concentration range from $0.2 - 12.4$ µg/mL and utilized with the NIR LVF. To aid in the detection of the small-signal fluorescence, a low-pass filter is applied to block the excitation source light, allowing for a larger exposure time to detect the low concentration fluorescence. This shows that the integrated system is able to detect down to 0.8 µg/mL in its integrated setup form. Further testing is underway to determine the efficacy of the integrated sensing system for use in fluorescence, but the initial results show promise in the sensing system's ability to resolve small-signal effects.

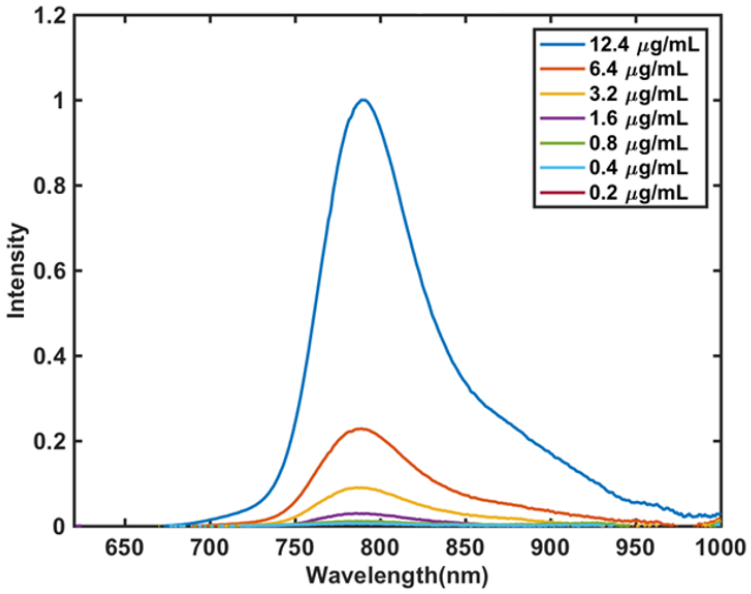

Figure 3.22 Plot of NIR LVF spectrometer system detecting fluorescence from an ALEXA750 sample.

3.7 DISCUSSION

The goal of integrating together an electronic-photonic circuit capable of signal sensing for biochemical analyses is therefore viable. It is made apparent that by reducing down a spectrometer path length to the size of an LVF, a system becomes integrable to a CMOS network, namely by bonding directly onto a CMOS image sensor capable of image processing. Then, by utilizing miniaturized optical components and aligning their output with a microfluidic, an entire biochemical analysis system can be made scalable for all mobile electronic devices, including smartphones. Key to these findings is the background work used to understand physically how the LVF works, to lay out schematics of optical components with ray optics software and CAD design software, to produce a schematic of electrical components that tethers the optical, to use macro- and nano-fabrication techniques for producing machinable

parts, to test the system as a heterogeneous setup, and to control the system electronically by means of a CMOS image sensor. These findings establish a set of methods for device integration where electronic and photonic domains can be made to interact with one another and produce sensing abilities for real-world applications. Given that the initial constraint to rapid adoption of point-of-use systems rested on the fact that these sensing systems are yet integrable or versatile, the LVF approach is promising in taking optical sensing to a small-scale. It can be reasonably expected that device designs in the area of biochemical detection and sensing will require continued integration as the available space for their components condenses just as the need for them becomes more apparent. For this purpose, the methods from this work can be considered. The guidelines for what will be required of these systems must at least include an excitation element and a spectral separation element, implying that the effects of light will be formulated from the ray optics to the spectral level. The approach outlined satisfactorily achieves this. To then combine these active and passive optical components with an electronic infrastructure serves the broader purpose of matching a novel system with an established network. This work accomplishes just that and provides a path forward in producing electronic-photonic circuitry capable of sensing and detection relevant to real-world biochemical usage.

CHAPTER 4: CAVITY TUNING DESIGN AND RESULTS

"The lamp of the future may be a speck of metal the size of a pencil-point which will be practically indestructible, will never burn out, and will convert at least ten times as much current into light as does today's bulb."
-Nick Holonyak, 1963

4.1 MOTIVATION

The expansion of telecommunication systems into the photonic domain for signal transmission has created a desire for stable and versatile laser designs. These designs are envisioned to straddle the needs of various long-haul and enterprise optical network applications in controllability and reconfigurability, where the ability to both route and control an optical signal can be made by means of coordinated photonic devices. The current approach to uniting such a system is by the use of a diverse set of components for active emitters, electronic drive circuitry, and modulators each attached to a laser cavity with a separate set of performance parameters. Yet this complexity poses limits on the ability to scale the overall design [43]. A rapid increase in the size and number of these devices, as well as a larger energy budget (J/bit) to run the system, places a hindrance on continuing this approach when inevitably denser signal propagation requires increased design complexities [49,70]. Instead, a method for heterogeneous electronic-photonic integrated laser designs is proposed that answers to this need. This would utilize available materials to propose a novel set of laser cavity designs that truly enable dense signal controls crossed between electronic and photonic domains, able to meet the needs of a diversified range of photonic applications.

Such an integrated electronic-photonic device aimed to control telecom data streams can reliably use the method of wavelength-tuning and fast switching to produce scalable network effects. Controlling the output wavelength of a particular laser by dynamic cavity tuning allows for dense wavelength-division multiplexing (DWDM), as shown in Figure 4.1, where a series of wave packets denoted by separate wavelengths from a single laser can be sent along in a single waveguide such that the overall information flow can be more densely carried as well as potentially routable on the basis of wavelength [71]. This would allow for a single network to more efficiently transmit signals with increasingly dynamic controls, enabling faster and steadier network connections that benefit the industry at large. To then realize scalability, these integrated devices must match well to present CMOS electronic designs while still harnessing the benefits of the optical domain for signal propagation, so a large set of constraints necessarily emerges.

Present structures designed for telecom-wavelength tuning are constructed in monolithic designs that present unique barriers to scale. Early work to integrate distributed feedback structures (DFB), as discussed further, based on InP gratings with InGaAsP telecom gain chips produced wide-band tuning yet with exceptionally large thermal variation in the tuning effect [72]. This was due to the amplified red-shifting in refractive index and thus its corresponding free spectral range as (2.74), making for impractical tuning controls. Current state-of-the-art designs in

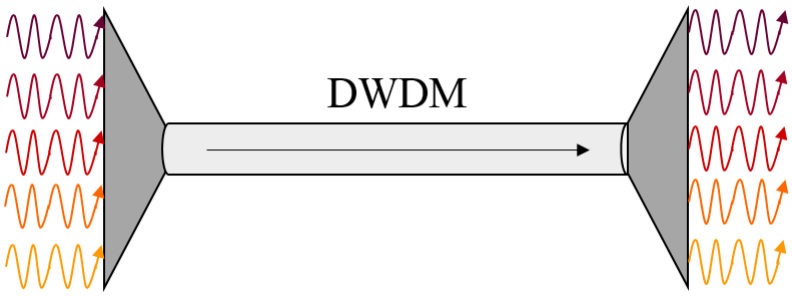

Figure 4.1 DWDM network, where multiplexing and demultiplexing sends multiple signals at once.

InP-based monolithic patterns use carrier injection modulation (blue-shift) to alter the refractive index, maintaining as many as 32 channels in the C-band spaced 100 GHz apart, and reaching switching speeds of 12 ns with higher tuning currents for each at 80 mA [73]. Yet a current-induced effect produces suboptimal tuning as the intended blue-shift in wavelength is countered by a thermal red-shift over time, in conjunction with large power losses at roughly 20 μW/GHz of optical signal power due to carrier-phonon interaction [74]. Separately, the present push for CMOS-compatible photonic integration has investigated silicon instead as a possible tunable material (i.e. silicon photonics). Yet silicon's centrosymmetry sustains only negligible nonlinear optical coefficients in its lattice, so silicon requires lossy methods of thermal-optic tuning with large transient switching delays through the use of thermal tuning [75]. This tuning, caused by large footprint resistive heaters along silicon cavities, produces very large refractive index changes and thus big jumps in longitudinal modes, yet the current required (100 mA) surpasses typical laser current thresholds, and the signal transience allows switching speeds now only just reaching 20 μs [76] with most systems still maxing out in the millisecond range. A popular material known for its large anisotropies, lithium niobate ($LiNbO_3$), has also been considered for large-scale cavity tuning structures yet is severely limited in the overarching goal of scalable heterogeneous integration due to the difficulties in fabricating sub-micron features or waveguides out of the material [77]. This in total points to the constraints in the current methodology in terms of approaching DWDM. In order to enable sophisticated wavelength-based packet controls, capable of wide-band tuning, a more versatile alternative material suitable for heterogeneous integration is needed.

4.2 GALLIUM NITRIDE ANISOTROPIES

Early work shows the material gallium nitride (GaN) and its III-N alloys offer numerous advantages when incorporated as a cavity optoelectronic. GaN contains unique material properties that prove suitable for the application of wavelength tuning design. The benefits of using GaN for constructing a tunable cavity come from the fact that GaN is an established material that has a wide bandgap (3.4 eV), whereas standard telecom wavelengths are at λ = 1310 nm, 1550 nm and this produces the energy-wavelength relation as:

$$E(eV) = \frac{1.24}{\lambda(\mu m)} \tag{4.1}$$

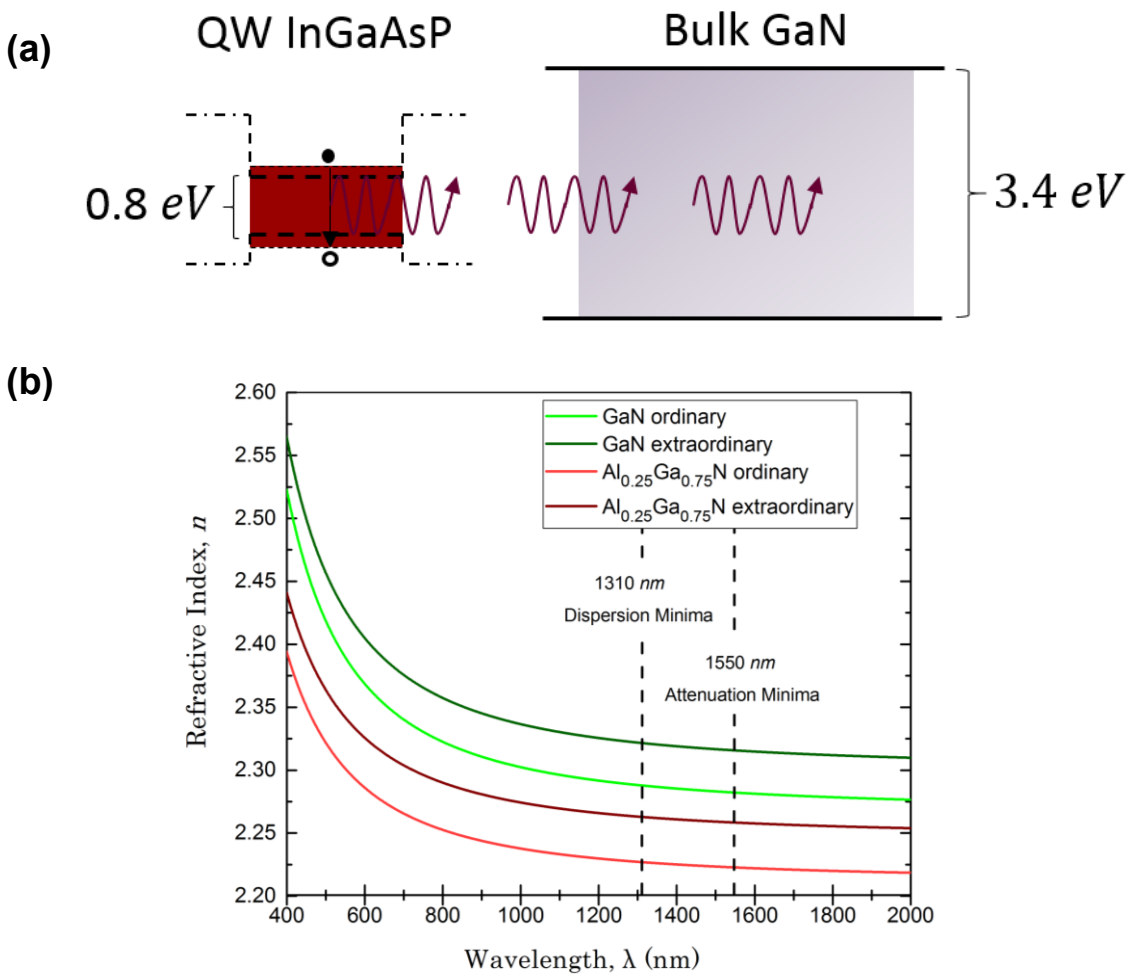

Figure 4.2 Bandgap diagrams of a telecom InGaAsP QW and its photon energy compared to bulk GaN in (a). Dispersion plot (Index vs. Wavelength) for GaN and an AlGaN alloy across axes in (b).

which correlates with photon energies of 0.8 eV and 0.95 eV for telecom photons, assuring high transparency in the 350 nm to 13.5 μm band [78], as shown in Figure 4.2a where a telecom photon will not be absorbed in GaN. Additionally, Figure 4.2b shows that GaN has low index dispersion across telecom wavelengths and has a higher index than its Al-alloys to enable optical confinement [79]. GaN also brings with it scalable fabrication techniques for production. This standing as an exceptional material comes from extensive research into III-N alloys for the use of active photonic devices, ranging from initial MOCVD-based low-defect GaN layers [39, 80], the inclusion of AlN-alloy nucleation and buffer layers [80], and various findings in dopant donor and acceptor materials [81,82]. III-N growth has thus seen wide implementation in blue-green laser diodes and white light LEDs [83,84], yet its use in other optoelectronic applications remains novel.

4.3 INTEGRATED CAVITY DESIGNS

The wide extent possible for GaN's use as an optoelectronic stems from its strong characteristics when grown as a wurtzite crystal. As described in Chapter 2, this presents an opportunity to make GaN and its alloys suitable for

the application of wide-band tuning. The nature of a wurtzite-grown GaN crystal means it has noncentrosymmetry, thus allowing for nonlinear optics effects. In particular, GaN has high *electro-optic, piezoelectric stress,* large nonlinear electric susceptibilities, and a large thermal conductivity [48, 79]. These anisotropies enable GaN structures to produce electrically-driven optical effects by straining and contorting the material on an angstrom-level, thus producing Coulombic variations to the refractive index [48]. Given this, the nature of GaN again suggests a highly effective solution to the question of efficient tuning. Electro-optic parameters in wurtzite GaN allow an applied electric field along the *c*-axis to align the atomic lattice of GaN as derived from electrical susceptibility and the Pockel's effect, causing changes in permittivity and thus the index [55]. The piezoelectric parameters in wurtzite GaN allow for a photo-elastic strain on the crystal that can induce appreciable fluctuations in the atomic lattice and thus controllable index changes when an applied electromechanical displacement is used, suggesting another practical method for cavity tuning in large-scale industry use [55]. Together, these benefits in GaN motivate a path forward in testing and implementing an integrated design for direct application to C-band telecommunications tuning (i.e. 1530 – 1565 nm). The goal is that GaN-based wavelength tuning can enable reduced footprints of optical sources, where an electrically-controlled GaN system can be used reconfigurably across wide wavelength bands and thus made compact enough onto existing CMOS electronic platforms for electronic-photonic integration.

This work presents the findings in two GaN-based edge emitting laser cavity designs matched to a telecom InGaAsP gain structure. The first set of designs is for a tunable laser that uses etched gratings in GaN along with a set of defined electrodes to produce an electro-optic effect for refractive index tuning of an internal cavity. This effect is described in conjunction with the *Vernier effect* by designing the system with a set of two cavity arms that can be biased separately for even wider-band longitudinal *mode-hopping* to extend the range of tuning (Figure 4.3a). The second set of designs is for a GaN-based tunable laser that produces a *standing acoustic wave* (SAW) atop a single

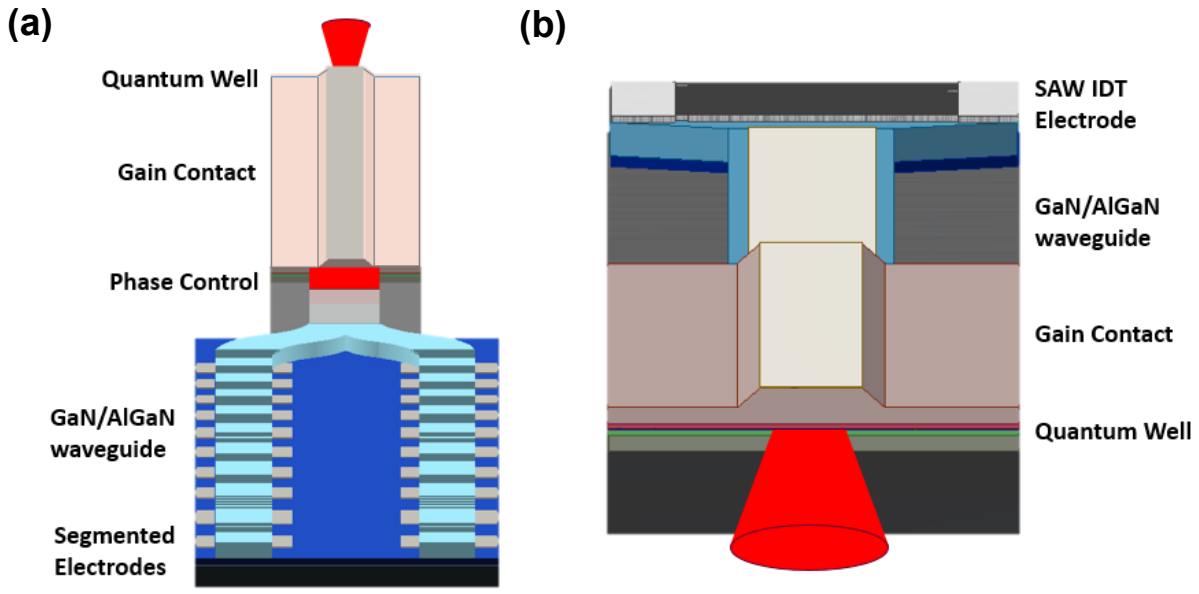

Figure 4.3 Design of etched sampled gratings tunable laser shown in (a), where the GaN (foreground) couples to an InGaAsP gain region (background). Design of RF SAW tunable laser shown in (b), where an IDT on GaN (background) emits from the QW

GaN length to produce a sinusoidal effective index pattern in the cavity that can induce piezoelectric and electro-optic effects for tuning (Figure 4.3b). This design is simulated in full to see the effects of uniting acoustic waves, RF electrical waves, strain, and photonic modes within the material GaN for a single electronic-photonic integrated form. Together, these designs are considered as part of the goal of enabling scalable DWDM devices that are CMOS compatible, so each system establishes a method toward utilizing a GaN-on-Si epitaxial design.

4.4 REFRACTIVE INDEX VARIATION

The use of GaN inside a telecom laser enables refractive index variation in the cavity by use of electronic-photonic interactions. A change in the refractive index, Δn, can be incurred by the fact that a set of perturbative effects on a material change its electrical permittivity, as shown by the relation [85]:

$$\Delta\left(\frac{1}{\varepsilon_r}\right) = r \cdot E + p \cdot S \tag{4.2}$$

where E denotes an electric field, S is for a unitless lattice strain, r is for the first-order electro-optic (Pockel's) effect (pm/V), and p is for the photoelastic parameter. Relating permittivity to a material's index as in (2.6), this produces the following relation for the change in refractive index:

$$\Delta n = -\frac{1}{2} n^3 \left(\sum_{i,j} r_{ij} \cdot E_j + p_{ij} \cdot S_{ij} \right) \tag{4.3}$$

This says that a series of perturbative effects is found across any material based on the vector components of any applied field or strain. An electric field effect is denoted by its three cardinal directions and a strain is denoted by the planarity of its effect's cross-section [85]. The effect in all directions is considered in summation, allowing for constructive interference to the index change in anisotropic materials and a largely canceling destructive interference in isotropic materials. These parameters exist in a material tensor described by the GaN 6mm (wurtzite) symmetry, so the non-zero elements must line up with the correct crystalline axes of GaN. Typical values of these parameters in wurtzite GaN have been gathered from prior research [86,87], showing:

$$\begin{bmatrix} r_{11} & r_{21} & r_{31} \\ r_{12} & r_{22} & r_{32} \\ r_{13} & r_{23} & r_{33} \\ r_{14} & r_{24} & r_{34} \\ r_{15} & r_{25} & r_{35} \\ r_{16} & r_{26} & r_{36} \end{bmatrix} = \begin{bmatrix} 0 & 0 & 1 \\ 0 & 0 & 0 \\ 0 & 0 & 1.96 \\ 0 & 0 & 0 \\ 0 & 0 & 0 \\ 0 & 0 & 0 \end{bmatrix} \cdot 10^{-12} \, \frac{m}{V} \tag{4.4}$$

$$\begin{bmatrix} p_{11} & p_{21} & p_{31} & p_{41} & p_{51} & p_{61} \\ p_{12} & p_{22} & p_{32} & p_{42} & p_{52} & p_{62} \\ p_{13} & p_{23} & p_{33} & p_{43} & p_{53} & p_{63} \\ p_{14} & p_{24} & p_{34} & p_{44} & p_{54} & p_{64} \\ p_{15} & p_{25} & p_{35} & p_{45} & p_{55} & p_{65} \\ p_{16} & p_{26} & p_{36} & p_{46} & p_{56} & p_{66} \end{bmatrix} = \begin{bmatrix} -8.6 & -2.3 & -1.7 & 0 & 0 & 0 \\ +2.3 & +8.6 & -1.7 & 0 & 0 & 0 \\ -1.7 & -1.7 & -9.1 & 0 & 0 & 0 \\ 0 & 0 & 0 & -2.7 & 0 & 0 \\ 0 & 0 & 0 & 0 & -2.7 & 0 \\ 0 & 0 & 0 & 0 & 0 & -3.2 \end{bmatrix} \cdot 10^{-2} \tag{4.5}$$

It is noted that these values are on the same order of magnitude as $LiNbO_3$ while considerably larger than various other semiconductors, including Si, InP, and GaAs [55]. The piezoelectric and Pockel's terms will apply solely to the integrated SAW-tunable laser design, while the Pockel's terms alone will be used for the grating design.

4.5 AlGaN/GaN INTERFACE

To produce an effective GaN structure inside an integrated laser cavity design, considerations must be made for the growth of GaN and its requirement for a buffer layer of an $Al_xGa_{1-x}N$ alloy. A proper structure for the proposed optoelectronic usage of GaN requires an undoped material with low defect and threading dislocation density, since any defect or dopant would cause unwanted optical signal scattering and possible exciton formation. Growing GaN atop an $Al_xGa_{1-x}N$ alloy as a buffer largely reduces these threading and defect sites [80]. However, given the anisotropy of all III-N lattices, a series of charge accumulation effects emerge at the material interface that must be accounted for to prevent optical attenuating effects, as shown in Figure 4.4.

This arises for GaN and its $Al_xGa_{1-x}N$ alloys because pseudomorphic growths along the c-plane (0001) experience both a spontaneous and piezoelectric polarization effect, P, that builds up charge concentrations, ρ, at their material interface by the Gaussian electrostatics relation $-\nabla \cdot P = \rho$ [88]. This means that the alloying chosen in any GaN/$Al_xGa_{1-x}N$ interface must be engineered accordingly. By this, an intrinsic stress is created in a c-plane GaN crystal that gives rise to a polarization:

$$P = P_{sp} + \frac{a - a_0}{a_0}\left(e_{31} - e_{33}\frac{C_{13}}{C_{33}}\right) = P_{sp} + P_{pz} \tag{4.6}$$

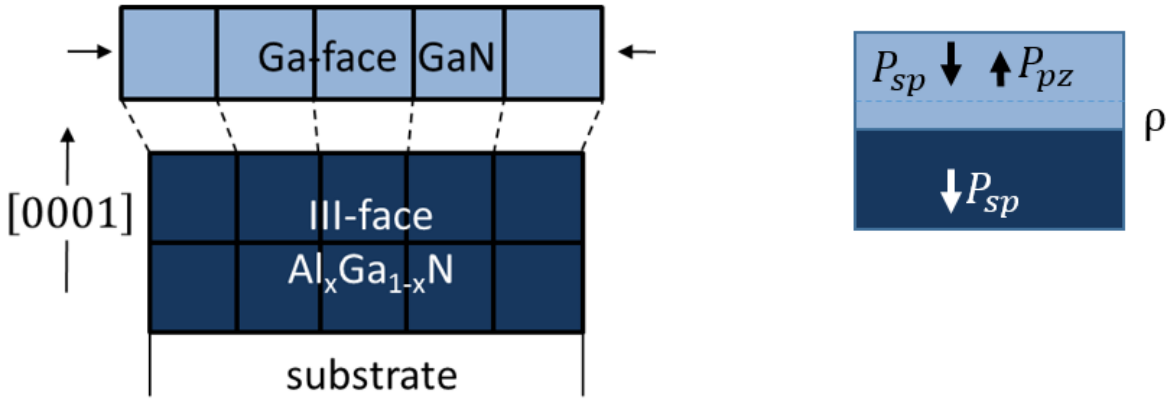

Figure 4.4 III-N interfaces where a built-in charge sheet emerges from c-axis growths. The pooling of carriers is shown on the right as a charge density, summed up from the piezo and spontaneous polarization terms.

where the spontaneous polarization goes as $P_{sp} = -0.052x - 0.029\ C/m^2$ for an alloy molar ratio, x, in $Al_xGa_{1-x}N$ [88], e_{ij} are piezo constants in determining GaN layer stress, and C_{ij} are the coupling constants that relate a Coulombic displacement to a stress. This shows that a chosen molar ratio of an $Al_xGa_{1-x}N$ buffer layer can produce an intrinsic spontaneous polarization that cancels with an intrinsic piezoelectric polarization, as shown in Figure 4.4. As such, alloys are chosen in this work for the buffer layer to have sufficient aluminum percentage to provide a maximal canceling effect in the charge sheet present at the interface. An $Al_xGa_{1-x}N$ alloy above $x = 0.25$ is found to be sufficient for a buffer layer that diffuses the charge sheet, by [89].

4.6 ETCHED GRATINGS DESIGN

4.6.1 Coupled Mode Theory

To utilize this ability to vary the refractive index in GaN, an applied form of coupled mode theory by use of Bragg etched gratings is first considered. A heterogeneous design is investigated that connects an active InGaAsP region producing gain directly to a bulk Ga-face GaN slab that is constructed atop an $Al_{0.5}Ga_{0.5}N$ buffer layer, as seen in Figure 4.3. The GaN slab is structured as a *Y-branch* waveguide that is physically etched to produce etched Bragg gratings on top. To assure scalability, this design is structured to be grown on silicon as the base substrate, enabling CMOS electronic compatibility as shown in Figure 4.5. It can be seen that this integrated design thus allows cavity light to propagate in z past the gratings in $x$continuously. The grating interacts with this cavity structure to create a periodic set of reflections as a DBR off each individual grating that, to first order, builds up a resonant cavity mode of constructive interference off gratings. Together, this allows for photon density to collect inside the cavity until stimulated emission is achieved.

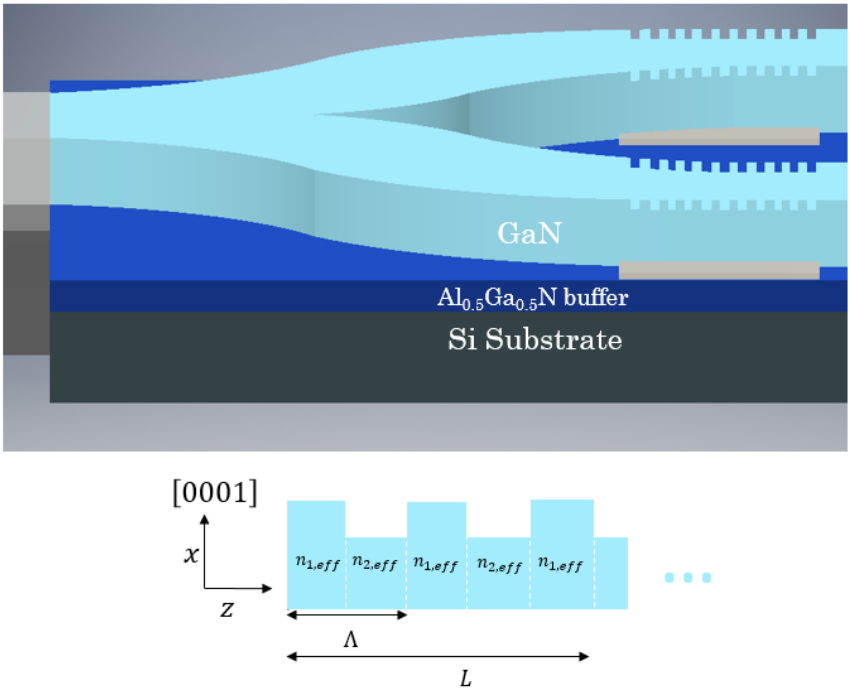

Figure 4.5 Gratings structure in GaN etched grating cavity. The upper picture shows the expected Y-branch heterogeneous layout, while the lower picture shows the Bragg grating depiction for finding the eigensolutions.

As this grating involves a physical stepping in material, this produces a periodic change in the permittivity along the cavity [90], as:

$$\Delta\varepsilon = \begin{cases} \varepsilon_{GaN} - \varepsilon_0, & \text{for } 0 < z < \dfrac{\Lambda}{2} \\ \varepsilon_0 - \varepsilon_{GaN}, & \text{for } \dfrac{\Lambda}{2} < z < \Lambda \end{cases} \tag{4.7}$$

where $\Lambda = \lambda/2n_0$ is the Bragg wavelength as created along the cavity length by the period of the grating. This Bragg wavelength becomes the critical figure of merit for producing the reflections that match to a desired cavity longitudinal mode, λ [48]. This initial index change comes from the geometric grading variation, not yet by any electro-optic tuning.

Using an approximation of each transverse mode's spread as a plane-wave along the grating, coupled mode analysis produces an effective refractive index dependent on this geometric perturbation in permittivity down the z axis. The difference between each oscillating propagation constant—forward and backward reflecting terms—becomes:

$$\Delta\beta = \beta_0 - \frac{\pi}{\Lambda} \tag{4.8}$$

A coupling between these forward, $A(z)$, and backward, $B(z)$, propagating modes is therefore created along the depth of each grating in x by this same variation [90], as:

$$\kappa_{AB} = -\kappa_{BA}^* = \frac{\omega\varepsilon_0}{4}\int_{\Lambda} \Delta\varepsilon(x)|E_y|^2 dx = \Gamma k_0 \Delta n_p \tag{4.9}$$

This says that the effective index of an optically-confined mode directly describes grating coupling allowed. Because of the grating perturbation, the difference in coupling and propagation constant matching produces a set of eigenvalues, q, as solved by [48] that stipulate the relative coupling across a grating length as:

$$q = \pm\sqrt{(\Delta\beta)^2 + \kappa_{BA}\kappa_{AB}} \tag{4.10}$$

Incorporating the forward-propagating transfer matrix methods as described in Chapter 2, a total coupling condition can be found for a given length of periodic index steps [48]. For a single effective index interface incident to a propagating field, a single *M* matrix term defines this, whereby a coupled equation set emerges for this interface as:

$$\frac{\partial}{\partial z}\begin{bmatrix} A(z) \\ B(z) \end{bmatrix} = iM\begin{bmatrix} A(z) \\ B(z) \end{bmatrix} \tag{4.11}$$

$$M = \begin{bmatrix} \Delta\beta & \kappa_{AB} \\ \kappa_{BA} & -\Delta\beta \end{bmatrix} \tag{4.12}$$

This presents the relation that for each grating interaction, a cross-term coupling κ transfers power between the two directions while the $\Delta\beta$ term determines what passes through in the same direction. As each of these interfaces build up, a total n number of M terms are combined together, producing a matrix coupling effect along an effective grating length L_{eff} as:

$$\begin{bmatrix} A(z) \\ B(z) \end{bmatrix} = M^n \begin{bmatrix} A(0) \\ B(0) \end{bmatrix} = F \begin{bmatrix} A(0) \\ B(0) \end{bmatrix} \tag{4.13}$$

where F becomes a product of multiple reflecting surfaces that approach resonance for particular eigenvalues, as:

$$F = \begin{bmatrix} \cos(qL) + \frac{i\Delta\beta}{q}\sin(qL) & -i\frac{\kappa_{AB}{}^{*}}{q}\sin(qL) \\ i\frac{\kappa_{AB}}{q}\sin(qL) & \cos(qL) - \frac{i\Delta\beta}{q}\sin(qL \end{bmatrix} \tag{4.14}$$

Extracting from this dispersion relation implicit in F, a stopband condition can be found that states what range of frequencies experience full reflection due to the grating periodicity Within the *transmission stopband*, this turns the resonant propagation constant eigenvalues imaginary, meaning $q = -iS$, converting all sinusoidal resonance terms to hyperbolic terms so that power couples into a particular resonant term and continuously reflects. This coincides with a single β_0 that best approaches $\frac{\pi}{\Lambda}$ in value to resonate [48]. Thus, the chosen longitudinal mode can be found by investigating the reflection characteristics of the grating structure. Employing standard transfer matrix identities, the reflection peak goes as:

$$|R(0)|^2 = \left|\frac{F_{21}}{F_{22}}\right|^2 = \left|\frac{i\kappa_{AB}\sinh(SL)}{S\cosh(SL) - i\Delta\beta\sinh(SL)}\right|^2 \tag{4.15}$$

4.6.2 Grating Structure

This design of gratings therefore allows for the goal of scalable heterogeneous integration, as now dependent on the length and depth of the grating, so that a sharper reflection peak can better select out a single wavelength for resonance. Utilizing a base set of GaN waveguide dimensions of 3 μm (width) x 1 μm (height) that allows for the desired telecom wavelengths to propagate as single-mode, as discussed further, a series of gratings aimed for reflection at λ = 1550 nm is etched atop the GaN with geometric periodicity at Λ = 1550 nm/2(2.28) = 337 nm. Each grating is established to be etched down to a depth of 200 nm out of the 1 μm on a rectangular GaN waveguide, shown in Figure

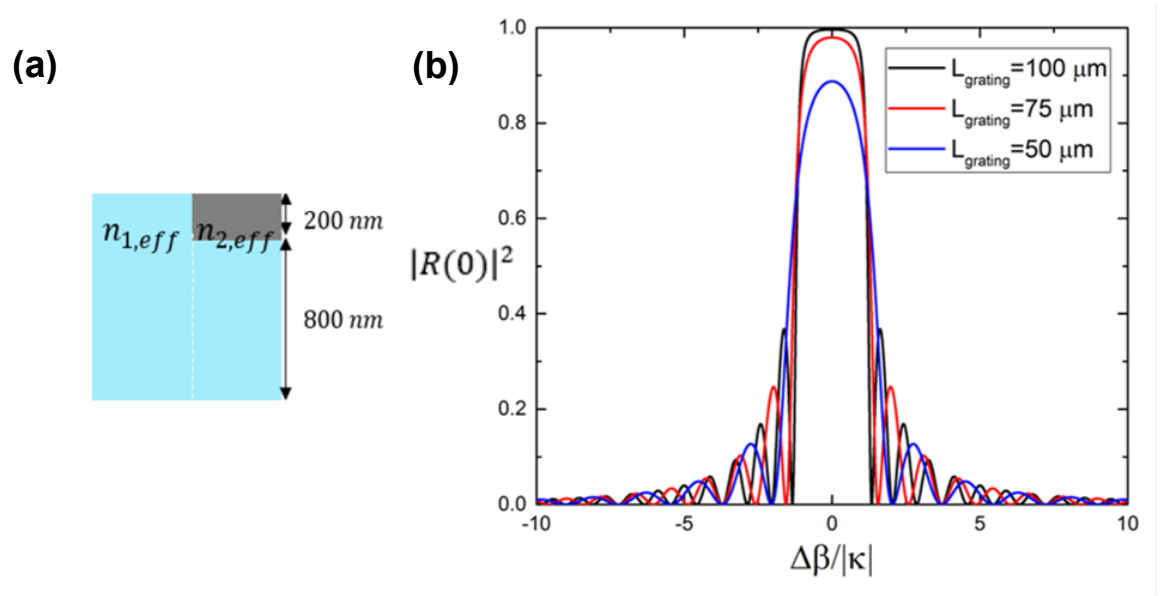

Figure 4.6 Zeroth-order effective index approximation of etched grating geometric interfaces shown in (a) while the plot of reflectivity for a sweep of etched grating lengths is in (b), showing stopband emerging.

4.6a. This then means that only a percentage of the propagating mode will interact with the grating structure and induce coupling. Using a reasonable approximation of the optical confinement overlap with the gratings as $\Gamma = .05$ and by noting that a piece-wise index can be constructed out of the grating delta producing $\Delta n_p \cong \Delta n_{eff} = n_{1,eff} - n_{2,eff} \cong 0.16$, a value for the coupling coefficient is found as:

$$\kappa_{AB}(1550\ nm, \Gamma = .05) \cong 3.24 \times 10^4\ \mathrm{m}^{-1} \tag{4.16}$$

A system solver is then produced to find the reflection spectra from (4.15) with (4.8) for this particular Bragg wavelength, shown in Figure 4.6b. This shows that the reflection spectra across grating lengths varies, thereby noting that an optimization must be found between integrating the system down for maximum scalability and extending the grating length to better design a cavity capable of sufficient reflection. A grating length, $L_{grating}$, of 75 μm consisting of roughly 225 individual Bragg grating periods is chosen to allow for sufficient reflectivity and thus cavity buildup.

As this would allow for reflection and tuning around a single peak resonant with the gratings, the total integrated design is extended to utilize the Vernier effect of mode-hopping between cavity branches. Noting Fourier transform rules, a series of gratings spaced out along the propagation axis of each cavity branch is known to produce a frequency comb of constructively-interfering reflection spectra known as a sampled grating DBR (SGDBR) [91], as shown in Figure 4.7. Each stretch of gratings produces closely-spaced reflection peaks in momentum space. The Fourier series equivalent shows how each reflection peak is separated, and this in turn defines the possible longitudinal modes that can experience enough gain to overcome losses and thus lase [49]. The fact that these peaks are closely spaced and that each Y-branch contains its own unique set of sampled gratings presents the path for mode-selection [92]. It is this integrated setup that will allow for the novel effect of using GaN for cavity wavelength tuning to produce its maximal effect. Thus, a total length of sampled gratings that denotes the total DBR length from one set of gratings

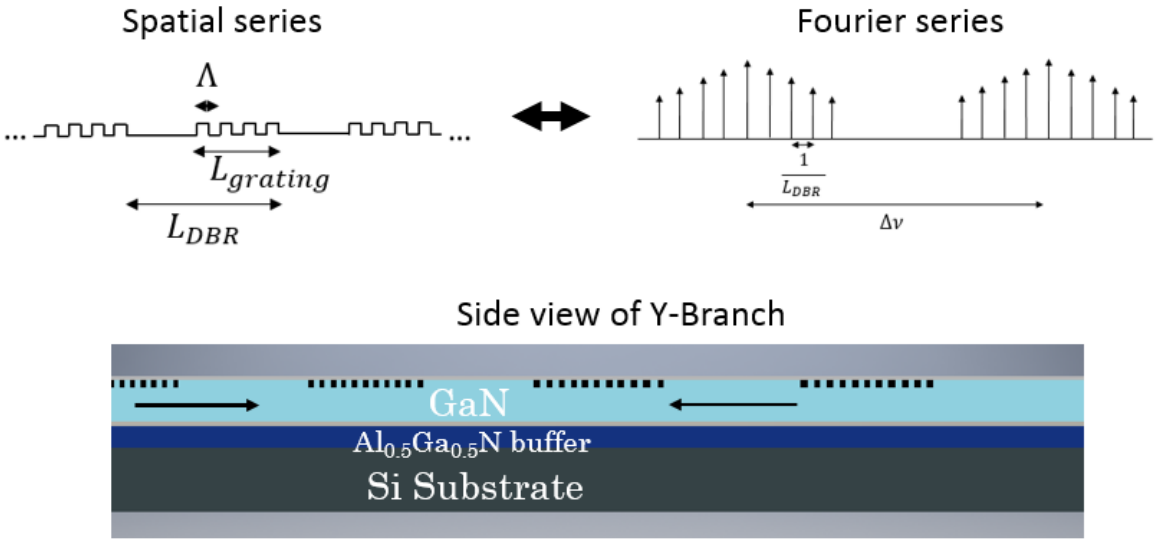

Figure 4.7 Sampled grating theory, showing a Fourier frequency series emerges from a grating distribution.

to the next, L_{DBR}, is produced atop the GaN waveguide. It becomes apparent that two orders of tuning can be employed: one that varies the index within a set of sampled gratings and gives continuous tuning over a range, and one that moves the set of longitudinal modes in one branch relative to the other and gives discrete tuning over a mode-hopping range, i.e. the Vernier effect. By noting that the coupling coefficient in (4.9) depends on Δn within a single grating period, the nature of GaN's anisotropic electronic-photonic properties comes through.

4.6.3 Electro-Optic Tuning

If the gratings are aligned with metal contacts in a traveling wave setup, a bias can be applied across them and allow for an appreciable Pockel's effect to change Δn. This controllable bias produces an electric field upward between the contacts, as E_z. With the GaN being chosen such that its c-axis is upward in x and so propagation is in-plane in z, the ordinary refractive index of GaN can be used as $n_o = 2.28$. Then, by utilizing the Δn relation in (4.3) and using the r_{13} and r_{33} values for the electro-optic/Pockel's effect that match directionally to the bias along E_z, it is found that:

$$\Delta n = -\frac{1}{2} n_o{}^3 (r_{13} \cdot E_z + r_{33} \cdot E_z) = -1.75 \cdot 10^{-11} E_z \tag{4.17}$$

This index variation happens separately to each grating it is applied to, depending on the individual bias and the resulting electric field this induces. An applied bias across a 10V swing is considered at each grating. To assure this methodology is in line with the goal of electronic-photonic integration via the CMOS, this bias is considered as separated into a +5V and a -5V bias, each separately applied to the contacts on the system. This is shown in Figure 4.8 where a universal contact is applied to all sampled gratings.

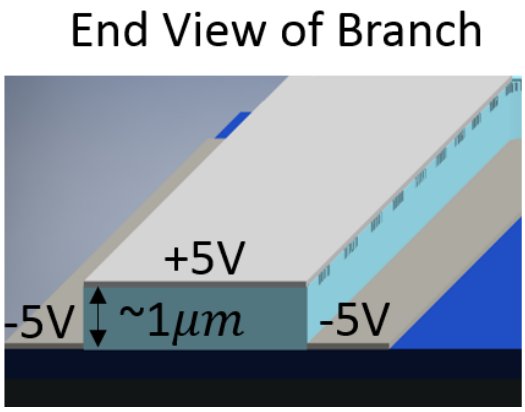

Figure 4.8 End view of electrode contact atop GaN waveguides, enabling distributed Pockel's effect.

Considering that the 10V field is applied over a 1 μm etched GaN waveguide thickness, this produces an overall index tuning possible of:

$$\Delta n = -1.75 \cdot 10^{-4} \tag{4.18}$$

which is within the scale of typical index variation. The corresponding wavelength tuning range that this gives is by:

$$\frac{\Delta\lambda}{\lambda_0} = \frac{\Delta n}{n} \quad \rightarrow \quad \Delta\lambda = 0.12\ nm \tag{4.19}$$

This first-order effect using just the Pockel's coefficient via an applied bias thus produces a small though capable result of wavelength tuning.

4.6.4 Vernier Effect

It is seen later that this effect can be amplified greatly by use of additional piezoelectric effects for even greater electronic-photonic interplay. The desired range of tuning for an integrated device should be comparable to other forms in production a la thermal and carrier-injection tuning, so again the Vernier effect is employed for mode-hopping to extend this effect [49]. The Vernier effect is easily enabled in this single integrated design because of the Y-branch setup and the fact that GaN's anisotropic behaviors can be switchably turned on or off on the basis of an electronic-based effect. The Vernier effect proceeds by first incorporating into the laser cavity design a multi-mode interferometer (MMI) to split the photon density of the resonant field into the two branches. Then the applied bias is controllably applied to just one branch so that only that branch feels the Pockel's effect for index tuning. A phase-matching therefore occurs between the two oscillating photon densities, where each branch acts as its own Fabry-Perot and aligns to choose out only one longitudinal mode to overcome losses and lase. This occurs by causing the reflection Fourier series of each arm to overlap, as shown in Figure 4.9, and select out a particular mode on each arm at the exact location where the addition of the reflectivities, R_1 and R_2, sufficiently overcomes losses [93]. Together, it is expected that this design will enable wide-band tuning, where a continuous tuning ranging of sub-nanometer sizes

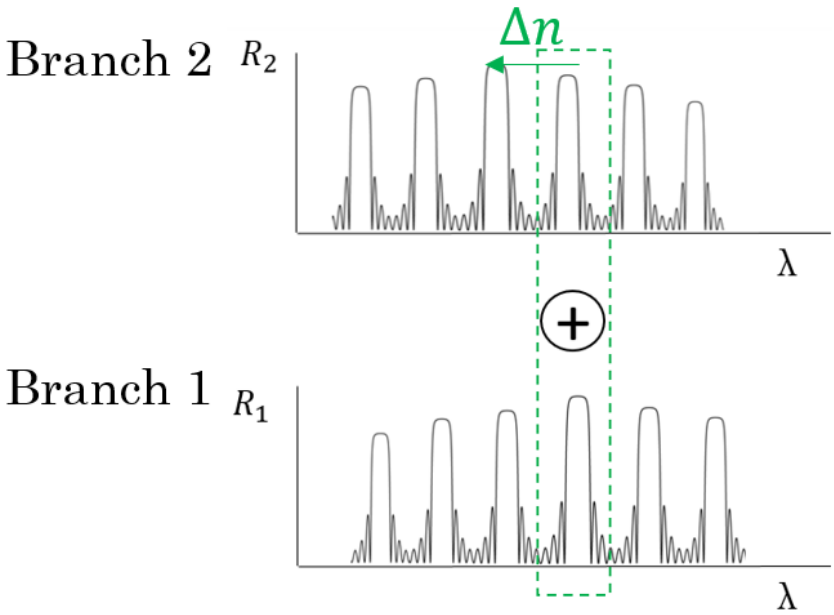

Figure 4.9 Vernier Effect for the Y-branch design. The matching of modes dependent on relative index changes is shown. The summation of Reflectivity, as opposed to multiplication, is unique to the Y-branch design.

becomes compounded in effect with a discrete mode-hopping range that together spans over tens of nanometers [49]. Using GaN in the Y-branch method maximizes flexibility in tuning as well as greatly reducing power losses due to the field-only effect; in addition, high side-mode suppression ratio (SMSR) exists due to the additive Vernier effect in tuning [94]. A GaN-based system is expected to possess switching speeds at <10 ns, limited mainly by the coupled electronic circuitry that drives the waveguide electrodes and thus enabling a scalable tuning system for wide-band multiplexing without a tuning current as other designs require [95].

In total, the proposed design in this work is analyzed and considered based on a sequence of findings on the optical coefficients in GaN and how this can best pair with various design geometric designs. The final layout for the design is shown in Figure 4.10. This final layout shows how the pairing of an InGaAsP-based QW gain region can be matched to a GaN-based grating region along with an MMI power splitter and a possible phase matching element to rectify the two branches. In total, this produces an expected cavity length of:

$$L = 2(L_{gain} + L_{phase} + L_{MMI}) + L_{eff,1} + L_{eff,2} \tag{4.20}$$

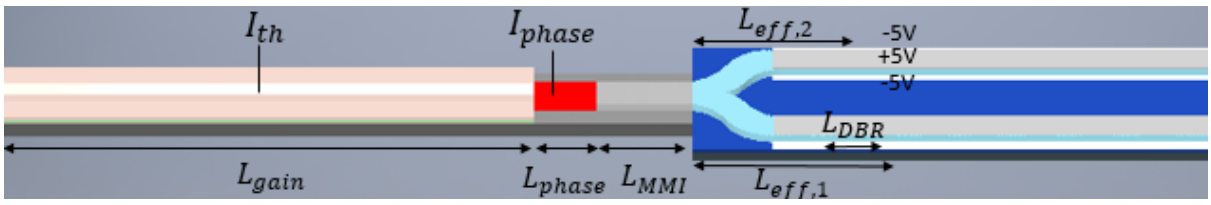

Figure 4.10 Final design of integrated laser. The leftmost piece shows the InGaAsP QW region with current injection contact, the rightmost shows the Y-branch GaN tuning design with voltage contacts. The center components show the interferometer and a potential phase control device to match the Y-branch outputs.

where typical values for each are given as $L_{gain} = 300\,um$, $L_{phase} + L_{MMI} = 100\,um$, and each L_{eff} denoting the effective penetration depth into the total grating structure (maximum of $300\,\mu m$) due to the longitudinal mode that is matched.

4.7 SAW DESIGN

4.7.1 Acoustic-Optic Structure

The piezoelectric parameters in wurtzite GaN allow for a combined photo-elastic and electro-optic effect on the crystal that can induce appreciable index changes when an applied acoustic wave causes electromechanical displacement, suggesting a separate scalable method for cavity tuning in GaN that can be made integrable for industry use. These benefits motivate a path forward in designing and implementing an integrated design for direct application to telecom systems that relates RF-driven acoustic structures with GaN-based optoelectronic structures as described above, where a single tunable cavity arm composed of a GaN waveguide can allow for efficient wavelength control and multiplexing across a wideband.

This tunable cavity consists of a SAW structure atop the GaN waveguide, enabling the production of a refractive index grating based on electronic RF stimuli. A schematic of the conceived end product for this endeavor is tested using FEM and effective index methods, where a wurtzite-grown GaN cavity structure is coupled to an InGaAsP gain chip. An RF inputted into an interdigital transducer (IDT) will result in a surface acoustic wave (SAW), caused by wurtzite GaN's piezoelectricity, which will propagate collinear with the optical beam in the waveguide and will induce a physical displacement atop the GaN structure [96]. The segment between the IDT and the waveguide will serve to focus the acoustic energy and launch a matched acoustic mode into the waveguide (Figure 4.11) [96]. Once there, by virtue of the photo-elastic and electro-optic effects in wurtzite GaN, the SAW induces a displacement, electric field, and strain along the length of the GaN waveguide.

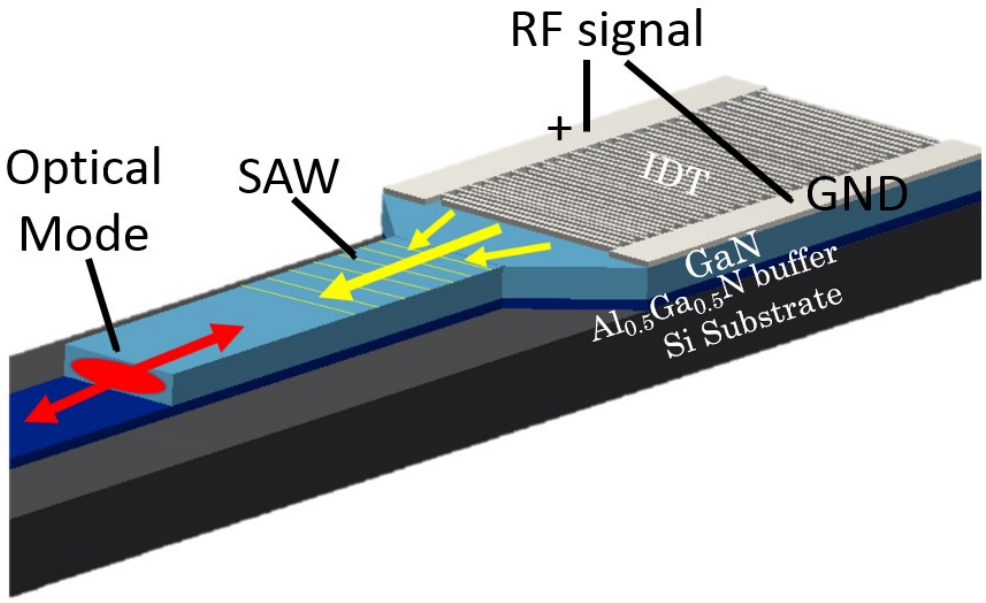

Figure 4.11 Design of GaN tuning structure, showing the IDT send in an RF signal (~GHz) that induces an acoustic perturbation that travels along the top of the waveguide and affects a resonant optical mode.

These combined effects impose a perturbative effect sinusoidally on the lattice, where offsetting Coulombic lattice forces stress the material and thus change the overall effective index spatially. This creates a mobile refractive index grating that spans across the waveguide which has the periodicity along the waveguide of the acoustic wavelength and an index perturbation strength (Δn) related to the acoustic power [97,98], as shown in Figure 4.11. This causes the waveguide to act collectively as a distributed reflector that encloses the laser cavity with an effective variable mirror capable of tuning and resonating at different optical longitudinal modes.

Unlike the geometric grating of a DFB laser as before, this acoustically-induced grating is not static and can be easily modified by altering the RF signal frequency applied to the IDT [99]. Each RF frequency matches to a separate grating spacing, meaning a different effective mirror is produced in the GaN waveguide simply by adjusting the coupled electronic signal applied to the transducer. A variable mirror based off changes to the index will then change the effective penetration depth of the signal into the mirror, similar to before with the sampled gratings, and thus overall changes the cavity length [48]. The variations in the cavity length are then manifest in their ability to control the resonance of the cavity and tune the output wavelength from the single branch GaN-based telecom laser.

The primary question regarding the feasibility of this idea is whether or not an acoustic wave can be generated within the GaN that is sufficiently strong to achieve the same effect as a DFB grating [99]. There are many details to be investigated herein but it is encouraging that efficiencies of 90% have been achieved with RF powers of 24 dBm [96] for an acousto-optic modulator in GaN. Separate studies have shown that AlN/GaN/sapphire or GaN/AlN/sapphire structures have greatly reduced insertion loss over simple III-N/sapphire designs, signifying that nested confinement of a SAW at piezoelectric material interfaces greatly enhances its effect [97]. Insertion loss and SAW velocity have also been found to be heavily dependent on thin-film thicknesses and acoustic wavelength [98], showing promise in the ability to design a geometry that accommodates best SAW/optical mode overlap.

In this design, an InGaAsP gain region is coupled to a grown GaN waveguide that terminates with a patterned set of IDT metal contacts to launch in the SAW. One end of the optical cavity will be a cleaved facet mirror to terminate the InGaAsP gain region, while the other end will be the variable SAW reflector. To accommodate typical telecom wavelengths in the C-band, the waveguide dimensions of the structure will be tailored to micron-scale such that all electromagnetic power is confined to nodeless Gaussian modes. The spacing of the IDT arms will be optimized to match to a desirable SAW wavelength that is compatible with GaN, and will be structured atop a GaN geometry that can focus its RF signal into the desired GaN waveguide. Thus, the integrated device will simultaneously maintain a propagating SAW wave, a resonating optical mode, and electrical inputs to both the gain region and the IDT (RF) that together allow for a highly-controllable tuning structure. This represents an optimal implementation of the goals of electronic-photonic integration, where the RF electronics and the telecom photonics work together to create reconfigurable circuitry atop a silicon (111) substrate for CMOS compatibility.

4.7.2 Single Transverse Mode Design and Results

To begin this design, the constraint is raised on how to assure that the GaN structure attached onto the InGaAsP gain chip produces single-mode transverse fields. Early assumptions in the sampled grating design

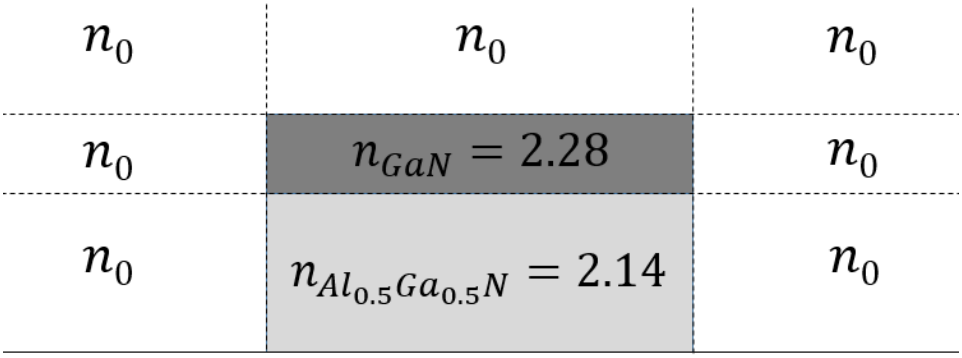

Figure 4.12 GaN-based waveguide index distribution for nine-segment effective index solver to determine dispersion relations.

approximated the oscillating longitudinal mode as a plane-wave, yet full consideration is now given to the cross-sectional spatial distribution of light as transverse modes. Given the nature of electronic-photonic integration, the output of an edge-emitting laser must be able to couple directly into a structure to be propagated via fiber or on-chip waveguide, and as such nodeless modes best confine the signal power. Noting that the boundary effects of the waveguide greatly determine what optical modes can propagate as described in Chapter 2, a waveguide is chosen such that only nodeless modes, HE_{00} and EH_{00}, are sustained.

An effective index solver is produced that predicts the expected modal indices for each given mode in a geometry. A programmable script is devised that produces the material refractive index for all III-N alloys utilizing aluminum and gallium together; with this, a buffer layer of $Al_{0.5}Ga_{0.5}N$ whose index is found to be 2.148 is placed beneath a core made of GaN whose index remains 2.28, as before. By constraining the width of the GaN waveguide to be 3 μm for good scalable lithography, the resulting geometry is shown in Figure 4.12, where now the effective index process is used to determine the thickness, d, of the GaN layer for confinement solely in the first set of nodeless modes.

Invoking the process in (2.36) and (2.38) as denoted before, an iterative process is formulated for finding *HE* modes is used such that first the effective index solver finds the *TE* indices for the GaN/AlGaN interface being a slab waveguide vertically, then it is constrained horizontally as *HE* into a rectangular waveguide, then finally it is used to extract an approximate core thickness from the full dispersion plot. The initial results and the normalized parameter, β, are shown in Figures 4.13 through Figure 4.15. In Figure 4.13a and Figure 4.13b, the slab waveguide solution for the center three effective index sections is found. It is seen that this formulation is upper-bound by the GaN core and lower-bound by the $Al_{0.5}Ga_{0.5}N$ cladding on bottom, with the thickness parameter included in the V-number x-axis sweep. Figures 4.14a and Figure 4.14b then show the dispersion plots after further confining the system horizontally. It is seen in these that now two sets of lower-bounds exist: one based on the lower core $Al_{0.5}Ga_{0.5}N$, and one based on the outer free-space index. Expectedly, the $Al_{0.5}Ga_{0.5}N$ index serves as the guiding cladding term, as any modes with indices between free-space and $Al_{0.5}Ga_{0.5}N$ will fully dissipate. Finally, Figure 4.15a shows the full relation of the normalized dispersion parameter, β, for the first few *HE* modes. Figure 4.15b zooms in on the onset of the first *HE* mode and pulls out the corresponding thickness term from the previous V-number.

From this, an approximation is therefore found from this solver that states the overall core thickness must be designed around 0.62 μm. This provides an aim for what the final waveguide should contain to maintain nodeless modal propagation. To produce a final solution that takes into account all boundary conditions, a 2D FEM solver is the next step in the method of finding the exact eigenmodes for a GaN-based integrated SAW-laser. The FEM is conducted using the software COMSOL run in a wave optics simulation for 1550 nm. Using the initial approximations from the effective index method where single mode behavior is seen at or around 0.62 μm of core thickness, the FEM solver further optimizes the design. The final geometric solution is plotted in Figure 4.16a and 4.16b. This shows that the 0.62 μm GaN core is split up into a ridge and neck portion of the rectangular waveguide, composed of a 0.5 μm ridge and a 0.12 μm neck underneath. This is found through iterative solutions in COMSOL, where it is seen that adding a small neck thickness to the core changes the overall effective index enough so the modes sit lower in the ridge, thus reducing index contrast and better suppressing higher-order modes. It is found that only the nodeless modes propagate, where the effective index of HE_{00} is n=2.1715, and for EH_{00} n=2.1615.

(a)

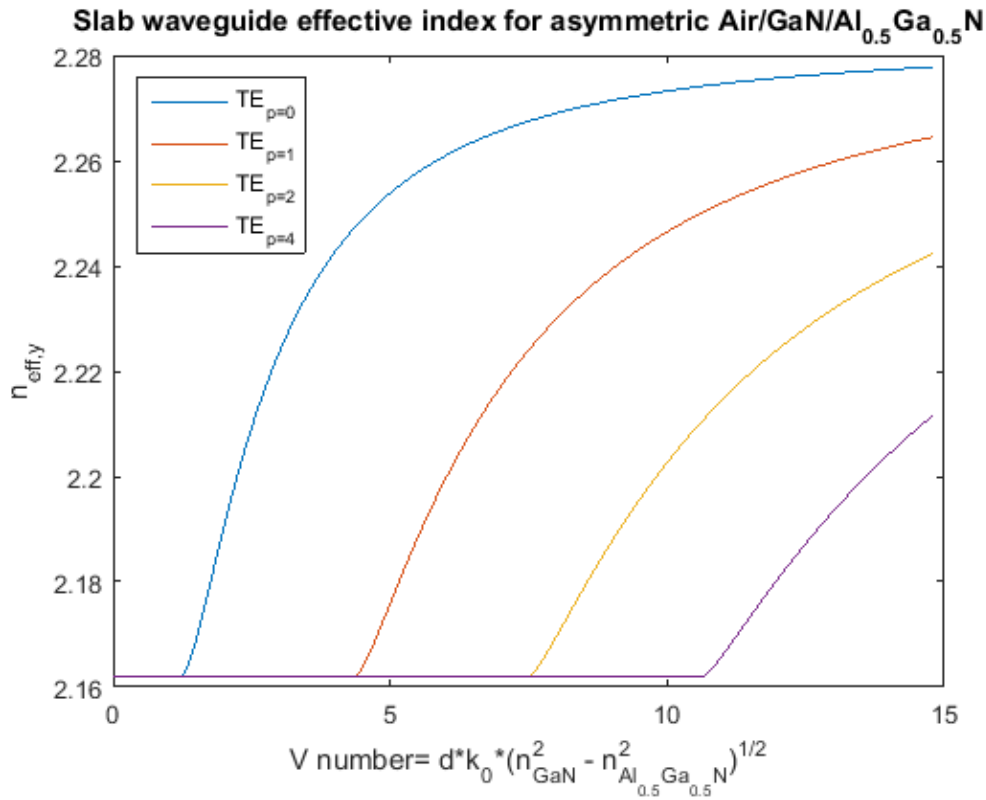

(b)

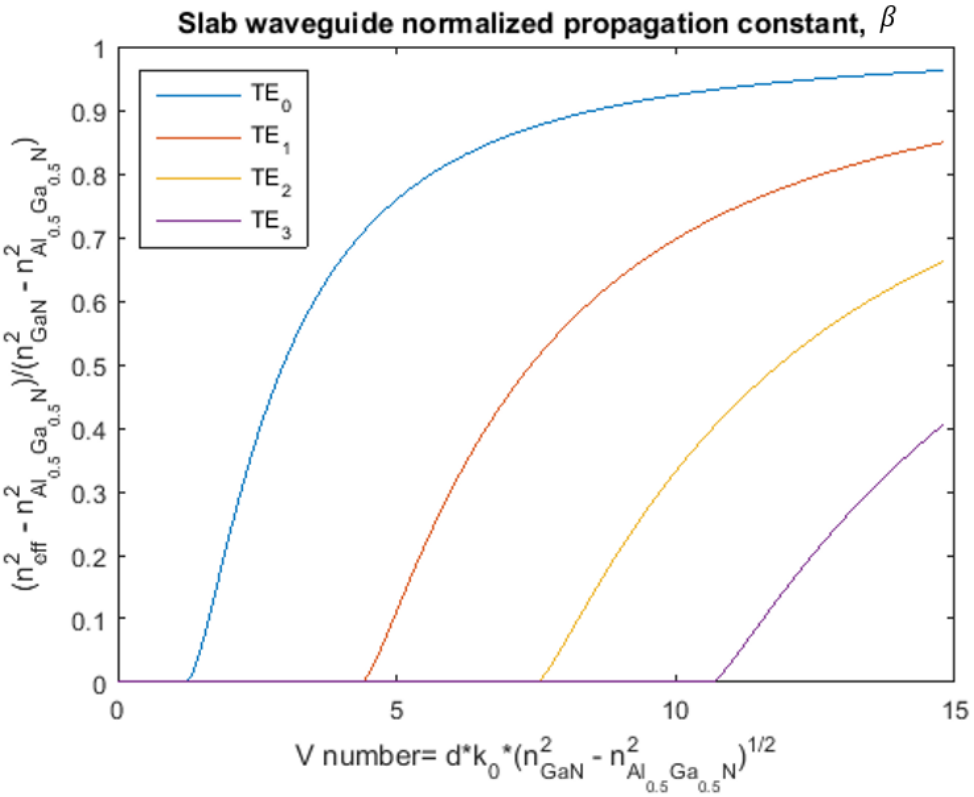

Figure 4.13 Plot from effective index solver for horizontal slab TE modes, Index vs. V-number, shown in (a), with the normalized results from solver, β vs. V-number, in (b).

(a)

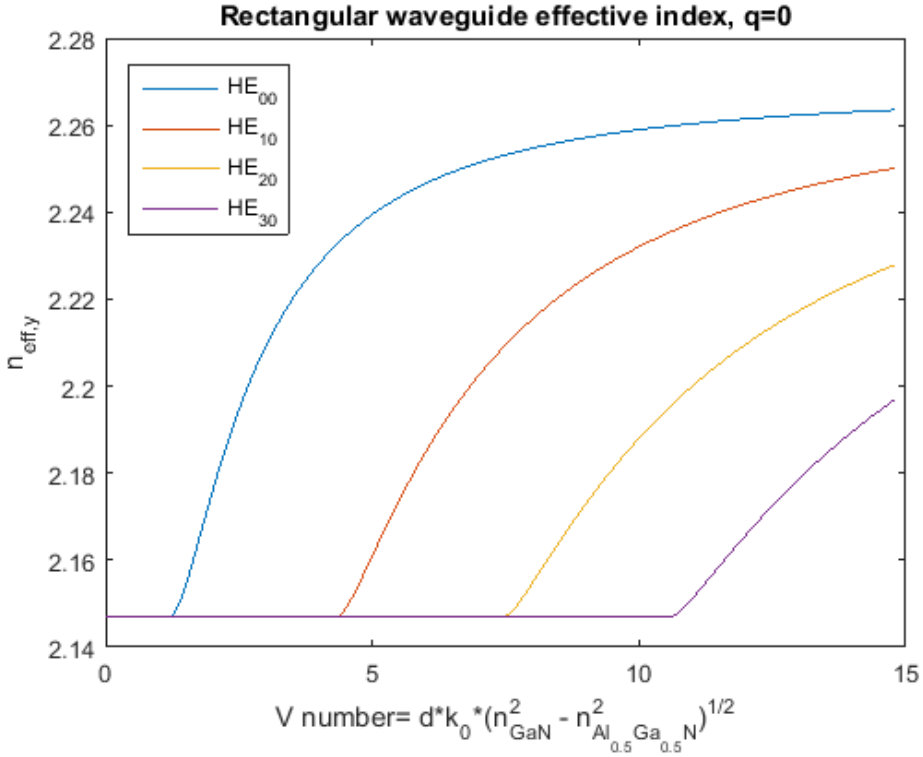

(b)

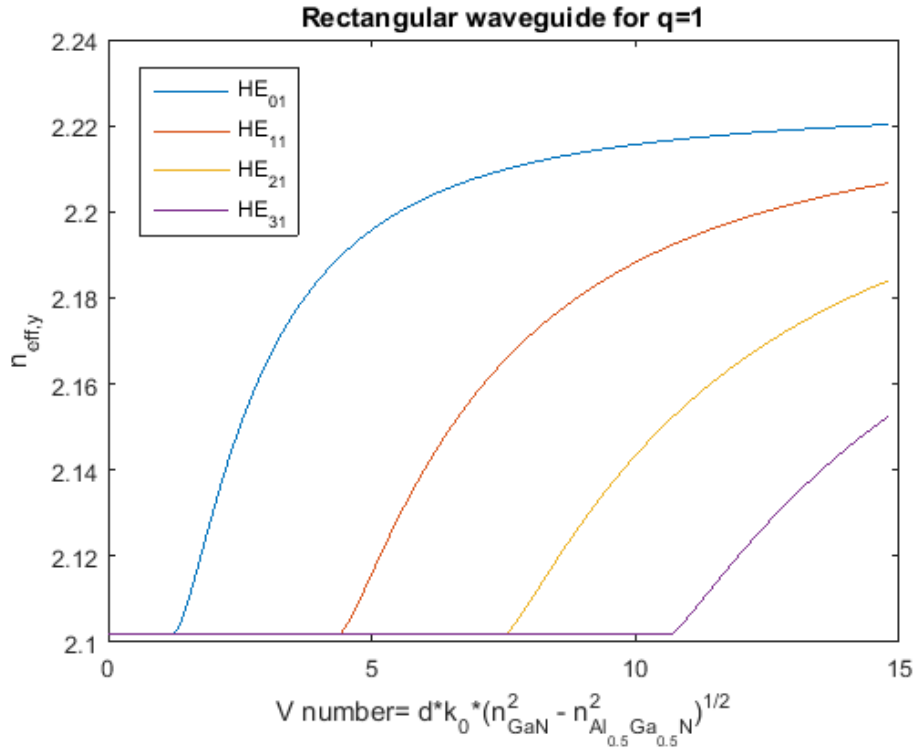

Figure 4.14 Plot from effective index solver for resultant vertical HE modes for q=0, Index vs. V-number in (a) with the resultant vertical HE modes for q=1, Index vs. V-number in (b).

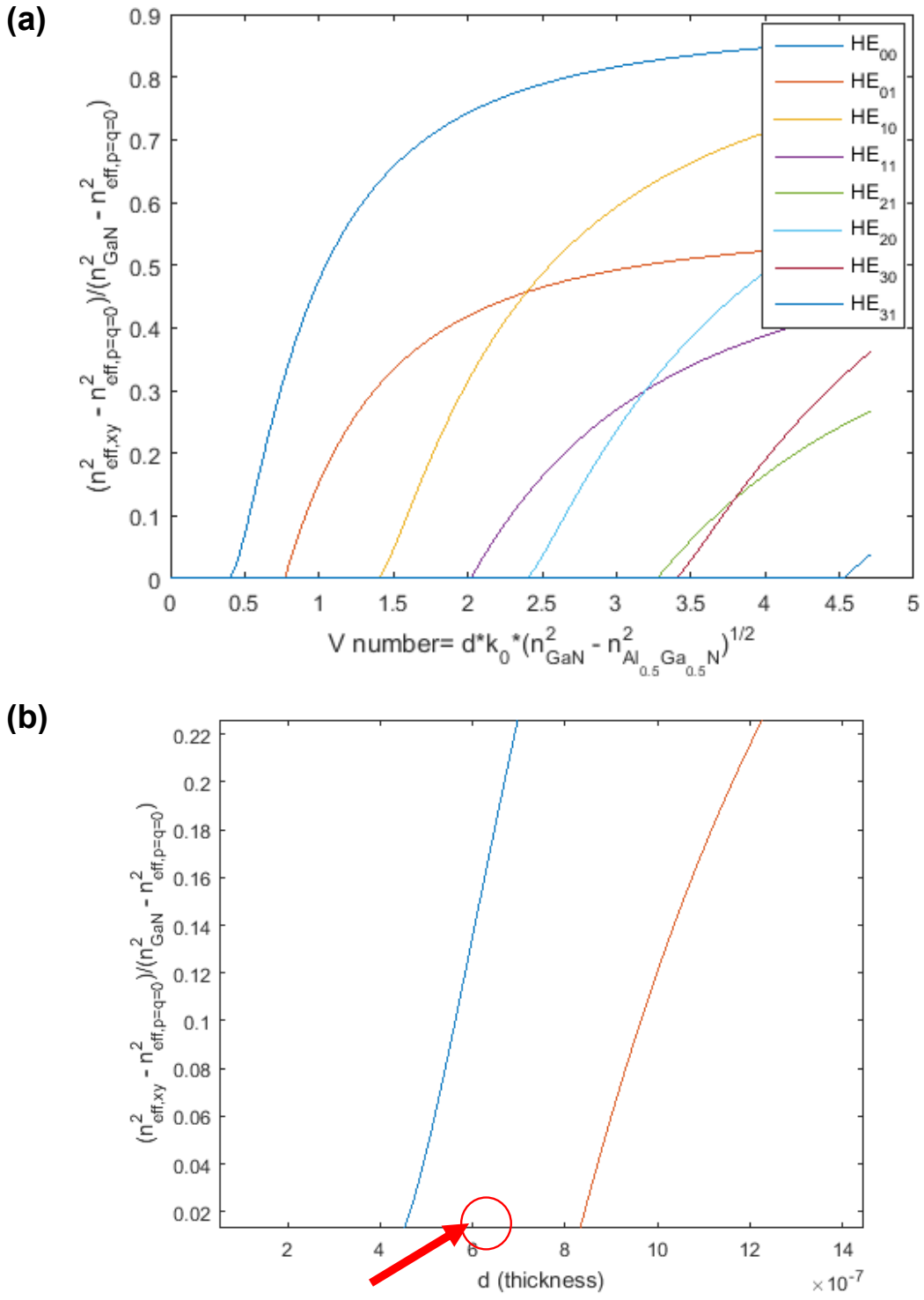

Figure 4.15 Plot of final dispersion curves, hinged to first modal onset p=q=0, β vs. V-number shown in (a) The overlap of the dispersion curves comes from the normalization basis. Each mode emerges from cutoff from its effective background cladding, a value interpolated from all nine-segments. The cutoff condition for the fundamental mode HE_{00} is seen. A zoomed-in plot of the final dispersion curves, β vs. Core thickness, is shown in (b), useful for finding the range of thicknesses possible for a fundamental mode waveguide.

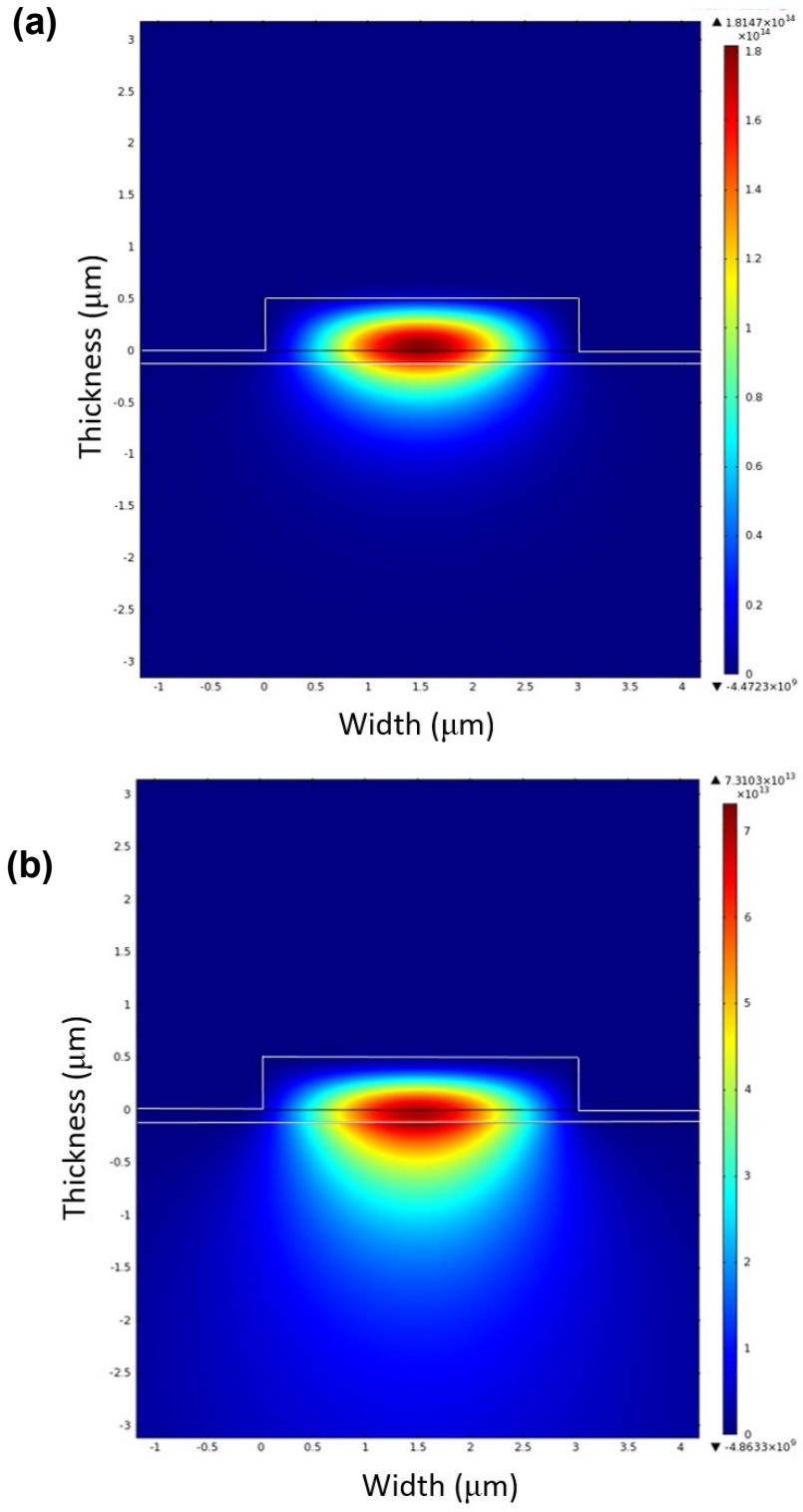

Figure 4.16 Plot of power distribution for FEM eigenmode solution to first propagating mode, $HE_{00,}$ as defined by waveguide geometry shown in (a), and for the second propagating mode, $EH_{00,}$ as defined by waveguide geometry shown in (b). This is the last mode that propagates. The power distribution in both is similar.

4.7.3 Piezoelectricity in GaN

To then combine the effects of the SAW on the GaN lattice to see whether an integrable tuning structure can be formed, the piezoelectric characteristics of the system must be known. This points to a set of equations denoting the the strain (S) on the lattice as [85]:

$$\begin{bmatrix} S_{xx} \\ S_{yy} \\ S_{zz} \\ S_{yx} \\ S_{yz} \\ S_{xy} \end{bmatrix} = \begin{bmatrix} \text{Compliance } (S_{ij})^{\vec{E}},\ 6\text{x}6, \frac{m^2}{N} \end{bmatrix} \begin{bmatrix} \text{Stress}(T_i), \\ 6\text{x}1, \frac{N}{m^2} \end{bmatrix} + \begin{bmatrix} \text{Coupling } (d_{ij})^{\vec{T}}, \\ , \frac{\partial S_j}{\partial E_i}^T, 6\text{x}3, \frac{C}{N} \end{bmatrix} \begin{bmatrix} \text{Field}(E_i), \\ 3\text{x}1, \frac{V}{m} \end{bmatrix} \quad (4.21)$$

where the strain is in all six coplanar/sheer directions and is unitless, and the Coulombic displacement (D) on the lattice as:

$$\begin{bmatrix} D_x \\ D_y \\ D_z \end{bmatrix} = \begin{bmatrix} \text{Coupling } (d_{ij})^{\vec{E}},\ \frac{\partial D_j}{\partial T_i}^E, 3\text{x}6, \frac{C}{N} \end{bmatrix} \begin{bmatrix} \text{Stress}(T_i), \\ 6\text{x}1, \frac{N}{m^2} \end{bmatrix} + \begin{bmatrix} \text{Permittivity } (\varepsilon_{ij}), \\ 3\text{x}3, \frac{F}{m} \end{bmatrix} \begin{bmatrix} \text{Field}(E_i), \\ 3\text{x}1, \frac{V}{m} \end{bmatrix} \quad (4.22)$$

In each of these, the variation to the lattice is determined by a conversion between electric field and stress via GaN material parameters. The electric field comes from the effect the SAW has in oscillating the surface of the lattice [99], producing a measurable field. The stress comes from the pressure applied by the SAW, as:

$$\begin{bmatrix} \text{Stress}(T_i), \\ 6\text{x}1, \frac{N}{m^2} \end{bmatrix} = \begin{bmatrix} \text{Elasticity } (C_{ij}),\ 6\text{x}6, \frac{N}{m^2} \end{bmatrix} \begin{bmatrix} \text{Strain}(S_i^0) \\ ,\ 6\text{x}1,\ [\ ] \end{bmatrix} - \begin{bmatrix} \text{Piezo } (e_{ij}), \\ \frac{\partial T_j}{\partial E_i}^S, 6\text{x}3, \frac{C}{m^2} \end{bmatrix} \begin{bmatrix} \text{Field}(E_i), \\ 3\text{x}1, \frac{V}{m} \end{bmatrix} \quad (4.23)$$

It is seen that there is a recursive effect between the produced field, strain, and stress in the lattice, governed by how the RF-driven SAW propagates along the surface of the GaN waveguide and perturbs the lattice. Typical values for each of these parameters are researched for application to telecom wavelength ranges and then inserted into the FEM simulation as [100,101,102,103]:

$$\begin{bmatrix} s_{11} & s_{21} & s_{31} & s_{41} & s_{51} & s_{61} \\ s_{12} & s_{22} & s_{32} & s_{42} & s_{52} & s_{62} \\ s_{13} & s_{23} & s_{33} & s_{43} & s_{53} & s_{63} \\ s_{14} & s_{24} & s_{34} & s_{44} & s_{54} & s_{64} \\ s_{15} & s_{25} & s_{35} & s_{45} & s_{55} & s_{65} \\ s_{16} & s_{26} & s_{36} & s_{46} & s_{56} & s_{66} \end{bmatrix} = \begin{bmatrix} 5.1 & -.92 & -2.5 & 0 & 0 & 0 \\ .92 & 5.1 & -2.5 & 0 & 0 & 0 \\ -2.5 & -2.5 & 6.7 & 0 & 0 & 0 \\ 0 & 0 & 0 & .04 & 0 & 0 \\ 0 & 0 & 0 & 0 & .04 & 0 \\ 0 & 0 & 0 & 0 & 0 & 12 \end{bmatrix} \cdot 10^{-3} \frac{m^2}{N} \quad (4.24)$$

$$\begin{bmatrix} d_{11} & d_{21} & d_{31} \\ d_{12} & d_{22} & d_{32} \\ d_{13} & d_{23} & d_{33} \\ d_{14} & d_{24} & d_{34} \\ d_{15} & d_{25} & d_{35} \\ d_{16} & d_{26} & d_{36} \end{bmatrix} = \begin{bmatrix} 0 & 0 & 8.2 \\ 0 & 0 & 8.2 \\ 0 & 0 & -16.5 \\ 0 & 8.0 & 0 \\ 8.0 & 0 & 0 \\ 0 & 0 & 0 \end{bmatrix} \frac{C}{N} \tag{4.25}$$

$$\begin{bmatrix} \varepsilon_{11} & \varepsilon_{21} & \varepsilon_{31} \\ \varepsilon_{12} & \varepsilon_{22} & \varepsilon_{32} \\ \varepsilon_{13} & \varepsilon_{23} & \varepsilon_{33} \end{bmatrix} = \begin{bmatrix} 5.35 & 0 & 0 \\ 0 & 5.35 & 0 \\ 0 & 0 & 5.38 \end{bmatrix} \frac{F}{m} \tag{4.26}$$

$$\begin{bmatrix} c_{11} & c_{21} & c_{31} & c_{41} & c_{51} & c_{61} \\ c_{12} & c_{22} & c_{32} & c_{42} & c_{52} & c_{62} \\ c_{13} & c_{23} & c_{33} & c_{43} & c_{53} & c_{63} \\ c_{14} & c_{24} & c_{34} & c_{44} & c_{54} & c_{64} \\ c_{15} & c_{25} & c_{35} & c_{45} & c_{55} & c_{65} \\ c_{16} & c_{26} & c_{36} & c_{46} & c_{56} & c_{66} \end{bmatrix} = \begin{bmatrix} 390 & 145 & 106 & 0 & 0 & 0 \\ -145 & 390 & 106 & 0 & 0 & 0 \\ 106 & 106 & 398 & 0 & 0 & 0 \\ 0 & 0 & 0 & 105 & 0 & 0 \\ 0 & 0 & 0 & 0 & 105 & 0 \\ 0 & 0 & 0 & 0 & 0 & 123 \end{bmatrix} \cdot 10^9 \frac{N}{m^2} \tag{4.27}$$

$$\begin{bmatrix} e_{11} & e_{21} & e_{31} \\ e_{12} & e_{22} & e_{32} \\ e_{13} & e_{23} & e_{33} \\ e_{14} & e_{24} & e_{34} \\ e_{15} & e_{25} & e_{35} \\ e_{16} & e_{26} & e_{36} \end{bmatrix} = \begin{bmatrix} 0 & 0 & -0.33 \\ 0 & 0 & 0 \\ 0 & 0 & 0.65 \\ 0.56 & 0 & 0 \\ -0.33 & 0 & 0 \\ 0 & 0 & 0 \end{bmatrix} \frac{C}{m^2} \tag{4.28}$$

Together, the parameters enable the RF-driven piezoelectric effects in the GaN material.

4.7.4 SAW Results in GaN

A simulation is then conducted using COMSOL. This simulation incorporated the above set of material tensors along with an RF frequency test at 10 GHz, with the goal of seeing the resultant material strain (S), electric field (E), and displacement on the lattice. To perform this, a GaN waveguide surrounded by air was structured to be 3 µm wide, 0.62 µm thick, and the SAW is launched between two IDTs that are 4 µm apart for initial tests,

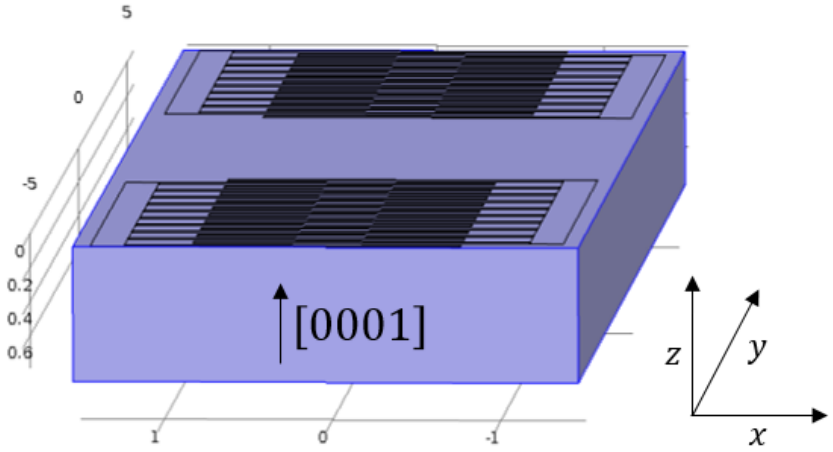

Figure 4.17 Diagram of simulated GaN-based SAW waveguide structure, in µm, for effective index tuning. The SAW will travel along y and perturb in z.

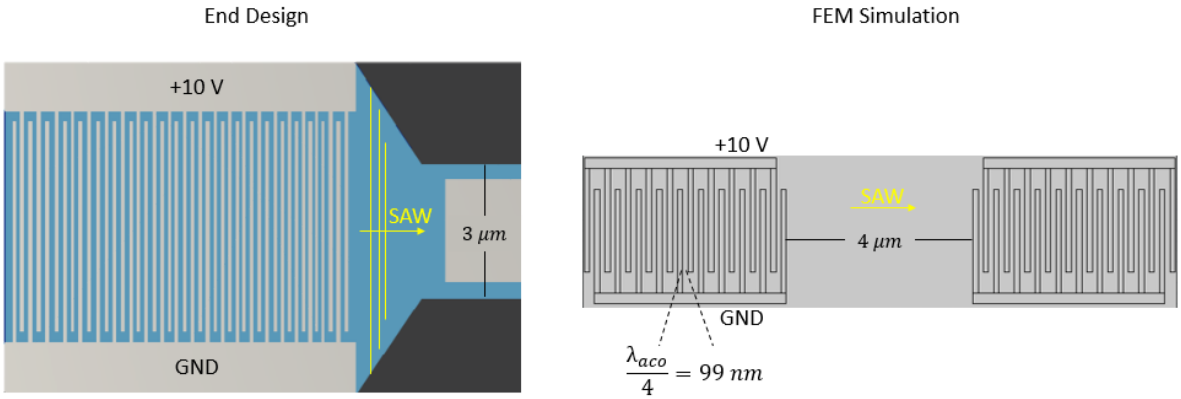

Figure 4.18 IDT design and schematic for effective SAW injection. The FEM approximates the IDT design and the focusing structure to compare the relative perturbation along a length of 4 μm.

as shown in Figure 4.17. These IDTs act to transmit and receive the RF signal biased at 10 V. The IDT is first designed to match to a particular range of RF drive frequencies, where the first round of simulations are run at a typical value of 10 GHz. To do this, known material parameters of GaN related to acoustic propagation are used, where the measured material density and the speed of sound inside bulk GaN go as [99]:

$$\rho_{DENSITY} = 6150 \frac{kg}{m^3} \tag{4.29}$$

$$V_{SAW} = 3996\ \mathrm{m/sec} \tag{4.30}$$

From these, an acoustic wavelength can be used to define the IDT, where:

$$\lambda_{aco} = \frac{V_{SAW}}{RF} = 399\ nm \tag{4.31}$$

The IDT consists of a series of patterned "arms" or digits that overlap and connect to one of two common contact electrodes that are used to drive the electronic signal feasibly from a separate integrated electronic device (Figure 4.18). The electrodes follow a similar Bragg wavelength spacing as with the etched gratings, and so are placed $\lambda_{aco}/4$ apart [48]. Thus, the integrated design is simulated to the same effect, where the SAW that produces the grating spacing emerges from the actual spacing of the electrodes. The resulting effects on the lattice from the SAW are found for a series of time-stamps.

First, the sequence of lattice displacements achieved by the SAW is plotted over time. In Figure 4.19, this is shown across two time stamps, with the displacement visually amplified to emphasize the lattice change. This displacement is shown to travel in time along the waveguide from left (Transmitter) to right (Receiver) as expected, giving an average displacement around 0.1 – 0.2 Å (Figure 4.20). This displacement emanates from the RF source point, as expected.

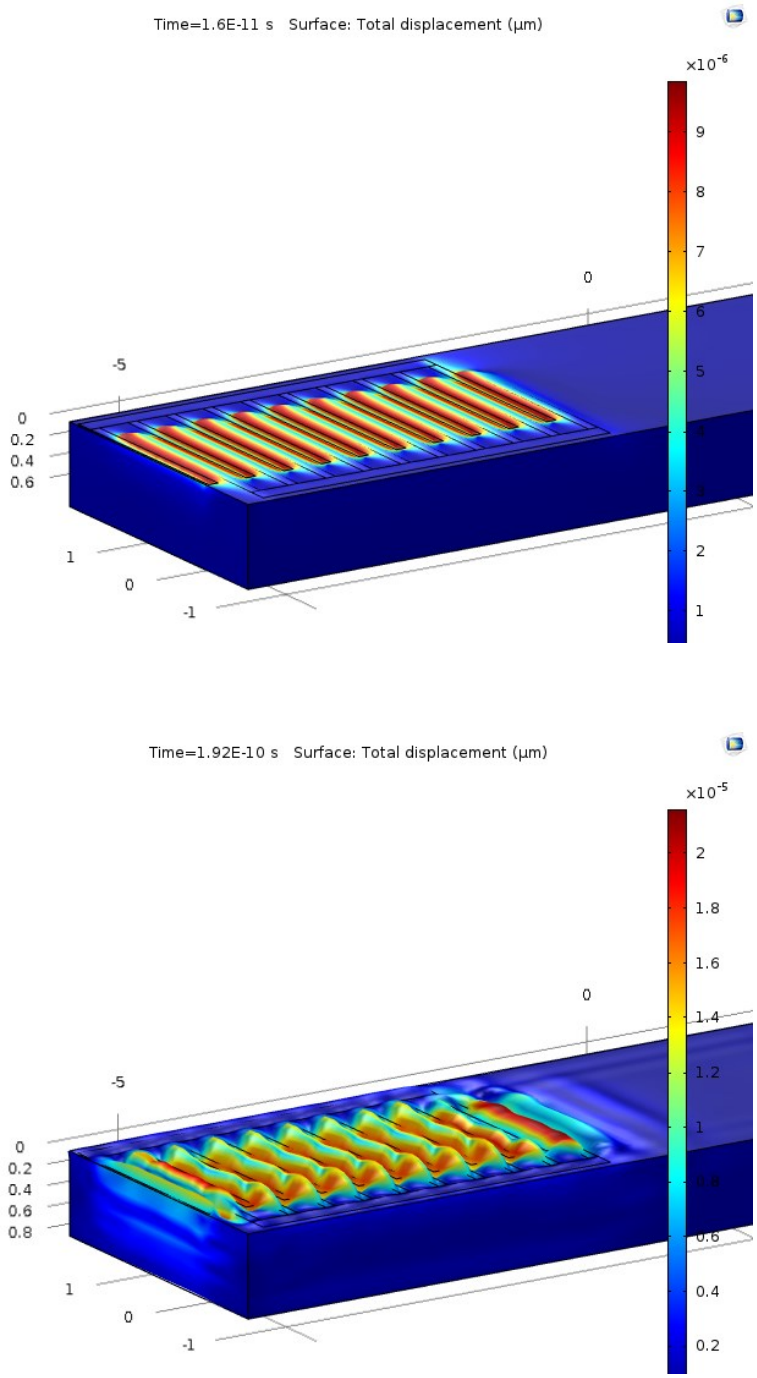

Figure 4.19 Displacement plots at different time stamp along GaN waveguide, showing the piezo-electric effects at (top) t=16 ps and (bottom) t=192 ps.

These displacement values prove in line with other SAW estimates in other materials, but it is noted that this relatively small value can produce large effects in induced strain (S) and electric field (E) on the lattice. By this, it is seen that an integrated SAW structure that heterogeneously combines an IDT structure atop the GaN cavity appears feasible.

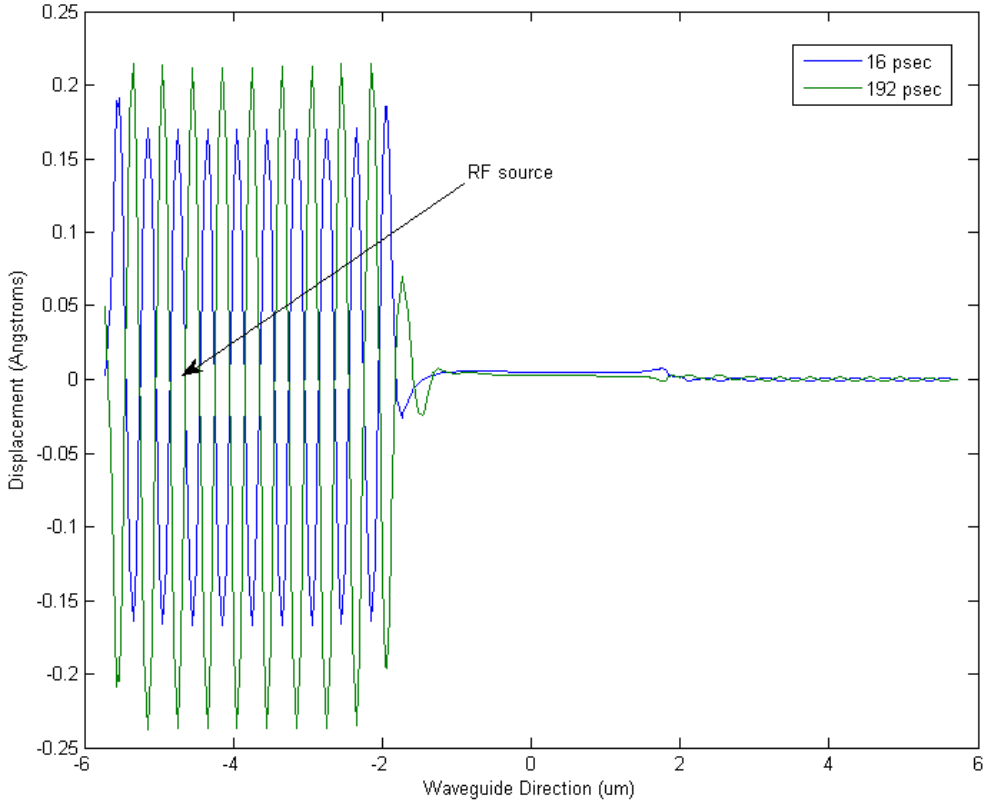

Figure 4.20 Plot of overlaid lattice displacement results along waveguide (Displacement vs. Length), showing propagation and average displacement values.

Shown in Figures 4.21 through Figure 4.23 are the results of the corresponding induced electric field onto the GaN waveguide. It is seen clearly that the field terms along the direction of the IDT is near zero, but along the growth axis (z) and along the propagation axis (y), there is a considerable 10^8 V/m field produced. Similarly, in Figures 4.24 through Figure 4.27, we see the various induced strains.

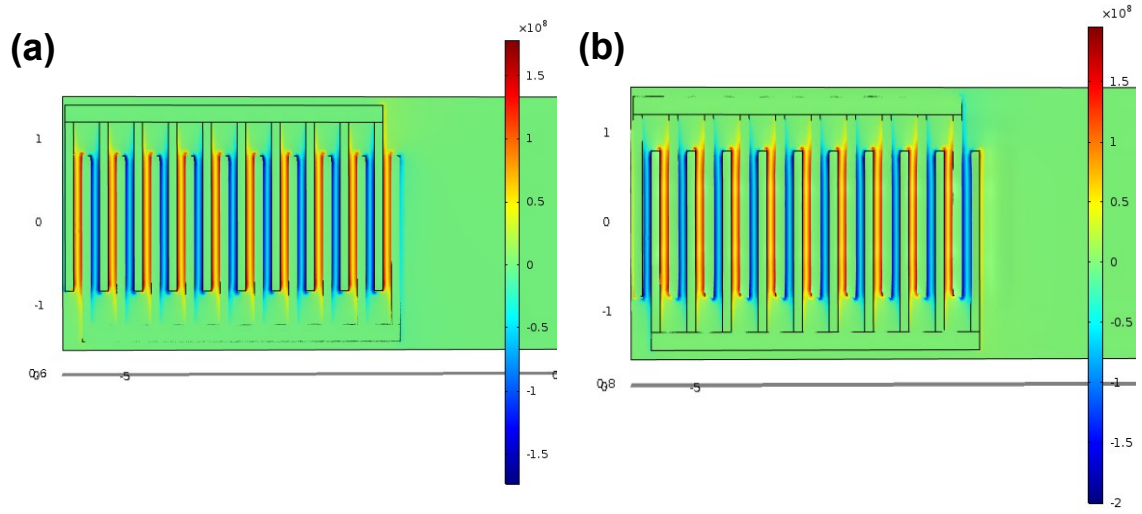

Figure 4.21 Time evolution of y-component of electric field, E_y, at t=32 psec in (a) and at t=176 psec in (b).

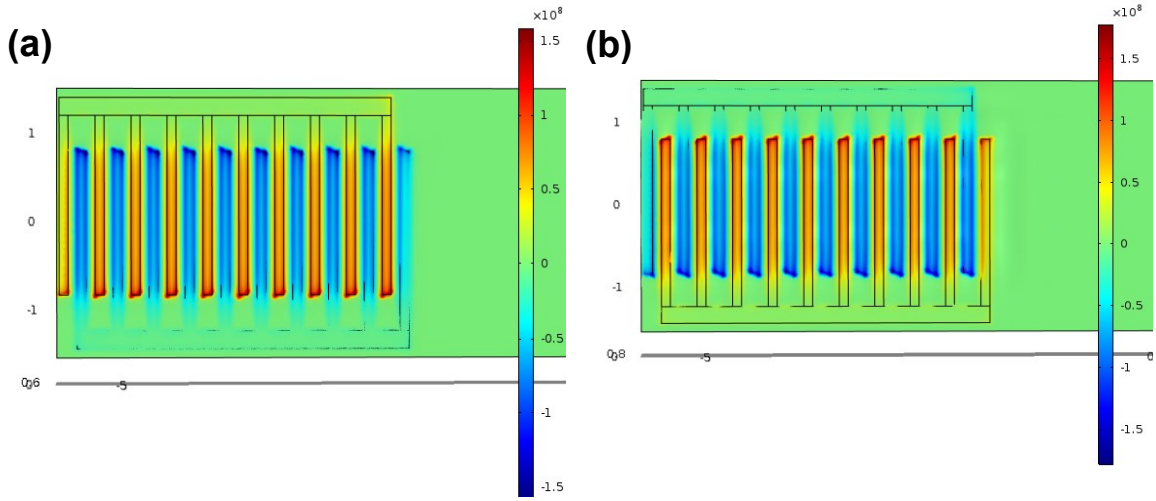

Figure 4.22 Time evolution of z-component of electric field, E_z, at t=32 psec in (a) and at t=176 psec in (b).

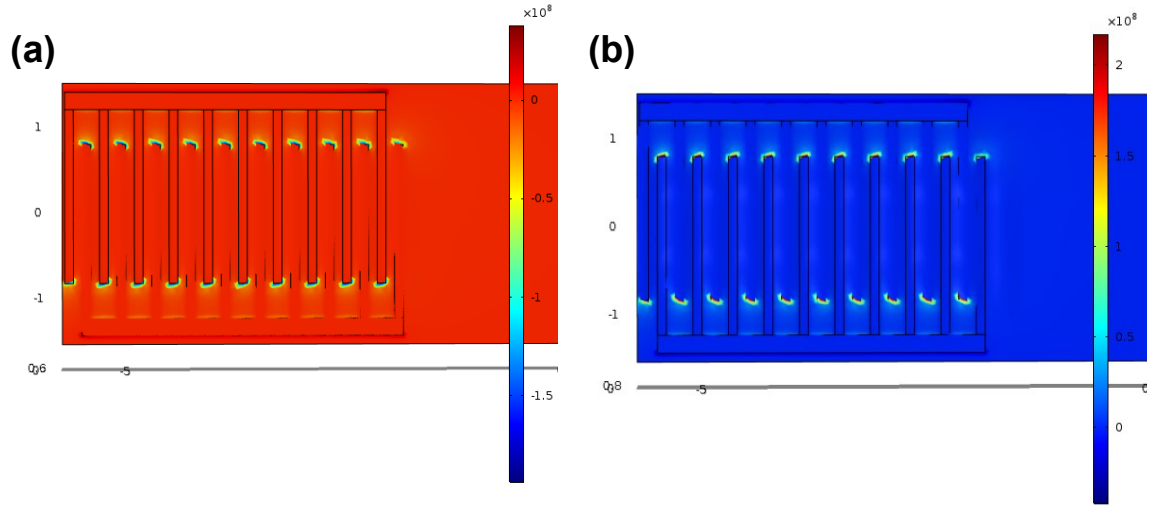

Figure 4.23 Time evolution of x-component of electric field, E_x, at t=32 psec in (a) and at t=176 psec in (b).

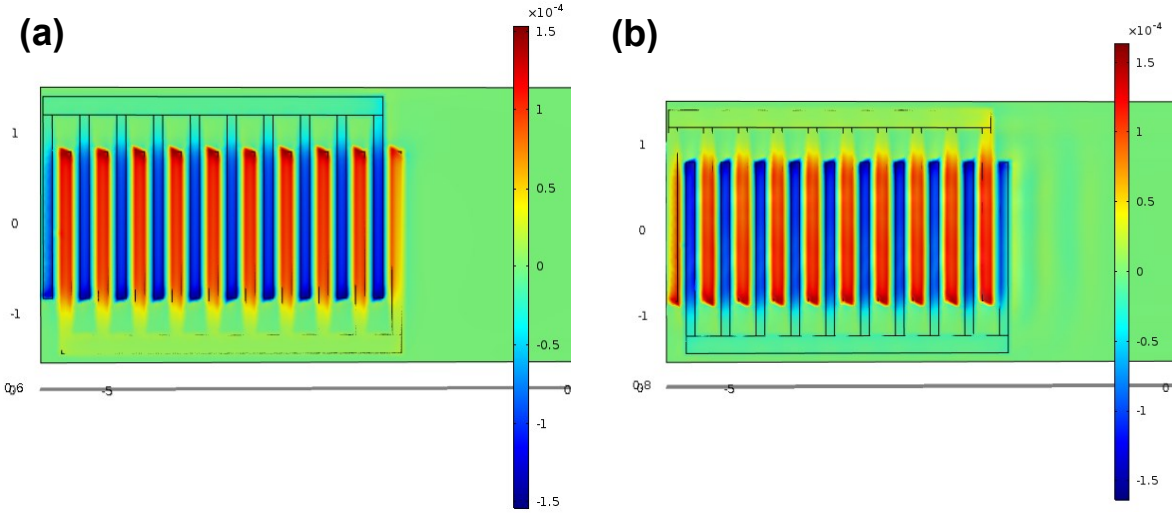

Figure 4.24 Time evolution of zz-component of strain, S_{zz}, at t=32 psec in (a) and at t=176 psec in (b).

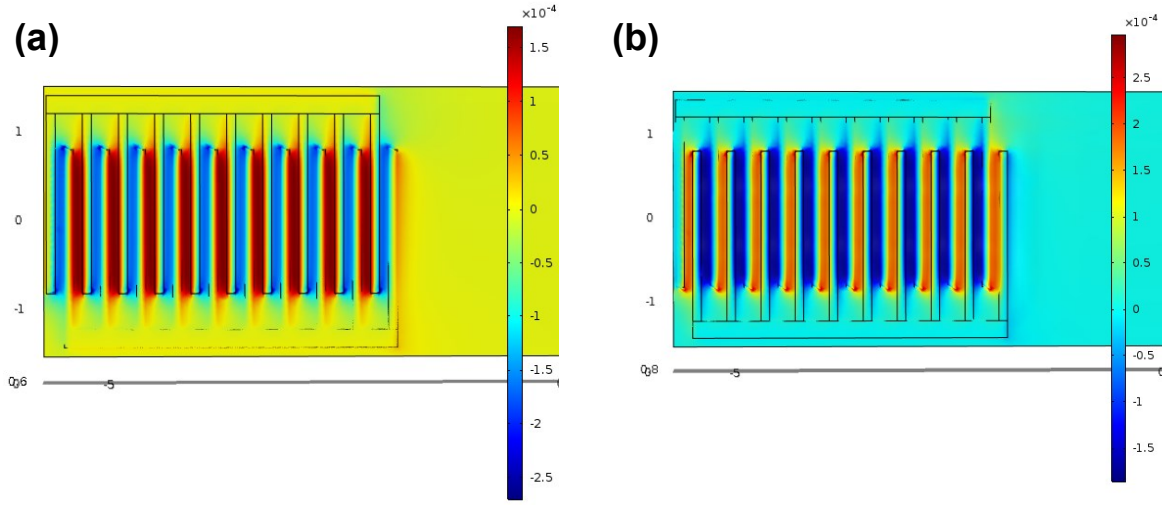

Figure 4.25 Time evolution of xz-component of strain, S_{xz}, at t=32 psec in (a) and at t=176 psec in (b).

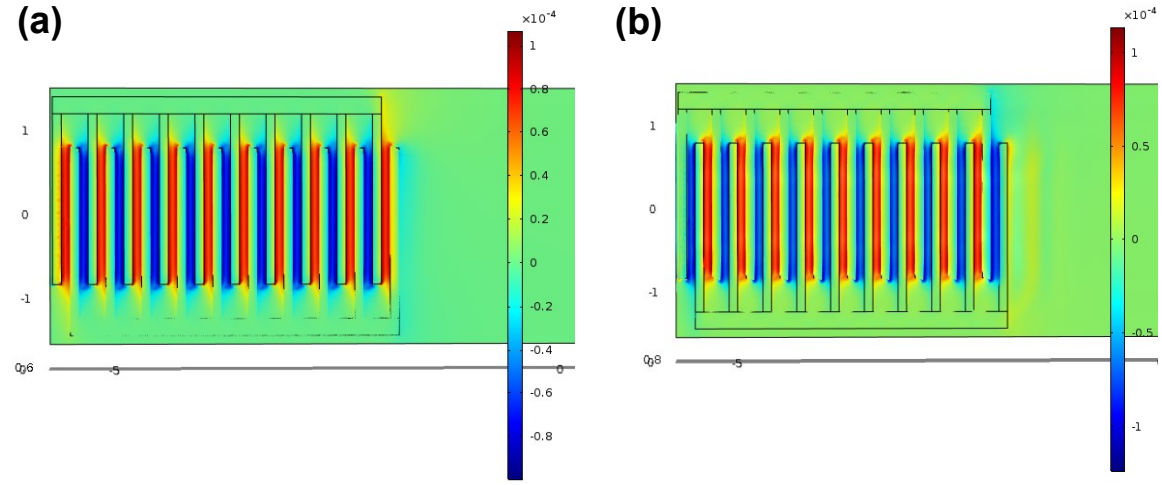

Figure 4.26 Time evolution of yz-component of strain, S_{yz}, at t=32 psec in (a) and at t=176 psec in (b).

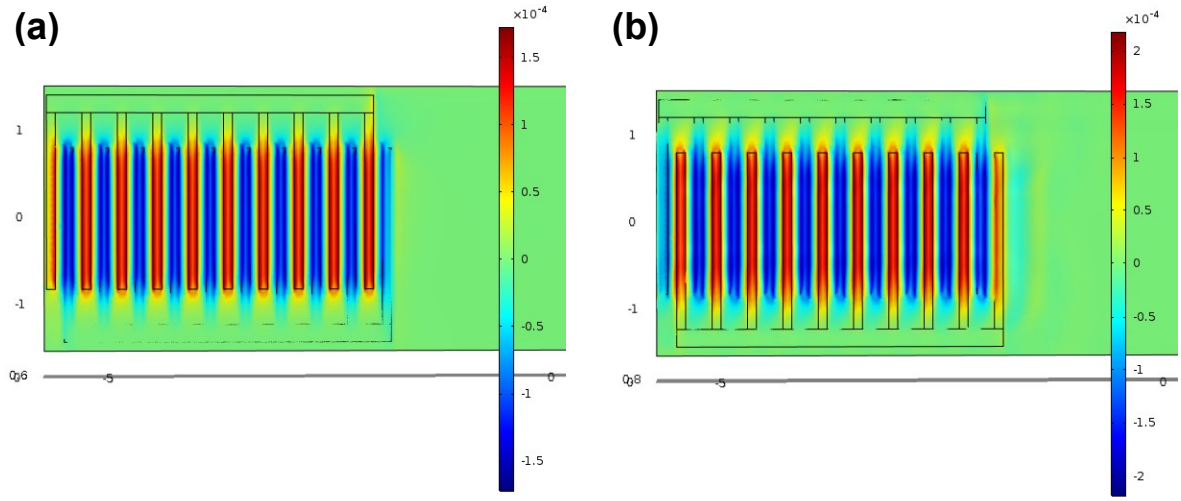

Figure 4.27 Time evolution of xy-component of strain, S_{xy}, at t=32 psec in (a) and at t=176 psec in (b).

As can be seen from these Strain results, the average values for the strain in each are ~10^{-4}. Together, this produces a starting point for what can be expected for the overall index shifts from the induced field at an RF signal of 10 GHz. Given that the photoelastic terms (10^{-2}) pair with the strains (10^{-4}) and the Pockels terms (10^{-12} m/V) pair with the electric fields (10^{8} V/m) to combine for a single index change, all contributing terms must be investigated in this work.

But looking at the material tensors, it is clear that only the E_z field term survives and that the S_{zz} strain term is dominant. Plotted in Figure 4.28 and Figure 4.29 is their overlap in time, where it is seen that the two effects have opposing signs as they propagate.

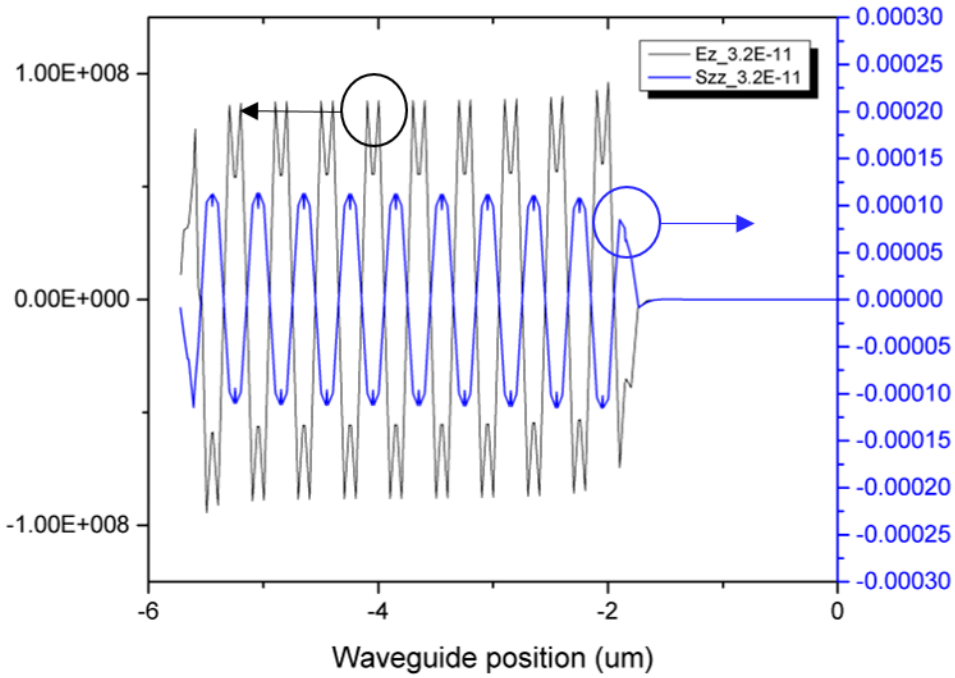

Figure 4.28 Plot of dominant electric field (E_z) and strain terms (S_{zz}) at t=32 psec.

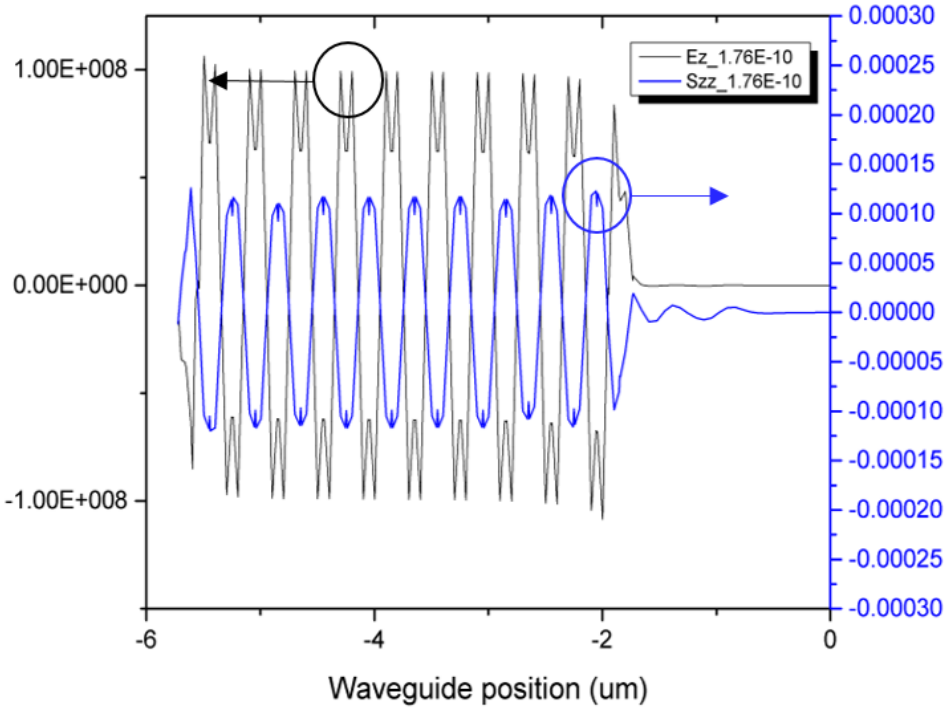

Figure 4.29 Plot of dominant electric field (E_z) and strain terms (S_{zz}) at t=176 psec.

Noting that the material tensors for the Pockel's effect and the photoelastic effect have opposite signs as well, as denoted before, it is clear then that the effects of the dominant contributing terms on the effective index change are additive. Together, this gives a conservative estimate of:

$$\Delta n \cong -\frac{1}{2}(2.28)^3[p_{31}S_{zz} + p_{32}S_{zz} + p_{33}S_{zz} + r_{31}E_z + r_{33}E_z]$$

$$= -5.926 \cdot [-1.25 \cdot 10^{-1}(1.25 \cdot\ 10^{-4}) + 2.96 \cdot 10^{-12}(1 \cdot 10^{8})]$$

$$= -1.84 \cdot 10^{-3} \tag{4.32}$$

This shows the exceptional capability of the SAW method for establishing a series of gratings along the integrated laser. This value is nearly 10x larger than the previous geometric etched grating design and is well within the expected range of current industry devices as driven by larger, less efficient controls. The value in (4.32) presents a highly encouraging path forward towards scalable designs, where the completed simulation for GaN-based systems presents promising results in finding a scalable set of photonic devices for DWDM. By employing a RF-based method to induce sinusoidal acoustic gratings along a GaN waveguide inside a laser, a wide-band range of tuning becomes readily attainable.

Given that this analysis is proceeded at 10 GHz, it can be expected that higher RF drive frequencies will produce a larger range of field and strain terms, thus extending the effect of wide-band tuning due to the Pockel's and piezoelectric effects beyond what a set of geometric gratings can do. Additionally, this design presents an

exceptionally clear formulation of the possibilities inherent when integrated devices are able to straddle the both electronic and photonic domains.

4.8 DISCUSSION

Here, we have developed methods whereby an electronic structure atop a GaN-based laser cavity can directly perturb the system to allow for efficient, controllable wavelength tuning. This allows for a close relation between the optical signal and any matching electronic inputs, as a CMOS-compatible layout would require. Two designs are discussed at length, one using geometric etched gratings and another using a dynamic RF-driven surface acoustic wave, where each allows for refractive index tuning sufficient for laser wavelength tuning. Each is presented as a heterogeneous design, where a GaN epitaxial structure (0001) grown atop silicon (111) is coupled to a standard telecom structure of an InGaAsP QW and controlled by an electronic system capable of inducing the optical effects in GaN. This then presents a compact and efficient method for making tunable lasers, utilizing the intrinsic anisotropies in GaN. As such, these designs are inherently scalable for network-level applications. It is conceivable that an electronic layout can be made and fabricated to overlay a photonic layout, each with its respective circuit elements, where the electronic signals act as reconfigurable inputs that dynamically prepare the photonic systems for a controllable optical signal. This premise therefore serves the goal of enabling DWDM systems that utilize small amounts of power yet with strong tuning ranges. For the gratings-based design, a relatively low static voltage (+10 V) with no major drive current is satisfactory to produce the effect of index tuning on the order of 10^{-4}, while for the SAW design typical values for the RF power (+10 V, 10 GHz) needed to create a SAW-effect in GaN capable of tuning on the order of 10^{-3} are around 5 μW [99]. This assures that the capabilities of this system can act as both a rapidly switchable and efficient means of laser cavity tuning. Further work can easily build off of this experimental design by considering the resolution of spaced RF-drive frequencies for a particular tunability range.

Together, the path forward in scaling up semiconductor lasers for network applications presents a challenge for wavelength tuning that is answerable via GaN-based structures. Widely known for its emitting effects in blue-green diodes, GaN has strong lattice-based effects that can be harnessed for a novel approach to laser cavity tuning. By introducing GaN waveguides into telecom-emitting cavity designs for tuning, a large step forward toward the singular goal of electronic-photonic integrated circuitry is made clear. This concludes the collection of findings that prove the capabilities of GaN-based photonic devices for the use in scalable integration methods.

CHAPTER 5: HETEROGENEOUS FABRICATION

"One shouldn't work on semiconductors, for that is a filthy mess.
Who knows whether any semiconductors even exist?"
-Wolfgang Pauli, 1931

5.1 MOTIVATION

To fabricate a reconfigurable network, the unification of electronic and photonic materials must be considered. Growth of III-V semiconductor materials on silicon has seen some headway despite lattice mismatches, but a more general method of material bonding is desired for rapidly scalable designs [104,105]. A heterogeneous distribution of semiconductor materials allows for various electronic and photonic devices to be connected as novel complex circuits, able to route and direct signals in a planar fashion through either the electronic or photonic domain. As it stands now, electronic-only designs have seen considerable success in designing fabrication techniques for monolithic silicon processing, where integrable CMOS devices have been calibrated for scalability [106]. Some monolithic photonic-only designs have constructed devices entirely from a single epitaxial structure, allowing for specialized designs in telecom-based applications [71]. Yet while CMOS networks are successful with a modest list of materials and photonic-only designs have merit for single-use designs, a heterogeneous electronic-photonic network has a larger span of III-V materials and thus the possibility for a much wider range of functionality. This acts as both an initial constraint and a potential advantage for heterogeneous photonic systems. Inadequate planning for such structures may throttle an electronic-photonic circuit design based on geometric limits, whereas sufficient coordination of the structures can enable new systems and logic networks [107].

This coordination and distribution of III-V materials on silicon is approached by considering how to fabricate photonic devices and align them with a CMOS host wafer. This alignment is crucial for proper signal propagation, since an electronic-photonic circuit is composed of individual elements that each act on a logical signal and each invoke some effect. As such, the ability to epitaxially transfer patterned photonic materials onto an established CMOS wafer and then construct electronic and photonic devices in unison with fine alignment is paramount [108]. Noting the merits of linking heterogeneous devices as described before in Chapters 1 through 4, an exceptional epitaxial transfer method would allow for a grid-like distribution of III-V materials atop CMOS that can be coordinated, constructed, and networked together in a single fabrication stage, assuring scalability. The result of this would produce transmitting, receiving, spectrally separating, and routing photonic devices that can span the range of III-V capabilities. Between these devices, waveguide structures could move wave packets and allow for reconfigurable networks, while embedded CMOS designs can enable electronic controls of the same. This work investigates these constraints of uniting these electronic and photonic materials and establishes a fabrication methodology for converting discrete device designs into such a single heterogeneous electronic-photonic circuit that is capable of large-scale networks and logic systems.

A scalable method is therefore desired that enables III-V photonic structures to be processed and defined in unison on CMOS-compatible silicon. Fabrication techniques designed for GaAs-based III-V photonic structures are shown, where a novel process that allows III-V epitaxial islands to be constructed across a silicon carrier wafer and prepared for epitaxial transfer onto a matching CMOS host wafer is presented. This process directly enables the transition to heterogeneous fabrication.

5.2 FABRICATION STEPS

The fabrication of any integrated circuit consists of a series of processing steps that allow for the careful definition and patterning of devices on a micron scale. For electronic-photonic integrated circuits, these process steps borrow their order from silicon-based CMOS processing, yet the particular tools and techniques utilized greatly vary. To construct this heterogeneous platform, a process is developed whereby a set of GaAs-based epitaxial structures can be distributed onto silicon for bonding preparation. Crucial to this method is that the GaAs material adheres throughout processing and is not damaged, assuring a good final bond onto a corresponding silicon feature. Given the complexities inherent in this methodology, each step is explained.

5.2.1 Temporary Bonding Polymer

Given the intent of readying III-V materials for a flip-chip bond onto CMOS, the first step in this work is to provide for a temporary, reversible adhesion between III-V and a silicon carrier wafer. Shown in Figure 5.1a, a 2" silicon wafer is utilized as the carrier wafer for processing bonded GaAs-based III-V epitaxial structures distributed in smaller squares on top. The GaAs material is an epitaxial structure that is cleaved into <25 mm^2 area pieces from larger wafer-sized pieces that can be arranged in a grid-like fashion on the silicon, as in Figure 5.1b. To unite these materials, the use of a commercially available temporary-bonding polymer is extended for heterogeneous integration, going beyond prior uses of it for silicon-only processing. Consisting of a petrol-based anisole solution, the temporary bonding solution allows for semiconductor wafers to be held reliably for a specified duration and then to be removed afterwards by either chemical or mechanical slide removal processes [109]. The polymer is chosen given its known rigidity and successes in silicon-based transfer processes, though a full investigation into its use for III-V-on-Si is now

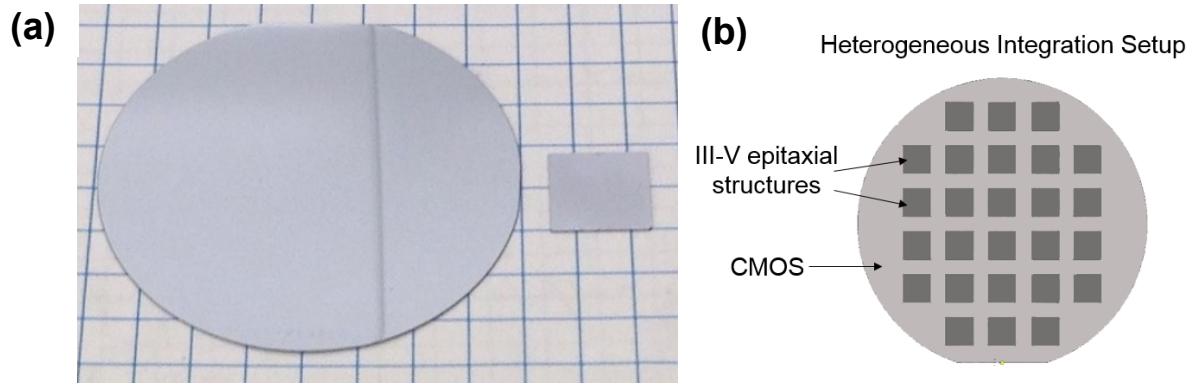

Figure 5.1 Initial wafers of silicon (large) and GaAs (small) in (a). The grid-like arrangement is in (b).

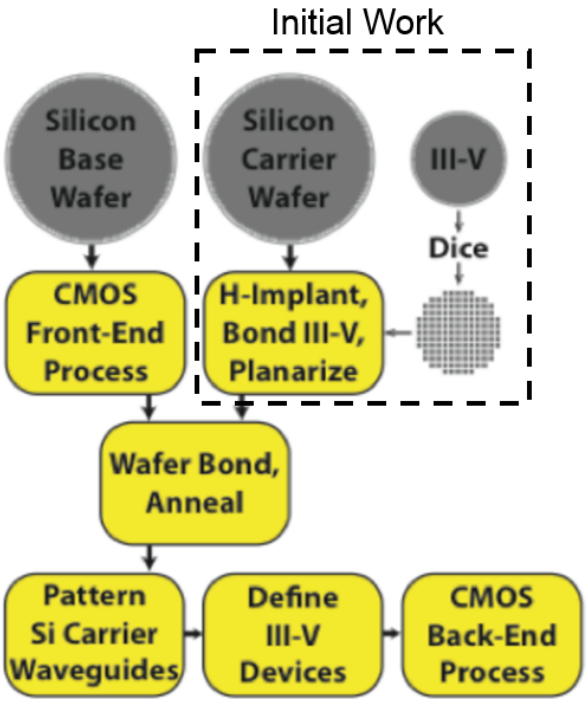

Figure 5.2 Process flow for heterogeneous integration of electronic-photonic circuitry, showing this initial work of setting up the epitaxial layout boxed in black. Graphic courtesy of Professor John M. Dallesasse, 2016.

considered. Utilizing standard cleanroom spinners, the temporary bonding polymer is able to be spun onto any surface at a speed between 3000 and 5000 rotations per minute (RPM) for 60 sec. This assures that the polymer is evenly distributed and allows for a clean bond between any cleaved III-V piece and the silicon carrier wafer underneath. The process of reversible bonding proceeds by spinning on a relatively thin (5-8 μm) coating, arranging the III-V epitaxial structures as an initial grid on top of the silicon carrier, and then finally vacuum-oven curing the temporary bonds to assure a strong adhesion. The polymer is known to be thermally sensitive in that it releases above 300º C, so the III-V-on-Si material is cured at 250º C inside the vacuum oven for 3 hours with a large weight pressing it down to assure good adhesion forces. This preparation of the III-V-on-Si acts as the first constraint on the feasibility of designing scalable electronic-photonic circuitry layouts, as shown in Figure 5.2, where the bonding of the III-V epitaxial structures onto the silicon carrier wafer enables a heterogeneous layout and so the choice and use of the bonding polymer is crucial in that.

Yet following the initial reversible bond by use of the polymer, a series of investigations must follow to confirm the efficacy in large-scale fabrication processes. In particular, it is understood that the polymer can maintain a temporary bond during flip-chip bonding, but for this particular process it must be determined if it can reliably hold throughout cleanroom-based deposition and etching processes, as well as if the III-V epitaxial pieces above the polymer can remain rigid and not prone to stress-based cracking.

5.2.2 Processing Steps

Upon uniting bulk III-V epitaxial structures onto silicon, a series of photonic device processing steps ready the material for epitaxial transfer. Shown in Figure 5.3a through Figure 5.3g, the making of III-V “islands” is shown.

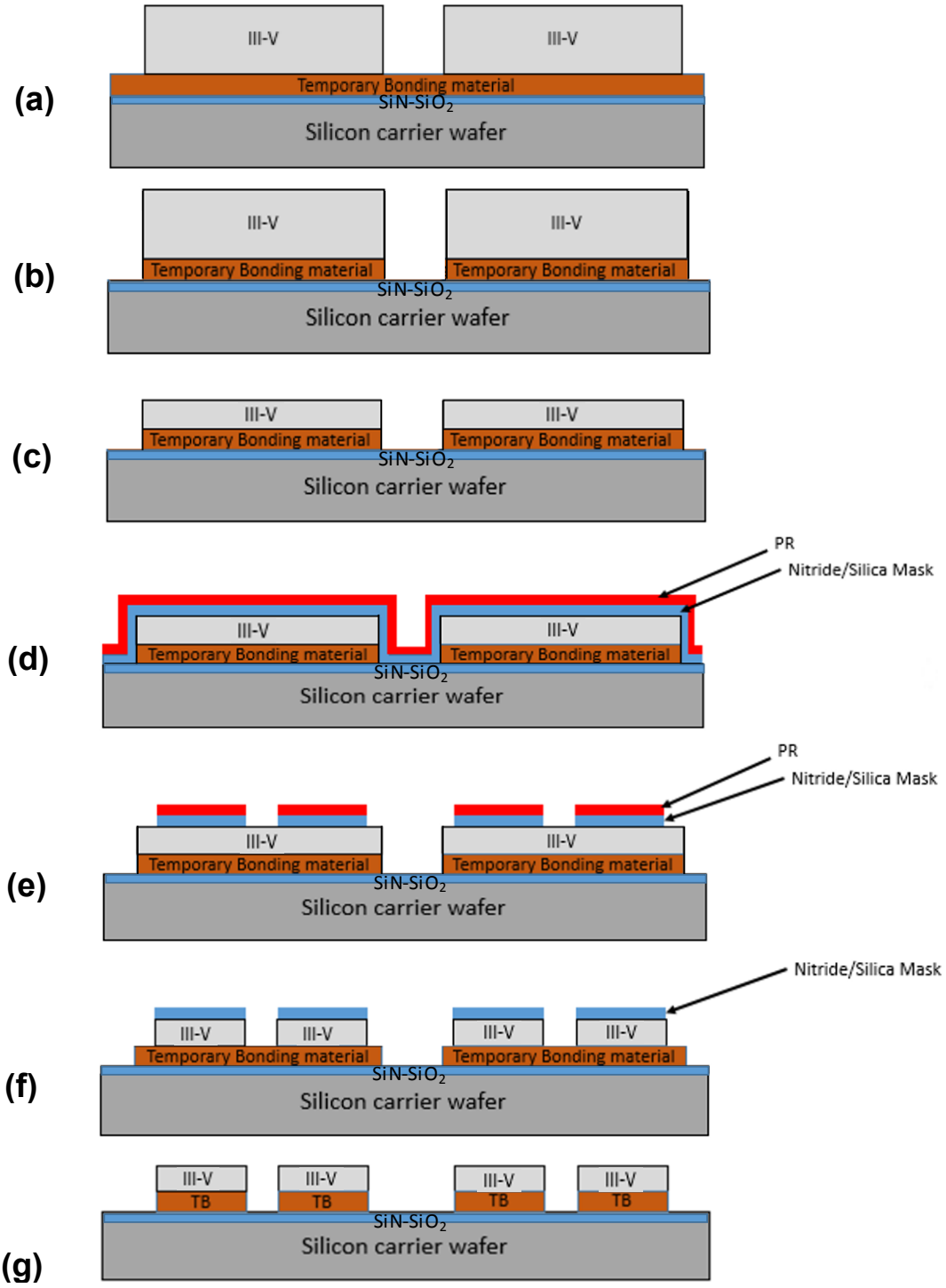

Figure 5.3 Schematic of processing steps for III-V-on-Si heterogeneous integration. A layer of SiN-SiO_2 is deposited on the silicon carrier wafer followed by a spin-on of temporary bonding polymer and a layout of III-V pieces in (a). The excess polymer is then etched away in (b) and the III-V pieces are thinned in (c). A hard mask of SiO_2 or SiN is then deposited on the III-V pieces in (d), followed by a spun-on photoresist for III-V island definition. An initial etch is performed to remove excess hard mask in (e) so that the III-V islands can be formed. A final III-V etch in (f) then defines the III-V islands, with the excess polymer again removed in (g).

As can be seen in the figures, a series of processing techniques is investigated and optimized such that bulk III-V epitaxial structures can be reduced to sizes on the order of photonic devices. The resulting structures, denoted as III-V islands as shown in Figure 5.3f, are prepared such that they span the silicon carrier wafer and can therefore align with corresponding features on a CMOS host wafer post-bonding. The intent is that these III-V islands can be made out of differing III-V alloys ranging from semiconductors used for active components to semiconductors used for passive guiding, allowing for a dense layout of distinct III-V structures that can be structured. Bulk removal of the excess III-V substrate as in Figure 5.3c is planned such that only the epitaxial layers remain above the polymer bonding layer.

Performing these steps requires consideration of both scalability and process generality across III-V alloys. As such, each step in the "recipe" is prepared iteratively over numerous III-V-on-Si layouts, useful for discerning which process variations produce good bonding and wafer integrity. These process variations are considered.

5.3 RECIPE OPTIMIZATION AND RESULTS

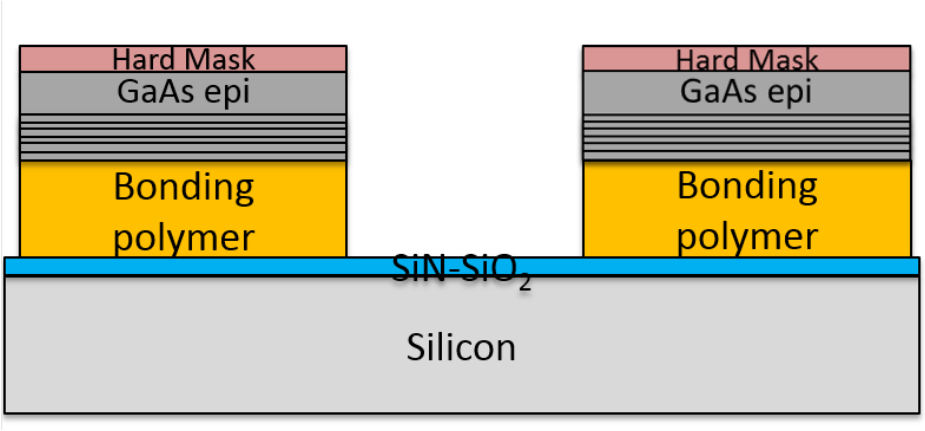

Figure 5.4 Final III-V-on-Si layout for epitaxial transfer onto CMOS.

The individual steps for each part of the processing are described. Each step is considered initially and then optimized per later findings for preparing the III-V epitaxial structures into III-V islands ready for flip-chip bonding onto CMOS, as shown in Figure 5.4, as the desired final stage of this process. By iteratively constructing a robust process for heterogeneous integration, the final epitaxial layer structure can be transferred onto aligning electronic structures followed by the removal of the temporary bonding polymer chemically or mechanically.

5.3.1 III-V-on-Si Polymer Bonding

The heterogeneous integration process begins with the spin-on application of the polymer. In this, the 2" silicon carrier wafer is placed on the spinner as is and a liberal amount of the temporary bonding polymer is applied to the wafer. Noting the polymer acts as an adhesive, the process must quickly proceed, so an initial speed is chosen at 3000 RPM for 30 seconds. This produces an even coating of the polymer of roughly 8 μm, conformally covering the entire wafer as shown in Figure 5.5a. Fringe-patterns confirm the coating's relative thinness while a high-resolution mechanical micrometer is employed to confirm the thickness of the layer. This tool works by dragging a mechanical

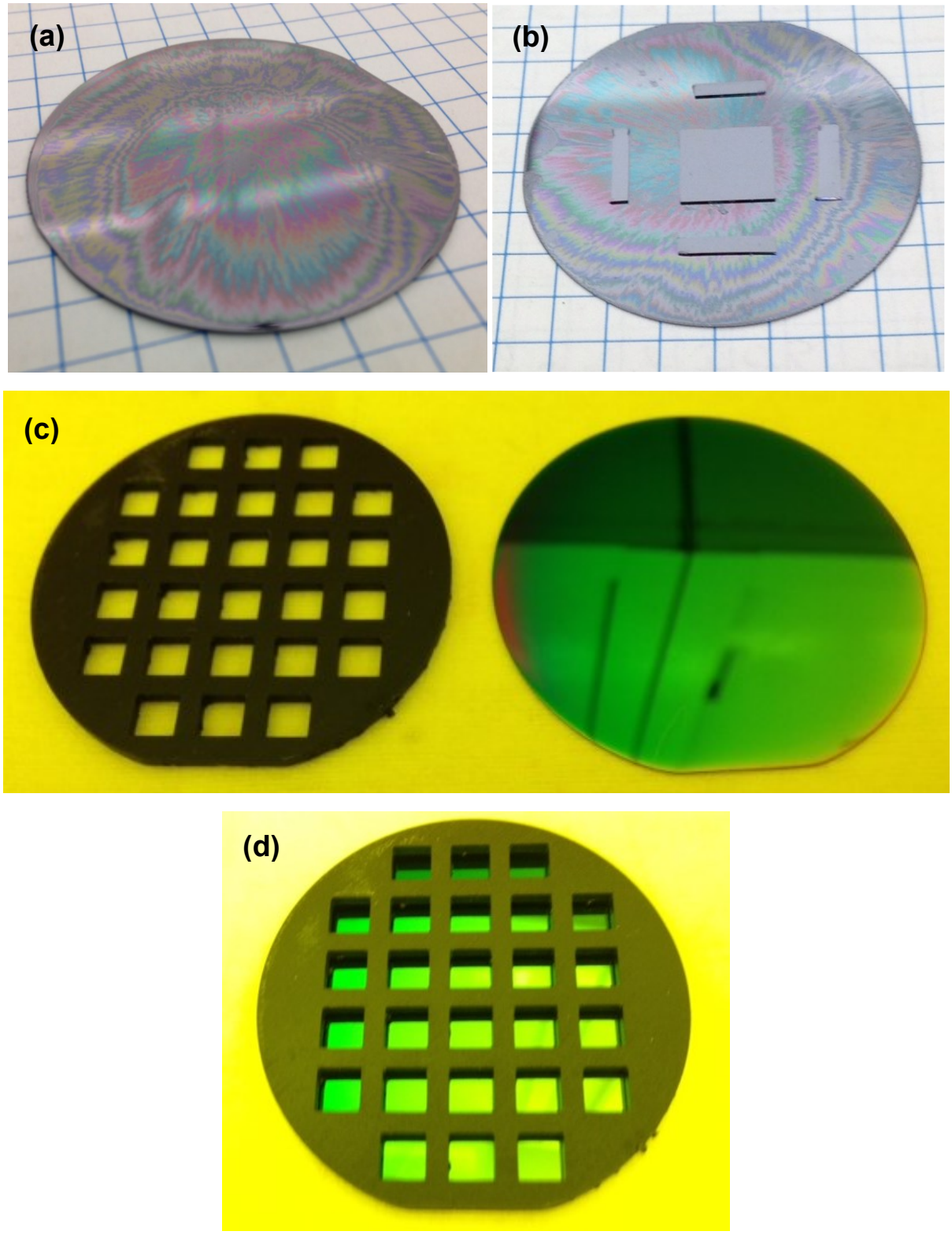

Figure 5.5 Processing results after spin-on application of temporary bonding polymer in (a). The initial layout of III-V pieces on the polymer for temporary bonding, confirming strong adhesion in (b). An SLA-printed stencil is made to allow for a grid-like layout of III-V pieces for temporary bonding in (c), allowing for a manual alignment in (d) of III-V pieces atop the polymer. The addition of an SiN-SiO_2 layer for stress relief is visible.

point across the surface of any semiconductor or polymer interface, producing a delta-step that is used to determine a material thickness. The initial proof-of-concept tests consist of placing large GaAs pieces around the silicon carrier wafer as shown in Figure 5.5b, including a set of "runner" pieces along the sides to assure even thinning of bulk semiconductor as described in Chapter 5.3c. These pieces are placed in a vacuum oven preset to 250º C as previously described, and following their removal an initial shear test is performed with a cleanroom scalpel on each bonded III-V piece. With good adhesion over the extended surface, this confirms the first stage of the epitaxial transfer process.

Following further considerations throughout the process findings, a series of adjustments are then made to the initial spin-on coating of the polymer for more optimal results. Initial results following thinning and hard mask deposition (Chapter 5.3c, 5.3d) find that an exceptional amount of stress exists at the polymer-GaAs interface, caused by the rigidity of the polymer as compared to the GaAs. As such, micro-cracks form in the GaAs material sooner than expected, a potential issue for later device formation as this effects α_i in cavity threshold, so a series of investigations are performed to remedy this. The result is a decision to first deposit a thin-film growth of SiN-SiO_2 on the silicon carrier wafer using a plasma-enhanced chemical vapor deposition (PECVD) tool, consisting of 250 nm SiO_2 and 250 nm SiN on top. Noting the effect SiN has on relieving surface stress, this process allows for the polymer deposition on top to better conform to the GaAs and not buckle under stress.

A stencil is prepared to allow for more consistent distribution of III-V epitaxial structures across the silicon carrier wafer, where the stencil is stereolithographically (SLA) printed and placed atop the silicon carrier wafer for GaAs piece alignment just after the spin-on application of the polymer. This effect is shown in Figure 5.5b and Figure 5.5c, where it is seen that this stencil lays out the III-V materials in an orderly fashion.

5.3.2 Removal of Excess Polymer

The next step undertaken in optimizing a heterogeneous integration process involves the removal of excess polymer on the silicon carrier wafer. While straightforward in intent, the proprietary nature of the temporary bonding polymer requires a search for the proper etch such that the excess polymer can be removed and does not react. An initial series of etches is performed on silicon carrier wafers with spun-on polymer without any III-V piece distribution on top. In these, the first consideration is to utilize fluorine-based chemistry as part of a dry-etch, where the fluorine species is contained in either CHF_3 or CF_4 and chemically reacts with the polymer to produce a vapor waste that is removed from the chamber. A second chemical species of O_2 is added to the chamber to chemically react with any additional organic residue. This process occurs inside a reactive ion etch (RIE) chamber, capable of vacuum levels down to 10^{-7} Torr, where a capacitive-based field emerges between the RIE plates and strikes the gases to produce a volatile plasma.

Initial findings, however, show that this particular combination of plasma species does not remove the bulk of the polymer and instead reacts to form an opaque film across the silicon carrier wafers. An initial choice of RIE power of 200 W paired with the reactant species consistently produced the same results. Considerable work followed this revelation in order to focus in on what specifically was causing the reaction to produce adverse results, especially considering that the opaque film was permanent on the silicon carrier wafers. Eventual discussion determined that this mixture of chemical reactants containing fluorine-based chemistry was producing a Teflon-based substance (i.e C_2F_4)

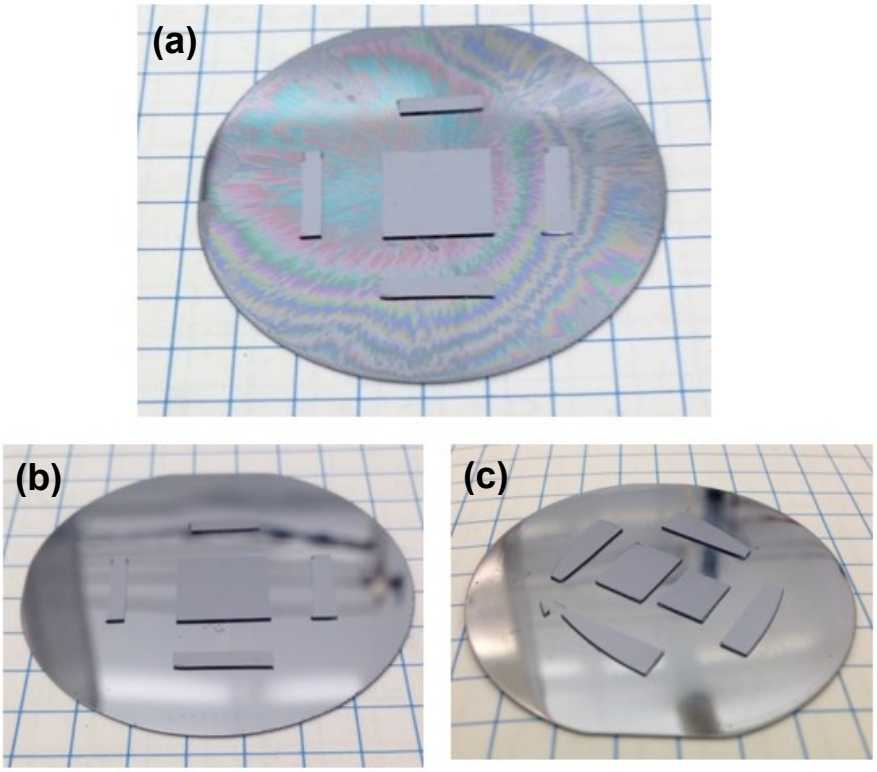

Figure 5.6 Early processing results before the removal of the polymer (a) and after the removal (b,c). It is seen that the bulk substrate of the silicon wafer is visible.

across the silicon carrier wafers upon reaction with the organic materials in the temporary bonding polymer, which as the name would lead one to believe is fairly irremovable. To this finding, the fluorine-based gases were removed entirely from the chamber and substituted in was inert argon gas, which instead of chemical etching would produce physical etching whereby it aids the process through physical bombardment. Upon this change, the production of the Teflon-based film was halted though the polymer remained unperturbed, so the inclusion of an inductively-coupled plasma (ICP) effect inside the chamber was employed. This ICP effect, as produced by a copper coil that surrounds the RIE plates, produces a strong magnetic field within the coil's span and greatly enhances the plasma density for etching. Following this change, positive results were achieved, allowing for the bulk removal of the temporary bonding polymer without adverse reactions. Figure 5.6 shows the results from this optimized process, where in Figure 5.6a the wafer is shown before the excess polymer removal and in Figure 5.6b and Figure 5.6c the polymer is removed.

A final set of optimizations is then later implemented for the excess bulk removal process, following later processing findings. Owing to the fact that the first successful polymer removal recipe is high pressure to assure rapid removal, this high pressure effect causes a more isotropic etch that begins to undercut the III-V epitaxial structure pieces. This means that polymer underneath the remaining pieces is etched as well, reducing the adhesion of the eventual III-V islands as shown in Figure 5.3f. To correct for this, a correction to the recipe is pursued to assure that the etch remains anisotropic and as vertical as possible. The correction to the recipe consists of a reduction of the chamber pressure from 70 mTorr to 10 mTorr, where low-pressure recipes are known to be anisotropic. Since this is expected to reduce the etch rate of the bulk polymer, the ICP power is therefore changed from 300 W to 600 W,

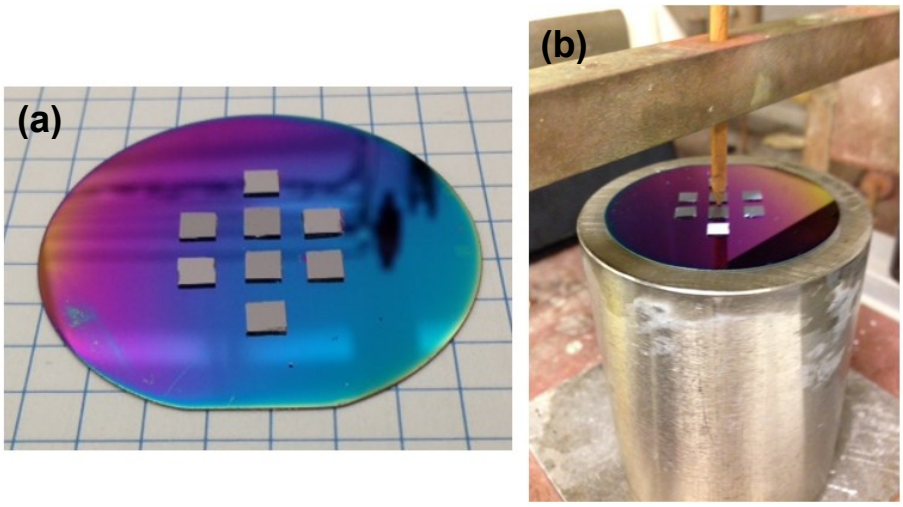

Figure 5.7 Optimized results of excess polymer removal in (a) and its mounting on a chuck for thinning in (b).

assuring that a rapid scalable etching process is maintained. Figure 5.7a shows the final bulk removal results, where the addition of the SiN-SiO_2 stress relief layer is now clearly visible, and in Figure 5.7b the wafer is shown being readied for the next stage for bulk thinning.

5.3.3 Lapping and Polishing for Wafer Thinning

The next stage of the process allows for the III-V epitaxial pieces to have their bulk substrate thinned away in unison such that only their epitaxial layers remain. To do this, the technique of lapping and polishing is considered and optimized for this heterogeneous material process. Borrowing from silicon manufacturing, the chemo-mechanical polishing (CMP) process allows for a bulk semiconductor to be reliably thinned down using large-scale processing tools. This technique is investigated for the extensive case here, where each III-V epitaxial structure layout on the silicon carrier wafer should be thinned down from roughly 350 μm to no more than 10 μm.

After mounting each 2" wafer onto a large lapping "chuck" by use of a thermally-sensitive wax and allowing it to set in place for a good even hold (as shown in Figure 5.7b), each III-V-on-Si grid is prepared for CMP processing. The lapping chuck is enclosed inside a large polishing block (Figure 5.8a) and the III-V wafers are then placed directly onto a series of blocks that each cause even III-V semiconductor removal on top of the silicon carrier wafer. This process, though done in a manual fashion at present, mimics that of the large-scale industrial processes, so all work derived here can be expected to easily be extended for scalable processing. The III-V wafers are first used on a rough, frosted glass plate whose serrations act to trap a 9 μm alumina grit powder as shown in Figure 5.8b; when the polishing block is rotated in a cyclical pattern (i.e figure-eight) on the block, the grit powder effectively mulls off the III-V semiconductor in a reliable manner. Roughly every 100 firm figure-eights remove around 50-70 μm of bulk GaAs semiconductor, as found. Thus, this process is adjusted to assure that the bulk removal does not proceed too quickly and that the removal is not too coarse. Early returns from this lapping process found that too rapid lapping causes the GaAs pieces to buckle and break along the polymer, so a slower pattern accompanied by better stress-relief and less etching undercut underneath the polymer is employed, as described in Chapter 5.3a and Chapter 5.3b. Together, the bulk removal becomes apparent. Once bulk removal has been achieved, the III-V pieces are extensively cleaned with

Alconox powder and then placed directly on a softer white block, where a finer set of grits stepping down from 0.3 to 0.06 μm allows for all the pieces to be smoothed in unison as shown in Figure 5.8c. This process allows for the remaining epitaxial material to be left with a smooth interface, where the finer grit assures no bulk removal. After 200 more firm figure-eights or so per grit, the final step in thinning the III-V materials returns them to their ideal polished semiconductor state, where it is known a polished interface implies better reflection for later photonic devices. This final step, as depicted in Figure 5.8d, takes the smoothed III-V pieces along the silicon carrier wafer and puts them into contact with a sponge-like block that is doused in diluted household bleach. Acting as an oxidizer for III-V materials, this bleach works to oxidize the surface of the smoothed GaAs pieces into a characteristic black look. This oxidized surface is then rotated against the sponge-like block, causing agitation that removes it leaving a nicely polished semiconductor interface, as shown in Figure 5.9.

A final consideration for bulk semiconductor removal involves the use of wet chemical etching solutions. A series of wet-chemical solutions are prepared and tested to produce reliable etching of the III-V pieces. Noting that each III-V has a different sensitivity to wet chemical etchants, GaAs is found to be sensitive to both phosphoric acid (H_3PO_4) and sulfuric acid (H_2SO_4) as etchants. In both, a solution is carefully prepared whereby acid, hydrogen peroxide (H_2O_2), and water are mixed to produce a particular etching rate. Again, this chemical process is much like CMP in its polishing attributes, where the peroxide oxidizes the surface of the GaAs and the acid removes the oxide for a strong interface. From each of these findings, it is seen that a solution on the order of 1:1:5 (acid:peroxide:water) produces an etching rate of 1 μm/min of the GaAs, though it is also seen that the sulfuric acid mixture is more

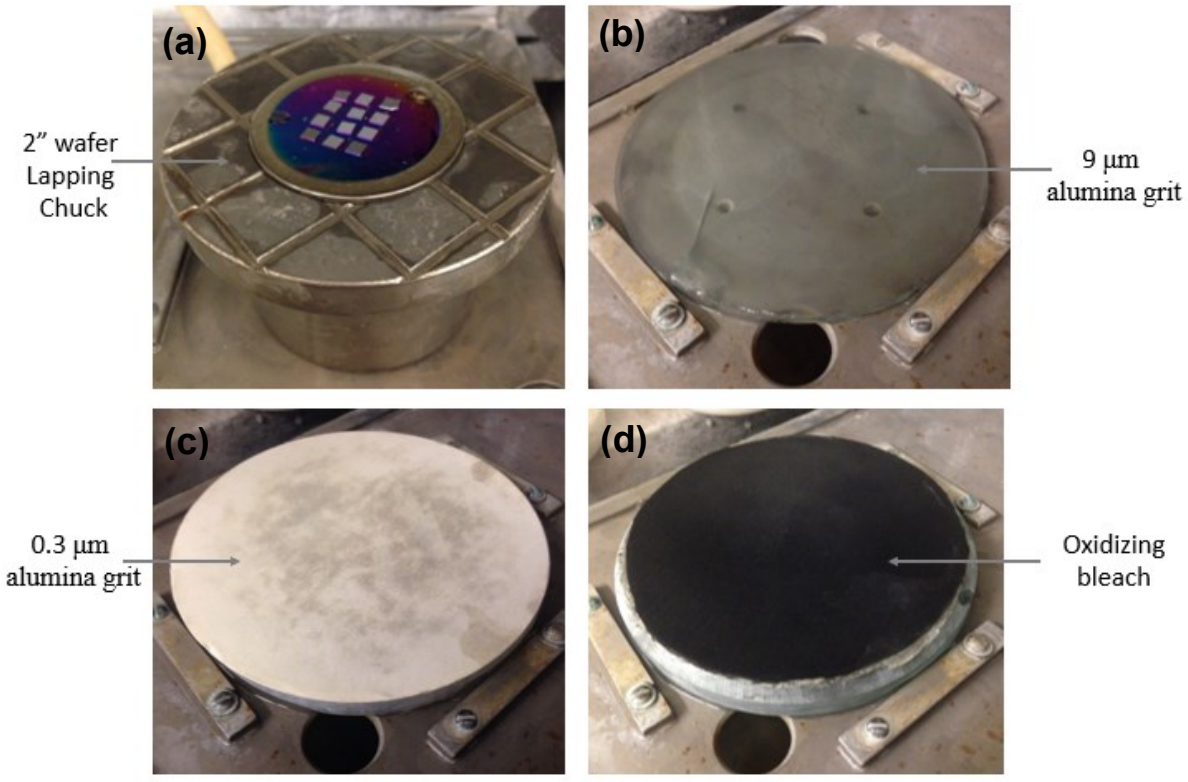

Figure 5.8 Lapping chuck designed for 2" silicon carrier wafers in (a). The thinning process proceeds first on a lapping block in (b), then by a fine grit alumina powder in (c), and finally an oxidizing bleach to polish in (d).

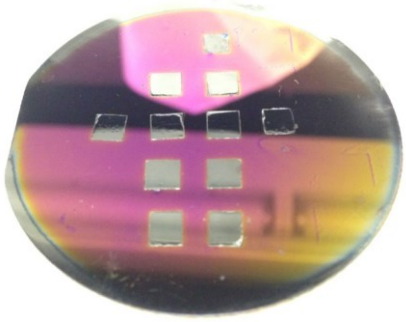

Figure 5.9 Fully thinned GaAs epitaxial structures atop Si, where the polymer is shown to adhere well.

anisotropic and thus removes disproportionately along certain crystalline axes, implying that small microcracks in the materials will quickly give way to large unwanted removal. As such, the phosphoric acid mixture is chosen, given that it is more isotropic, and the solution is employed at the last stage of the bulk removal to assure that no more than 10 μm remain of GaAs. Further work will utilize fully-formed epitaxial layer structures, so it is expected that the use of a wet etchant will be even more straightforward, given that they can be tailored to work until hitting an "etch stop" material, implying that a particularly thin layer can be preserved on the basis of its chemical sensitivity.

5.3.4 III-V Island Definition

The preparation of the III-V islands requires that a method is used to selectively define areas for processing. From this principle, photolithography and hard mask development are used, as shown in Figure 5.3d and Figure 5.3e. For this, the III-V epitaxial structures are therefore prepared with a hard mask made of SiO_2, given SiO_2's strong selectivity in later III-V material etching. The hard mask will act as a means to selectively pattern and cover portions of the III-V epitaxial structures such that when they undergo III-V etching they only etch away material where the hard mask is not present. To then prepare this mask, initial considerations are given to the III-V-on-Si structure, noting the temporary bonding polymer's thermal sensitivity above 300º C. A specific recipe is therefore developed that allows for the formation of an SiO_2 hard mask at a temperature of 250º C. Similar to before with the SiN-SiO2 stress-relieving layer underneath the polymer, the SiO_2 hard mask is deposited by use of the PECVD tool, where silane (SiH_4) and nitrous oxide (N_2O) gases are allowed into a vacuumed chamber and a series of adduction and desorption processes follow, where the products of the reaction produce solid SiO_2 on the surface of the III-V and silicon carrier wafer while outgassing any waste products. The hard mask is therefore produced across the GaAs pieces for good III-V island definition, and the relative thickness of the material is calibrated to produce 1 μm, determined by checking a color chart where the interference patterns of the SiO_2 expectedly produce a green-purple layer at 1 μm.

To define the hard mask for good selective etching of the GaAs material underneath, the process of photolithography is employed. Using a set of organic polymer-based photoresist (PR) fluids, photolithography allows

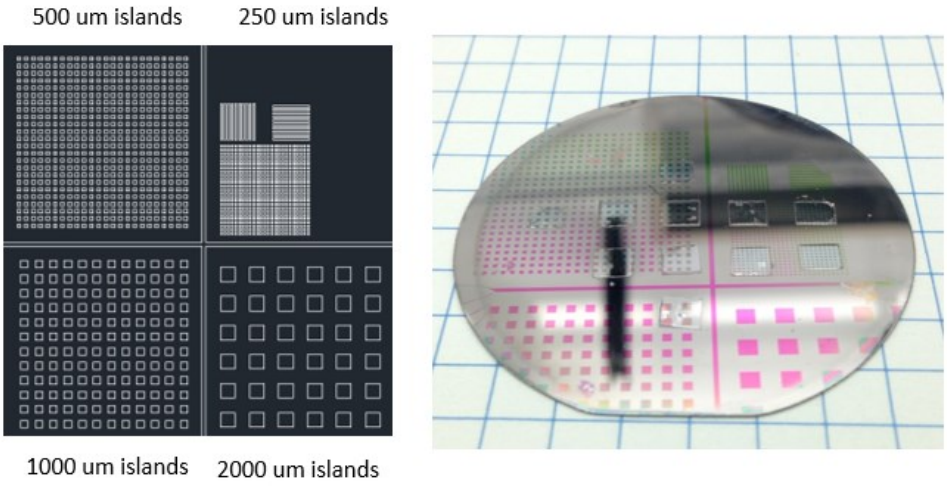

Figure 5.10 Lithography pattern for heterogeneous III-V island definition, shown on thinned GaAs pieces.

for the spin-on application of a second mask that is light-sensitive such that it can be exposed underneath a short-wavelength UV lamp to chemically alter the polymer for selective removal. The polymer used is a positive resist (S1813) where it is spun-on at 3000 rpm, allowed to soft bake, and is then exposed underneath a prepared lithography mask. This mask shown in Figure 5.10, as developed in Inventor, is constructed as a light-field mask for the development of the III-V islands, where each enclosed square shown is patterned out of chrome to prevent UV light from reaching underneath to that PR, ensuring that the remaining PR is UV-chemically reacted. Varying in dimensions, the III-V islands are progressively made smaller to the point of being on the order of typical edge-emitting laser designs at 250 μm. Following this exposure, the entire III-V-on-Si wafer is moved to a basic (pH > 7.0) developer bath, where the developer is sloshed over the PR features, removing only the UV-chemically reacted excess PR and leaving well defined islands of PR above the uniform hard mask, as shown above in Figure 5.10.

Following development, the selectively-defined PR is then used to produce the same features in the hard mask. The intent here is to fully remove all excess hard mask where not desired, such that the GaAs material is openly exposed there for III-V etching. Using fluorine chemistry inside an RIE tool, a series of etch tests is thus performed to determine a proper etching recipe of removing SiO_2, where the tradeoffs noted are that too aggressive an etch will remove the PR mask prematurely while too subtle an etch will take too long and potentially expose the temporary bonding polymer to excessive plasma heat sources and over-cure it. A series of etch rate tests is performed for a CHF_3/O_2 plasma combination using dummy GaAs pieces coated in the same hard mask and same lithographic patterns, shown in Figure 5.11. It is seen that varying the total amount of O_2 flow rate (sccm) relative to the CHF3 in a constant 30 sccm flow changes the overall etch rate; noting that O_2 is more isotropic in etching than CHF3, it is seen that the highest O_2 percentage (86/14, CHF_3/O_2) begins to drift significantly in etch rate, implying that some irregularity related to thermal sensitivity or material selectivity is present. As such, a higher CHF_3 relative percentage to O_2 is chosen, allowing for good anisotropy in the etch which leads to strong hard mask sidewalls. This etch is then performed inside the RIE tool to allow for a good removal of the excess hard mask everywhere outside of the PR islands.

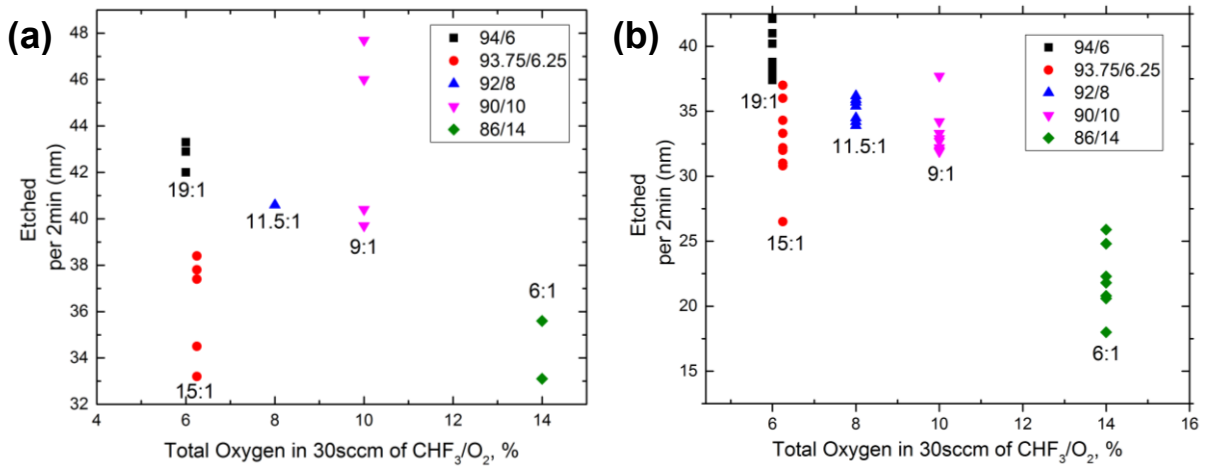

Figure 5.11 Hard mask etch rate over CHF_3/O_2 flow rate ratios, shown at (a) 2 minutes and (b) 4 minutes for a constant total of 30 sccm. Each individual dummy piece used in the testing is shown by a single point.

Following these initials steps, a few optimizations take place to assure that the process is refined. The initial PECVD of the hard mask takes place in a slower chemical environment, requiring the wafer to be exposed to plasma for over 40 minutes to achieve a hard mask deposition of 1 µm. Noting the concern of overexposure of the polymer to plasma heat, the process is therefore updated so that it can be performed in under 12 minutes with comparable conformity, assuring that the process remains scalable. Additional optimization is found in the final etching process of the hard mask, where the wafer is transitioned into a chamber that is capable of both ICP and RIE processes. Still using the same reacting gases, the higher power possible with the ICP assures that the process etches through 1 µm of hard mask rapidly, going from near 1 hour of etching to under 3 minutes of etching; upon this transition, the results are compared and they look comparable, where the ICP-RIE environment is favorable to the thermal sensitivity of the bonding polymer.

5.3.5 III-V Etch

The final stage of this work in heterogeneous material integration involves the formation and definition of III-V islands. To do this, a chlorine-based chemistry inside of an ICP-RIE equipped etching chamber is used. In this, the chlorine species of silicon tetrachloride ($SiCl_4$), combined with the physical etchant argon, is used to etch away the exposed GaAs (i.e. not covered by hard mask) in a controlled fashion at low pressure, where etch rates on the order of 500-900 nm/min are possible. The hard mask blocks the GaAs underneath itself and etches much slower than the surrounding GaAs, with a selectivity between GaAs and SiO_2 found to be roughly at 20:1. A set of wafers prepared for the III-V etch is shown in Figure 5.12, where it is seen that the III-V islands on the order of typical photonic devices are now surrounded by excess GaAs. Given that the depths of this III-V epitaxial structure exceed most depths associated with III-V etching, the recipe devised must take this into account such that the III-V material does not burn or unevenly etch due to the excessive depths required.

The prepared recipe undergoes a considerable amount of optimization, where it is found that too low pressure in the chamber (<2 mTorr) will not strike the plasma, so a series of steps toward low pressure are prepared to take the

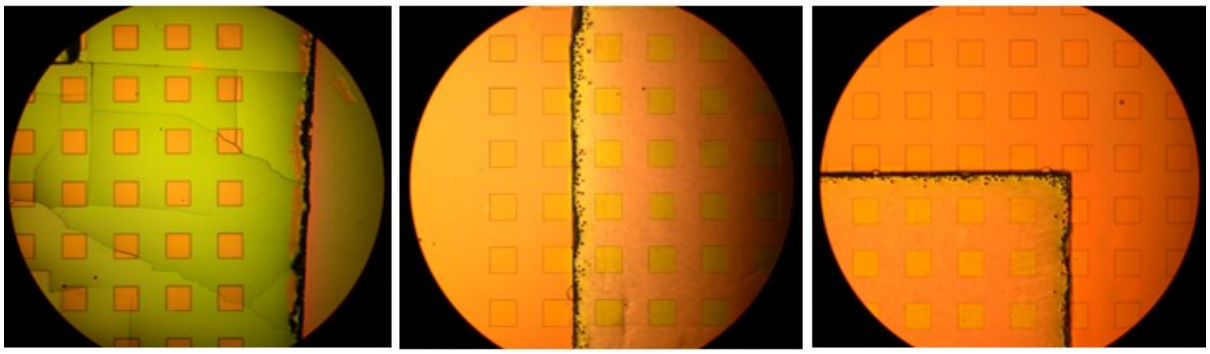

Figure 5.12 III-V island hard mask distribution (250 μm x 250 μm squares) on GaAs wafer ready for III-V etching, where the edge of the thinned GaAs piece is seen on top of the silicon carrier wafer underneath.

chamber down to an appropriate level. The thermal sensitivity of the temporary bonding polymer requires that all thermal accruement incurred by the plasma is allowed to conduct away, requiring that the silicon carrier wafer be rigidly waxed onto the chamber platen so that heat can propagate away from the hard mask and III-V materials. Additionally, noting that the bonding polymer is sensitive to excessive thermal sources, the etching recipe is adjusted to a higher ICP power, doubling to 200W, allowing for rapid removal of excess GaAs at an etch rate of roughly 850 nm/min. With this rate, the total etching process takes 10-15 minutes, greatly reducing the etch time from before when the etching would occasionally run towards 1 hour due to the considerable amount of GaAs.

It is seen that the III-V islands can be formed by etching through the GaAs material, where the hard mask allows for good selectivity and thus allows for deep etching. This deep etching prepares a series of pillars atop the temporary bonding polymer that span the silicon carrier wafer, removing the excess material and allowing for a grid of III-V materials that are capable of electronic-photonic integration.

The next steps in this process will proceed to finalize the removal of the excess temporary bonding polymer and to test the shear force strength of the remaining III-V islands. In this, early determinations can be made regarding the integrity of GaAs pieces as they are flip-chip bonded onto silicon in a large-scale array. From these determinations, the same process can be extended to other III-As alloys, as well as to III-N materials that can enable a full range of active and passive devices.

5.4 DISCUSSION

Together, these steps present a complete process for taking bulk III-V epitaxial wafers and readying them for permanent adhesion onto CMOS wafers, enabling the heterogeneous integration of electronic-photonic devices. This work looks at GaAs and determines a method for temporarily bonding this material on an intermediary silicon carrier wafer for initial processing, producing a large arrangement of III-V islands that can be bonded in unison onto fine-aligning features on CMOS. As such, this process provides a substantial step forward in realizing the difficult task of uniting a range of III-V photonic materials for coupling and routing structures. It is seen by use of GaAs epitaxial structures that the temporary bond strength throughout this process remains strong and thus able to be scaled up. Furthermore, the various techniques employed in this process have been found to proceed quite rapidly together,

owing to the fact that each can leverage standard CMOS fabrication processing tools with only small optimizations needed to account for III-V alloy variations.

Looking past this initial work, the III-V-on-Si process now has a scalable method for photonic material distribution that can be planned and lithographically defined in a repeatable manner. Once a large array of III-V islands are readied, their bonding onto aligning CMOS features will require investigation into permanent bonding processes. Likely using metal contacts or a separate dielectric, the annealing of these bonds will provide for a robust connection between III-V and silicon. Following this, the temporary bonding polymer now on top of the III-V pieces can be removed by chemical or mechanical slide means, revealing the epitaxial layers of the III-V islands. From these, final etching processes can be performed in unison across the III-V islands, allowing for lasers, photodetectors, modulators, photonic control devices, or various sensing devices to be formed and coupled together with fine sub-micron precision. This process directly allows for this precision, as any technique of device formation before final bonding would be subject to manual alignment variation; instead, here the III-V island retains generality until it is finally flip-chip bonded and then made to easily be formed into recognizable devices. Each step progressively refines the III-V material, allowing for considerable flexibility in device planning, a considerable advantage in laying out and planning electronic-photonic integrated circuits.

CHAPTER 6: CONCLUSION

"Almost in the beginning was curiosity."
-Isaac Asimov, 1987

Together, the components of this research thesis point to promising methods for integrating electronic and photonic devices. A broad set of parameters detailing the characterization, simulation, fabrication, testing, and analysis of CMOS compatible photonic structures is considered and discussed.

It is found that the use of an integrated spectrometer based on a CMOS-compatible LVF sensor can enable a compact sensing system capable of biochemical-related analyses. The set of steps followed produces a series of results that present how to unite heterogeneous materials onto CMOS, enable signal collection and signal processing via the LVF, test and compare the system on realistic point-of-use assay tests, and to compress the entire set of optical and electrical components down into a manageable, scalable framework. This sensing device is compact to the point of being directly attachable to CMOS while its resolution and spectral range produce spectra that are comparable to standard handheld spectrometers. This puts the full operation of sensing small-signal stimuli in biological or chemical systems to be within the reach of photonic systems, all by the virtue of closely aligning electronic and photonic components. The importance of sensing the absorptive or fluorescent signature of a particular assay or contaminant cannot be understated, and again given the nature of integration being the main limiting factor, a method for making an integrated spectrometer usable on a smartphone platform is shown to be a novel step forward in scaling access to biochemical-related photonic processes.

Further, the study of GaN and its III-N alloys sets the background for the design and simulation of a unified laser structure that can enable a low-power, rapid, integrable strategy for cavity-based wavelength tuning. This work produced results that explain how to understand the dynamic lattice displacement of GaN, relate the material parameters of GaN to a desired index change, produce a set of geometries capable of wide-band tuning, lay out a CMOS-compatible design, use a static field to cause controllable tuning, and to design integrable laser structures that can input electronic controls and output a photonic signal for DWDM. This set of laser designs allows for a closely-aligned device footprint where electronic drive circuitry is directly attached atop a GaN waveguide that is integrated into a standard telecom-wavelength InGaAsP QW design. A single laser can then be used to produce a range of wavelength tuning without adding to the system current nor taking away from the gains in speed possible with an all-field control design. By this, a highly reconfigurable set of lasers can be made into a network, with a common electronic system capable of interrogating each and providing the necessary stimuli to tune to a set output wavelength. The findings answer the question as to whether GaN is a suitable material for future III-V-on-Si integration. It is seen that GaN performs remarkably well to this end due to its piezoelectric and electro-optic effects, with the added benefit of III-N alloys being readily available and customizable presently in industry.

Finally, a fabrication recipe is constructed that shows how III-V epitaxial structures can be laid out and distributed onto silicon for large-scale processing and interconnect distribution of electronic-photonic circuitry schematics. The experiments performed investigate how to define and bond initial III-V structures atop a silicon

carrier wafer and then ready these initial features for transfer onto CMOS-grade silicon for a single heterogeneous layout of III-V-on-Si. These techniques are designed and implemented so that rough alignment of III-V materials is sufficient for initial defining of possible photonic devices atop the carrier wafer, enabling a more scalable approach to system design that holds off sub-micron precision until final processing. Utilizing a heterogeneous platform from the start—III-V epitaxial layers prepared and processed on silicon—produces a simple design in laying out a scalable mesh of electronic and photonic connections and control for direct integration on a single CMOS wafer. These results are founded on a series of cleanroom-based procedures that show how to convert bulk GaAs via fluorine and chlorine chemistry dry-etch techniques into a series of thin-film features that are directly readied on a silicon carrier wafer. By investigating how temporary bonding polymers work in semiconductor processing, a complete recipe is designed and optimized that can be extended to any III-V wafer for direct integration onto silicon where it is then thinned, polished, defined, and etched for dense device placement. A process flow and a deep understanding of standard cleanroom equipment emerges so that individual III-V wafers capable of photonic device fabrication can be prepared for pick-and-place alignment onto a pre-processed (back-end) CMOS wafer, allowing for a single electronic-photonic system to be constructed in unsion. By this, the process designed answers the questions of the previous sections by now considering fabrication constraints for heterogeneous layouts and beginning the process of integrating electronic-photonic networks.

6.1 BROADER IMPACT

These results separately present strategies to achieve the goal of making photonic devices see the same scalability and versatility as standard CMOS electronic systems. They make up a compact sensing platform composed of integrating graded DBR as an LVF atop CMOS electronics capable of wide-band spectroscopy, a novel method for laser cavity tuning based on GaN-based anisotropies that creates tunable mirrors via index shifts for telecom materials, and a scalable strategy for physical integration of III-V epitaxial wafers onto a common silicon carrier wafer for batch processing and bonding. Yet it is also recognized that the culmination of these results presents a common design toward dense structures capable of electronic-photonic controls for electronic-photonic signals, where the heterogeneous integration of III-V devices and other dielectrics, allowing for photonic interactions and signal routing, with silicon CMOS, optimized for transistorized memory and logic controls, lays out a closely intersecting system. Given the constraints on expanding electronic-only systems further as they relate to data infrastructures, the ability to unite such photonic and electronic domains seamlessly is a crucial goal for further semiconductor-based integration strategies. As such, the methods and designs derived herein present a potential unified path forward to this inevitable transition to broader photonic implementation in present electronic layouts.

It is reasonable to expect that all systems fully embracing photonics and its capabilities would seek to assure that sensing, emission, and the close integration with any needed electronics work in tandem. Such a network would therefore require means of resolving and distributing relevant optical signals that are incident onto a photosensitive device. Given the inherent advantage possible with photonic systems and its wide spectrum, multiple wavelengths carrying either information or reconfigurable controls can be routed and used simultaneously, allowing for different devices to perform tasks. If sensing a desired signal or external stimuli is therefore a crucial starting point before a

reconfigured control is chosen, the LVF design and its direct integration onto CMOS image sensors can be embedded to resolve the relevant wavelength of the passing signal, similar to large scale prisms and diffraction gratings. It is worth remembering that the majority of the LVF device used in this work was bulk dielectric for mechanical stability, whereas the passive sensing section is constrained to the top thin-film. This same network would therefore require means of rapid, efficient tuning of optical signals capable of in-plane routing. The set of GaN-based laser cavity devices, as described, that emits at telecom wavelengths would match to this goal well, allowing for DWDM at the source given the ability to vary index. Further, the close interplay of this cavity effect with the low-dissipation electric fields applied to it means that a closely tethered electronic system would be in the interest of such a network. Able to leverage the advantages presently held by CMOS technologies in cost and scale, the GaN design discussed can be reconfigurably controlled via its matched static/RF electronic system for rapid variations to tune or stabilize a desired wavelength, thus assuring a system's scalability beyond single device dies. With a stable set of sensing and emitting devices, it is conceivable that multiple photonic devices can be aligned and realigned for cascading signal networks, able to be reconfigured rapidly for a particular task or instruction given the overlaid CMOS electronic device's controls. Much as electronic integrated circuitry saw the benefits and expansion due to its signal reliability across multiple configurations and functions, the same can be expected by proper alignment and distribution of these very devices for optical signals. It is here then where the ability to fabricate III-V-on-Si comes into play. The viable process found for laying out epitaxial wafers to construct interacting electronic-photonic elements can be employed to best distribute GaN-based lasers and LVF-based spectroscopic sensors, each enabled or disabled by its corresponding implementation of CMOS electronics. Additional devices and geometries that emerge and require placement within a single integrated system can thus be folded into the processing technique, where the bonding method is constructed for any or all III-V wafers to be aligned and placed as needed. A single system of electronic and photonic ready materials can then undergo patterning or dielectric deposition to further define DBR or photonic waveguides as well as metal deposition for electronic contacts, producing a final heterogeneous patterning of materials that so far presents inclusive methods of tuning and small-signal detection. With such a fundamental platform as enabled and forecasted in part by these findings, the ability for electronic-photonic circuits to reach orders of scale across applications in telecommunications, biochemical sensing, and other industry-level processes is well within reach.

6.2 NEXT STEPS

The work described in this thesis presents a possible path forward toward the industry goal of electronic-photonic integrated circuitry. Given the complexity of this goal, these efforts as completed present a single step forward toward this substantial goal and much work remains to reach scalability on the levels seen by the penetration of CMOS electronics. As such, additional photonic device experiments are to begin with the intention to scale and unify designs derived from this work as needed and with the understanding that the author remains vested in seeing to electronic-photonic integration's expansion. Each set of results and findings shows promise in isolation and so the next step is to begin work on coupling components and design techniques (i.e. simulation, fabrication) for electronic-photonic integrated circuits.

REFERENCES

[1] Bardeen, J. and W. H. Brattain (1948). "The Transistor, A Semi-Conductor Triode." Physical Review 74(2): 230-231.

[2] Hall, R. N., et al. (1962). "Coherent Light Emission From GaAs Junctions." Physical Review Letters 9(9): 366-368.

[3] Holonyak Jr., N. and S. F. Bevacqua (1962). "Coherent (Visible) Light Emission from $Ga(As_{1-x}P_x)$ Junctions." Applied Physics Letters 1(4): 82-83.

[4] Holonyak, N. (1987). "Semiconductor alloy lasers--1962." IEEE Journal of Quantum Electronics 23(6): 684-691.

[5] Noyce, R. N. (1977). "Large-scale integration: What is yet to come?" Science 195(4283): 1102-1106.

[6] Alferov, Z. I. (1998). "The history and future of semiconductor heterostructures." Semiconductors 32(1): 1-14.

[7] Pearson, G. L. and W. H. Brattain (1955). "History of Semiconductor Research." Proceedings of the IRE 43(12): 1794-1806.

[8] Tan, F., et al. (2014). "850 nm oxide-VCSEL with low relative intensity noise and 40 Gb/s error free data transmission." IEEE Photonics Technology Letters 26(3): 289-292.

[9] Kilby, J. S. (1964). "Miniaturized electronic circuits," US 3138743 A, issued June 23, 1964.

[10] Vadasz, L. L., et al. (1969). "Silicon-gate technology." IEEE Spectrum 6(10): 28-35.

[11] Seitz, F. and R. P. Johnson (1937). "Modern Theory of Solids. III." Journal of Applied Physics 8(4): 246-260.

[12] Slater, J. C. (1949). "Electrons in Perturbed Periodic Lattices." Physical Review 76(11): 1592-1601.

[13] Hall, R. N. and W. C. Dunlap (1950). "PN Junctions Prepared by Impurity Diffusion." Physical Review 80(3): 467-468

[14] Sze, S. and J. Irvin (1968). "Resistivity, mobility and impurity levels in GaAs, Ge, and Si at 300 K." Solid-State Electronics 11(6): 599-602.

[15] Atalla, M. M., et al. (1959). "Stabilization of silicon surfaces by thermally grown oxides." Bell Labs Technical Journal 38(3): 749-783.

[16] Atalla, M. and E. Tannenbaum (1960). "Impurity redistribution and junction formation in silicon by thermal oxidation." Bell Labs Technical Journal 39(4): 933-946.

[17] Wanlass, F. M. (1967). "Low stand-by power complementary field effect circuitry", US 3356858 A, issued Dec 5, 1967.

[18] Luisi, J. A., et al. (1976). "High speed-low cost, clock controlled CMOS logic implementation", US 3982138 A, issued Sep 21, 1976.

[19] Lifante, G. (2003). Integrated photonics: Fundamentals, J. Wiley.

[20] Lu, M., et al. (2008). "Label free biosensor incorporating a replica-molded, vertically emitting distributed feedback laser." Applied Physics Letters 92(26): 261502.

[21] Burrows, E. and K.-Y. Liou (1990). "High resolution laser LIDAR utilising two-section distributed feedback semiconductor laser as a coherent source." Electronics Letters 26(9): 577-579.

[22] Ibrahim, T. A., et al. (2003). "All-optical AND/NAND logic gates using semiconductor microresonators." IEEE Photonics Technology Letters 15(10): 1422-1424.

[23] O'Brien, J. L. (2007). "Optical quantum computing." Science 318(5856): 1567-1570.

[24] O'Brien, J. L., et al. (2009). "Photonic quantum technologies." Nature Photonics 3(12): 687-695.

[25] Alferov, Z. I., et al. (1975). "Liquid phase epitaxy of AlxGa1–xAs-GaAs heterostructures." Crystal Research and Technology 10(2): 103-110.

[26] Hakki, B. W. and T. L. Paoli (1975). "Gain spectra in GaAs double− heterostructure injection lasers." Journal of Applied Physics 46(3): 1299-1306.

[27] Holonyak Jr, N., et al. (1978). "Room-temperature continuous operation of photopumped MO-CVD $Al_x Ga_{1-x}$ As-GaAs-$Al_x Ga_{1-x}$ As quantum-well lasers." Applied Physics Letters 33(1): 73-75.

[28] Manasevit, H. and W. I. Simpson (1969). "The Use of Metal-Organics in the Preparation of Semiconductor Materials I. Epitaxial Gallium-V Compounds." Journal of The Electrochemical Society 116(12): 1725-1732.

[29] Dupuis, R. D. and P. D. Dapkus (1977). "Room-temperature operation of Ga (1− x) Al x As/GaAs double-heterostructure lasers grown by metalorganic chemical vapor deposition." Applied Physics Letters 31(7): 466-468.

[30] Dallesasse, J., et al. (1990). "Hydrolyzation oxidation of $Al_x Ga_{1-x}$ As-AlAs-GaAs quantum well heterostructures and superlattices." Applied Physics Letters 57(26): 2844-2846.

[31] Huffaker, D., et al. (1994). "Native-oxide defined ring contact for low threshold vertical-cavity lasers." Applied Physics Letters 65(1): 97-99.

[32] Coldren, L. A. (2000). "Monolithic tunable diode lasers." IEEE Journal of Selected Topics in Quantum Electronics 6(6): 988-999.

[33] Feng, M., et al. (2005). "Room temperature continuous wave operation of a heterojunction bipolar transistor laser." Applied Physics Letters 87(13): 131103.

[34] Craford, M. G., et al. (2001). "In pursuit of the ultimate lamp." Scientific American 284(2): 62-67.

[35] Thijs, P. J., et al. (1991). "High-performance 1.5 mu m wavelength InGaAs-InGaAsP strained quantum well lasers and amplifiers." IEEE Journal of Quantum Electronics 27(6): 1426-1439.

[36] Bai, Y., et al. (2008). "Room temperature continuous wave operation of quantum cascade lasers with 12.5% wall plug efficiency." Applied Physics Letters 93(2): 021103.

[37] Nakamura, S., et al. (1994). "Candela-class high-brightness InGaN/AlGaN double-heterostructure blue-light-emitting diodes." Applied Physics Letters 64(13): 1687-1689.

[38] Moutanabbir, O. and U. Gösele (2010). "Heterogeneous integration of compound semiconductors." Annual Review of Materials Research 40: 469-500.

[39] O'Mahony, M. J., et al. (2006). "Future optical networks." Journal of Lightwave Technology 24(12): 4684-4696.

[40] Kish, F. A., et al. (2011). "Current status of large-scale InP photonic integrated circuits." IEEE Journal of Selected Topics in Quantum Electronics 17(6): 1470-1489.

[41] Welch, D. F., et al. (2007). "Large-scale InP photonic integrated circuits: Enabling efficient scaling of optical transport networks." IEEE Journal of Selected Topics in Quantum Electronics 13(1): 22-31.

[42] Reed, G. T., et al. (2010). "Silicon optical modulators." Nature Photonics 4(8): 518-526.

[43] Liang, D. and J. Bowers (2009). "Photonic integration: Si or InP substrates?" Electronics Letters 45(12): 578-581.

[44] Kimerling, L., et al. (2006). Electronic-photonic integrated circuits on the CMOS platform. Integrated Optoelectronic Devices 2006, International Society for Optics and Photonics.

[45] Izhaky, N., et al. (2006). "Development of CMOS-compatible integrated silicon photonics devices." IEEE Journal of Selected Topics in Quantum Electronics 12(6): 1688-1698.

[46] Liow, T.-Y., et al. (2010). "Silicon modulators and germanium photodetectors on SOI: monolithic integration, compatibility, and performance optimization." IEEE Journal of Selected Topics in Quantum Electronics 16(1): 307-315.

[47] Jin, J.-M. (2011). Theory and computation of electromagnetic fields, John Wiley & Sons.

[48] Chuang, S. L. (2012). Physics of photonic devices, John Wiley & Sons.

[49] Coldren, L. A., et al. (2012). Diode lasers and photonic integrated circuits, John Wiley & Sons.

[50] Verdeyen, J. T. (1989). Laser electronics, Prentice Hall New Jersey.

[51] Jin, J. M. (2010). "The finite element method." Theory and Computation of Electromagnetic Fields: pp. 342-398.

[52] Heisenberg, W. (1961). On Modern Physics, Orion Press.

[53] Sakurai, J. J., et al. (1995). Modern quantum mechanics, Revised Edition, AAPT.

[54] Streetman, B. G. and S. Banerjee (2000). Solid state electronic devices, Prentice Hall New Jersey.

[55] Boyd, R. (2008). Nonlinear Optics (Third Edition). Burlington, Academic Press.

[56] Cheng, K.-Y. (1997). "Molecular beam epitaxy technology of III-V compound semiconductors for optoelectronic applications." Proceedings of the IEEE 85(11): 1694-1714.

[57] Hess, K. (2000). Advanced theory of semiconductor devices, IEEE press.

[58] Pai, N. P., et al. (2012). "Point-of-care testing for infectious diseases: diversity, complexity, and barriers in low-and middle-income countries." PLoS Med 9(9): e1001306.

[59] Gubala, V., et al. (2011). "Point of care diagnostics: status and future." Analytical chemistry 84(2): 487-515.

[60] Damhorst, G. L., et al. (2015). "Smartphone-imaged HIV-1 reverse-transcription loop-mediated isothermal amplification (RT-LAMP) on a chip from whole blood." Engineering 1(3): 324-335.

[61] Emadi, A., et al. (2012). "Linear variable optical filter-based ultraviolet microspectrometer." Applied optics 51(19): 43.

[62] Wan, Y., et al. (2016). "Compact characterization of liquid absorption and emission spectra using linear variable filters integrated with a CMOS imaging camera." Scientific Reports 6.

[63] Emadi, A., et al. (2012). "Linear variable optical filter-based ultraviolet microspectrometer." Applied Optics 51(19): 43.

[64] Huang, W.-K., et al. (2007). "A high-speed and high-responsivity photodiode in standard CMOS technology." IEEE Photonics Technology Letters 19(4): 197-199.

[65] Smith, A. M. and S. Nie (2012). "Compact quantum dots for single-molecule imaging." JoVE (Journal of Visualized Experiments)(68): e4236-e4236.

[66] Lim, S. J., et al. (2015). "Brightness-equalized quantum dots." Nature Communications 6.

[67] Al Hosani, E., et al. (2014). "A new optical-based device for online black powder detection in gas pipelines." IEEE Transactions on Instrumentation and Measurement 63(9): 2238-2252.

[68] Karr, J. R., et al. (1985). "Effects of chlorine and ammonia from wastewater treatment facilities on biotic integrity." Journal of Water Pollution Control Federation: 912-915.

[69] Long, K. D., et al. (2014). "Smartphone instrument for portable enzyme-linked immunosorbent assays." Biomedical optics express 5(11): 3792-3806.

[70] Hui, R., et al. (2003). "GaN-based waveguide devices for long-wavelength optical communications." Applied Physics Letters 82(9): 1326-1328.

[71] Coldren, L. A. (2000). "Monolithic tunable diode lasers." IEEE Journal of Selected Topics in Quantum Electronics 6(6): 988-999.

[72] Hui, R., et al. (2005). "III-nitride-based planar lightwave circuits for long wavelength optical communications." IEEE Journal of Quantum Electronics 41(1): 100-110.

[73] Titriku, A., et al. (2014). Efficiency modeling of tuning techniques for silicon carrier injection ring resonators. Optical Interconnects Conference, 2014 IEEE, IEEE.

[74] Zhang, X., et al. (2015). "Carrier-induced fast wavelength switching in tunable V-cavity laser with quantum well intermixed tuning section." Optics Express 23(20): 26336-26341.

[75] Hulme, J. C., et al. (2013). "Widely tunable Vernier ring laser on hybrid silicon." Optics Express 21(17): 19718-19722.

[76] Creazzo, T., et al. (2013). "Integrated tunable CMOS laser." Optics Express 21(23): 28048-28053.

[77] Wooten, E. L., et al. (2000). "A review of lithium niobate modulators for fiber-optic communications systems." IEEE Journal of Selected Topics in Quantum Electronics 6(1): 69-82.

[78] Geiss, R., et al. (2005). "Low loss GaN at 1550 nm." Applied Physics Letters 87(13): 132107.

[79] Morkoç, H. (2009). Handbook of nitride semiconductors and devices, Materials Properties, Physics and Growth, John Wiley & Sons.

[80] Amano, H., et al. (1986). "Metalorganic vapor phase epitaxial growth of a high quality GaN film using an AlN buffer layer." Applied Physics Letters 48(5): 353-355.

[81] Amano, H., et al. (1989). "P-type conduction in Mg-doped GaN treated with low-energy electron beam irradiation (LEEBI)." Japanese Journal of Applied Physics 28(12A): L2112.

[82] Nakamura, S., et al. (1992). "Thermal annealing effects on p-type Mg-doped GaN films." Japanese Journal of Applied Physics 31(2B): L139.

[83] Amano, H., et al. (1990). UV and blue electroluminescence from Al/GaN: Mg/GaN LED treated with low-energy electron beam irradiation (LEEBI). Institute of Physics: Conference Series.

[84] Sheu, J.-K., et al. (2003). "White-light emission from near UV InGaN-GaN LED chip precoated with blue/green/red phosphors." IEEE Photonics Technology Letters 15(1): 18-20.

[85] Davis, C. C. (1996). Lasers and electro-optics : fundamentals and engineering. Cambridge [England] ;, Cambridge University Press.

[86] Cuniot-Ponsard, M., et al. (2014). "Electro-optic and converse-piezoelectric properties of epitaxial GaN grown on silicon by metal-organic chemical vapor deposition." Applied Physics Letters 104(10): 101908.8.

[87] Pezzagna, S., et al. (2008). "Refractive indices and elasto-optic coefficients of GaN studied by optical waveguiding." Journal of Applied Physics 103(12): 123112.

[88] Ambacher, O., et al. (1999). "Two-dimensional electron gases induced by spontaneous and piezoelectric polarization charges in N-and Ga-face AlGaN/GaN heterostructures." Journal of Applied Physics 85(6): 3222-3233.

[89] Waltereit, P., et al. (2000). "Nitride semiconductors free of electrostatic fields for efficient white light-emitting diodes." Nature 406(6798): 865-868.

[90] Kogelnik, H. and C. Shank (1972). "Coupled-wave theory of distributed feedback lasers." Journal of Applied Physics 43(5): 2327-2335.

[91] Jayaraman, V., et al. (1993). "Theory, design, and performance of extended tuning range semiconductor lasers with sampled gratings." IEEE Journal of Quantum Electronics 29(6): 1824-1834.

[92] Wesström, J.-O., et al. (2004). State-of-the-art performance of widely tunable modulated grating Y-branch lasers. Optical Fiber Communication Conference, Optical Society of America.

[93] Choi, S. J., et al. (2005). "Tunable narrow linewidth all-buried heterostructure ring resonator filters using vernier effects." IEEE Photonics Technology Letters 17(1): 106-108.

[94] Wesstrom, J.-O., et al. (2002). Design of a widely tunable modulated grating Y-branch laser using the additive Vernier effect for improved super-mode selection. Semiconductor Laser Conference, 2002. IEEE 18th International, IEEE.

[95] Jung, H., et al. (2014). "Electrical tuning and switching of an optical frequency comb generated in aluminum nitride microring resonators." Optics letters 39(1): 84-87.

[96] Bu, G., et al. (2004). "Guided-wave acousto-optic diffraction in Al x Ga 1− x N epitaxial layers." Applied Physics Letters 85(12): 2157-2159.

[97] O'Clock Jr, G. and M. Duffy (1973). "Acoustic surface wave properties of epitaxially grown aluminum nitride and gallium nitride on sapphire." Applied Physics Letters 23(2): 55-56.

[98] Auld, B. A. (1973). Acoustic fields and waves in solids, Рипол Классик.

[99] Kim, Y. and W. D. Hunt (1990). "Acoustic fields and velocities for surface-acoustic-wave propagation in multilayered structures: An extension of the Laguerre polynomial approach." Journal of Applied Physics 68(10): 4993-4997.

[100] Bykhovski, A., et al. (1997). "Elastic strain relaxation and piezoeffect in GaN-AlN, GaN-AlGaN and GaN-InGaN superlattices." Journal of Applied Physics 81(9): 6332-6338.

[101] Boonchun, A. and W. R. Lambrecht (2010). "First-principles study of the elasticity, piezoelectricity, and vibrational modes in LiGaO 2 compared with ZnO and GaN." Physical Review B 81(23): 235214.

[102] Polian, A., et al. (1996). "Elastic constants of gallium nitride." Journal of Applied Physics 79(6): 3343-3344.

[103] Manchon, D., et al. (1970). "Optical studies of the phonons and electrons in gallium nitride." Solid State Communications 8(15): 1227-1231.

[104] Pasquariello, D. and K. Hjort (2002). "Plasma-Assisted InP-to-Si Low Temperature Wafer Bonding". IEEE Journal of Selected Topics in Quantum Electronics 8.1.

[105] Mountanabbir, O., et al. (2008). "III-V and III-Nitride Engineered Heterostructures: Wafer Bonding, Ion Slicing, And More". ECS Transactions.

[106] Liang, D., et al. (2010). "Hybrid Integrated Platforms for Silicon Photonics". Materials: 1782-1802.

[107] Kazior, T.E. (2014). "Beyond CMOS: Heterogeneous Integration of III-V Devices, RF MEMS, and Other Dissimilar Materials/Devices with Si CMOS to Create Intelligent Microsystems". Philosophical Transactions of the Royal Society A: Mathematical, Physical and Engineering Sciences 372.2012

[108] Hermanowski, J. (2009). Thin wafer handling - Study of temporary wafer bonding materials and processes. 2009 IEEE International Conference on 3D System Integration.

[109] Science Lab. (2013, May 21). Potassium Hydroxide [Material Safety Data Sheet]. Retrieved from http://www.sciencelab.com/msds.php?msdsId=9922949.